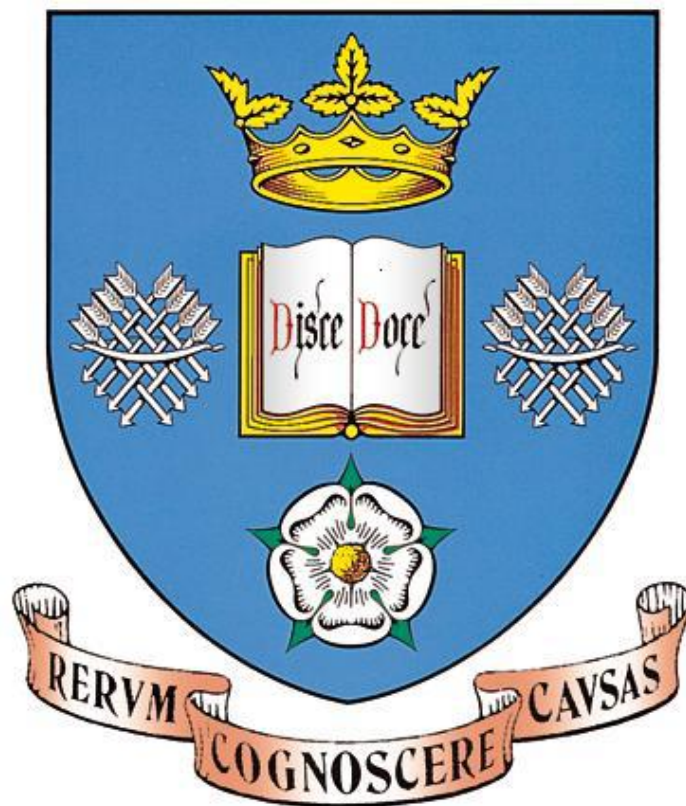


Hybrid Quantum Well/Quantum Dot Structure for Broad Spectral Bandwidth Emitters

By

Siming Chen



**Department of Electronic and Electrical
Engineering**

*Thesis submitted to the University of Sheffield for the
degree of Doctor of Philosophy*

April 2014

Intentionally Blank

Abstract

This thesis details a hybrid quantum well (QW)/quantum dot (QD) active element for an application in broadband source.

First of all, a literature review on the fundamentals of optical coherence tomography (OCT) and superluminescent light emitting diodes is provided in Chapter 1. Basic principles of QD formation using molecular beam epitaxy and several experimental techniques are reviewed in Chapter 2.

The first vertically integrated hybrid QW/QD structure for application in broadband light sources is proposed in Chapter 3. Spontaneous emission from both the QW and the QDs resulted in a full width half maximum (FWHM) of 250nm being demonstrated.

In Chapter 4, experimental results on the modal gain and lasing characteristic of hybrid QW/QD laser are described. Due to the contribution from the QD ground state and first excited state, and the lowest energy transition of the QW, the modal gain at room temperature is extended to 300nm. The values for modal gain are further confirmed by simultaneous three state lasing.

The first hybrid QW/QD superluminescent diode is discussed in Chapter 5. High order QW transitions are observed at high current densities. As a result, a 3dB emission spectrum of FWHM linewidth of 289nm centered at ~1200nm with a corresponding power of 2.4mW is achieved.

The origin of high order QW transitions is discussed in Chapter 6. New device designs utilizing a larger number of QD layers with higher areal density and larger state separation is reported in Chapter 7. Chapter 8 summarizes the whole thesis.



Dedicated to my parents and family

Acknowledgements

I would like to extend my deepest thanks to my lovely supervisor, Prof. Richard Hogg for tolerating my ignorance and helping me grow up. Without his guidance, insight and support, it would not have been as comprehensive or complete.

I would like to thank those senior members in my group for their support, advice and friendship. Especial thanks go to ZZ and Qi for their help and guidance during my research and life in Sheffield. Thanks also to Big Dave and Kris for technical support and advice on device testing. I would also like to thank Ken and Nasser for their support and advice on device fabrication (Ken is very accommodating and I am actually a big fan of him).

I would also like to thank my colleagues especially Xiao, Jon, Little Dave, Negin, Majid, Hifsa, Richard, Kristof, Omar, Saurabh, Hongchi, Luke, Avan, Amilia, Noura. And most importantly, a massive love to Kejia and Wei (we are always family!!!).

I also gratefully acknowledge the growers at the National Centre for III-V Technologies, especially Shiyong, Max, Ed. Thanks also goes to colleagues in QD Laser Inc, particularly, Sugawara-san, Kageyama-san, Nishi-san, and Takemasa-san.

My final thanks are to my parents and family for their endless love. They are always proud of me, and I won't let them down.

List of Publications

Journal Paper (Refereed)

- [1] M. A. Majid, D. T. D. Childs, H. Shahid, **S. Chen**, K. Kennedy, R. J. Airey, R. A. Hogg, E. Clarke, P. Howe, P. D. Spencer, and R. Murray., "Towards 1550-nm GaAs-based lasers using InAs/GaAs quantum dot bilayers," *IEEE J. Sel. Topics Quantum Electron.*, vol. **17**, no.5, pp.1134-1142. 2011.
- [2] M. A. Majid, D.T.D Childs, H. Shahid, **S. Chen**, K. Kennedy, R. J. Airey, R. A. Hogg, E. Clarke, P. Spencer and R. Murray., "Excited State Bilayer Quantum Dot Lasers at 1.3 μm ," *Jpn. J. of Appl. Phys.*, vol. **50**, p. 04DG10. 2011.
- [3] **S. M. Chen**, K. J. Zhou, Z. Y. Zhang, D. T. D. Childs, M. Hugues, A. Ramsay, and R. Hogg., "Ultra-broad spontaneous emission and modal gain spectrum from a hybrid quantum well/quantum dot laser structure," *Appl. Phys. Lett.*, vol. **100**, no. 4, pp. 041118-041118-3, 2012.
- [4] **S. Chen**, K. Zhou, Z. Zhang, O. Wada, D. T. D Childs, M. Hugues, and R. A. Hogg., "Room temperature simultaneous three-state lasing in hybrid quantum well/quantum dot laser," *Electron. Lett.*, vol. **48**, no. 11, pp. 644-645, 2012.
- [5] K. Zhou, Q. Jiang, Z. Zhang, **S. Chen**, H. Liu, Z. Lu, K. Kennedy, S. Matcher, and R. A. Hogg., "Quantum dot selective intermixing for broadband light sources," *Opt. Express.*, vol. **20**, no. 24, pp. 26950-26957, 2012.
- [6] **Siming Chen**, Kejia Zhou, Ziyang Zhang, J. R. Orchard, D. T. D. Childs, M. Hugues, O. Wada, and R. A. Hogg, "Hybrid Quantum Well/Quantum Dot Structure for Broad Spectral Bandwidth Emitters," *IEEE J. Sel. Topics Quantum Electron.*, vol.**19**, no. 4, pp.1900209-1900209-9, Jul/Aug. 2013.

Conference and Proceeding Paper (Refereed)

- [1] M. A. Majid, D.T.D. Childs, **S. Chen**, H. Shahid, K. M. Groom, K. Kennedy, R. A. Hogg, E. Clarke, P. Spencer, and R. Murray., "**Gain Spectra Analysis of Bilayer Quantum Dot Lasers beyond 1.3 μm** ," *Photonics Global Conference (PGC), Proc. IEEE.*, 5706039, 1 (2010).
- [2] M. A. Majid, **S. Chen**, D. T. D. Childs, H. Shahid, R. J. Airey, K. Kennedy, R. A. Hogg, E. Clarke, P. Spencer and R. Murray., "**Gain and absorption**

characteristics of bilayer quantum dot lasers beyond 1.3 μm ,” *Novel In-Plane Semiconductor Lasers X, Proc. SPIE*. **7953**, 795303 (2011).

- [3] **S. Chen**, K. Zhou, Z. Zhang, D. T. D. Childs, J. R. Orchard, R. A. Hogg, K. Kennedy, and M. Hugues., “Hybrid quantum well/ quantum dot structure for broad spectral bandwidth devices,” *Physics and Simulation of Optoelectronic Devices XX, Proc. of SPIE.*, **8255**, 82550E (2012).
- [4] K. Zhou, **S. Chen**, D. T. D. Childs, and R. A. Hogg., “Effect of modulation p-doping on the differential carrier lifetime of quantum dot lasers,” *Novel In-Plane Semiconductor Lasers XI, Proc. SPIE.*, vol. **8277**, 827720-1 (2012).
- [5] **S. Chen**, K. Zhou, Z. Zhang, O. Wada, D. T. D. Childs, K. Kennedy, M. Hugues, and R. A. Hogg., “Hybrid quantum well/quantum dot active element for broad spectral bandwidth emitters and amplifiers,” *23rd International semiconductor laser conference (ISLC), Proc. IEEE*, 120-121, 7-10 Oct. 2012.
- [6] **Siming Chen**, N. Peyvast, K. Zhou, N. Babazadeh, Z. Zhang, D. T. D. Childs, M. Hugues, O. Wada, and R. A. Hogg, T. Kageyama, K. Nishi, T. Takemasa, and M. Sugawara, “Broad bandwidth emission from hybrid QW/QD structures,” *Lasers and Electro-Optics Pacific Rim (CLEO-PR) conf.*, Tokyo, 2013.

Conference Talk and Poster

K. Zhou, D. T. D. Childs, **S. Chen** and R. A. Hogg,

UK Semiconductor, Sheffield, UK (July. 2011)-Oral

“Measurement of Differential Carrier Lifetime of Un-doped and Modulation p-doped Quantum Dot Lasers”

S. Chen, K. Zhou, Z. Zhang, D. T. D. Childs, J. Orchard, R. A. Hogg, K. Kennedy, and M. Hugues

SPIE Photonics West, San Francisco, California, USA (Jan. 2012)-Oral

“Hybrid Quantum Well / Quantum Dot Structures for Broad Spectral Bandwidth Devices”

K. Zhou, **S. Chen**, D.T.D. Childs, R.A. Hogg,

UK Semiconductor, Sheffield, UK, (July. 2012)-Poster

"Effect of Modulation p-Doping on the Differential Carrier Lifetime of Quantum Dot Lasers"

K. J. Zhou, Q. Jiang, Z. Y. Zhang, **S. M. Chen**, H. Y. Liu, K. Kennedy and R. A. Hogg,

The Celebration of the 50th Anniversary of the Diode Laser-IOP, Coventry, UK (Sep. 2012)-Poster

"Broadband Quantum Dot Light Source Based on Selective Area Intermixing

Process"

K. J. Zhou, O. Wada, **S. M. Chen**, Z. Y. Zhang, D. T. D Childs, K. Kennedy and Richard A. Hogg,

23rd International semiconductor laser conference (ISLC), San Diego, California, USA (Oct. 2012)-Poster

"Characterization of Recombination Processes in Quantum Dot Lasers Using Small Signal Modulation"

S. Chen, K. Zhou, Z. Zhang, D. T. D. Childs, O. Wada, M. Hugues, and R. A. Hogg
UK Semiconductor, Sheffield, UK (Jul. 2012)-Oral

"Hybrid Quantum Well/Quantum Well Active Element for Broad Spectral Bandwidth Source"

S. Chen, K. Zhou, Z. Zhang, D. T. D. Childs, M. Hugues, and R. A. Hogg
The Celebration of the 50th Anniversary of the Diode Laser-IOP, Coventry, UK (Sep. 2012)-Poster

"Hybrid Quantum Well / Quantum Dot Laser Structure for Broad Spectral Bandwidth Emitters and Amplifiers"

S. Chen, K. Zhou, D. T. D. Childs, Z. Zhang, M. Hugues, and R. A. Hogg
23rd International semiconductor laser conference (ISLC), San Diego, California, USA (Oct. 2012)-Poster

"Hybrid Quantum Well / Quantum Dot Active Element for Broad Spectral Bandwidth Emitters and Amplifiers"

S. Chen, N. Peyvast, K. Zhou, N. Babazadeh, Z. Zhang, D. T. D. Childs, M. Hugues, and R. A. Hogg

UK Semiconductor, Sheffield, UK (Jul. 2013)-Oral

"Broad Bandwidth Emission from Hybrid Quantum Well/Quantum Well Structure"

S. Chen, N. Peyvast, K. Zhou, N. Babazadeh, Z. Zhang, D. T. D. Childs, M. Hugues, O. Wada, and R. A. Hogg, T. Kageyama, K. Nishi, K. Takemasa, and M. Sugawara,
The 18th Opto-Electronics and Communications Conference / Photonics in Switching 2013 (CLEO-PR&OECC/PS 2013)-Oral

"Broad Bandwidth Emission from Hybrid QW/QD Structures"

Contents

| | |
|--|-----|
| Abstract | II |
| Acknowledgements | IV |
| List of Publications | V |
| Chapter 1: Introduction | 1 |
| 1.1 Optical Coherence Tomography | 1 |
| 1.2 Superluminescent Diodes (SLD) | 4 |
| 1.2.1 Overview of Superluminescent Diodes | 4 |
| 1.2.2 Principles of SLD Operation | 5 |
| 1.2.3 Main Characteristics | 6 |
| 1.2.4 SLDs Fabrication | 10 |
| 1.2.5 Self- Assembled QDs for SLDs | 11 |
| 1.3 Broadband QD-SLD – “State-of-the-Art” | 14 |
| 1.4 Outline of This Thesis | 17 |
| Reference | 22 |
| Chapter 2: Experimental Techniques | 25 |
| 2.1 Introduction | 25 |
| 2.2 Molecular Beam Epitaxy (MBE) | 25 |
| 2.3 A Method of Quantum Dots Formation: Stranski-Krastanow (S-K) Growth Mode | 29 |
| 2.4 Experimental Techniques | 32 |
| 2.4.1 Photoluminescence Spectroscopy | 32 |
| 2.4.2 Electroluminescence | 37 |
| 2.4.3 Photocurrent Spectroscopy (PC) | 39 |
| Reference | 42 |
| Chapter 3: Ultra-Broad Spontaneous Emission from a Hybrid QW/QD Structure | 46 |
| 3.1 Introduction | 46 |
| 3.2 Background | 47 |
| 3.3 Experiments | 50 |
| 3.4 Results and Discussion | 56 |
| 3.5 Conclusion | 70 |
| 3.6 Future work | 71 |
| Reference | 73 |
| Chapter 4: Gain and Lasing Characteristics of Hybrid QW/QD Laser | 76 |
| 4.1 Introduction | 76 |
| 4.2 Background | 77 |
| 4.3 Experiments | 78 |
| 4.4 Results and Discussion | 81 |
| 4.5 Conclusion | 97 |
| 4.6 Future Work | 98 |
| Reference | 99 |
| Chapter 5: Realization of Ultra-Broad Bandwidth Superluminescent Diodes Using Hybrid QW/QD Structure | 101 |
| 5.1 Introduction | 101 |

| | |
|---|-----|
| 5.2 Experiments | 102 |
| 5.3 Results and discussion | 103 |
| 5.4 Conclusion | 115 |
| 5.5 Future work | 116 |
| Reference | 117 |
| Chapter 6: Study of QD-Induced Strain Modulation of a QW..... | 120 |
| 6.1 Introduction..... | 120 |
| 6.2 Experiments | 121 |
| 6.3 Results and Discussion..... | 124 |
| 6.4 Summary | 130 |
| 6.5 Future Work | 130 |
| Reference | 131 |
| Chapter 7: Development of New Design of Hybrid QW/QD Structure for High Power and Broad Bandwidth Superluminescent Diodes..... | 133 |
| 7.1 Introduction..... | 133 |
| 7.2 Second Generation Hybrid QW/QD Structure..... | 135 |
| 7.2.1 Device Structure and Fabrication..... | 135 |
| 7.2.2 Results and Discussion..... | 139 |
| 7.3 Third Generation Hybrid QW/QD Structure..... | 143 |
| 7.3.1 Device Structure and Fabrication..... | 143 |
| 7.3.2 Results and Discussion..... | 147 |
| 7.4 Conclusion | 153 |
| 7.5 Future Work | 153 |
| Reference | 155 |
| Chapter 8: Conclusion..... | 157 |

Chapter 1: Introduction

1.1 Optical Coherence Tomography

There has been growing interest in broad spectral bandwidth sources for use in biological tissue imaging applications, such as optical coherence tomography (OCT) [1]. OCT is a non-invasive, non-contact imaging technique that can perform high resolution cross-sectional imaging of internal structure in biological tissue [2]. It operates as a type of “optical biopsy”, which enables *in-situ* imaging of tissue in real time [3].

The wavelengths for tissue imaging operate in the biological “window” of 1000-1300 nm, offering the possibility to perform OCT imaging with high quality and deep penetration in tissue. For instance, typically ~1050nm [3, 4] is used for ophthalmology and 1200-1300nm [5] is used for imaging skin tissue due to the minimum of optical dispersion in water, and the minimum in scattering and absorption, respectively [6].

The principle of OCT is based on low coherence interferometry [7], i.e. a Michelson interferometer, which measures the intensity of light and its time delay by interfering it with light that has traveled with certain reference path length and hence time delay.

There are two main types of OCT systems: time domain (TD)-OCT and Fourier domain (FD)-OCT / sweep laser source (SLS)-OCT. In both types of OCT system, the final imaging is made up from individual axial scans (taken by one scan of reference arm or one sweep of the laser) taken during a lateral scan of the optical beam by scanning optics. The axial and lateral resolutions of OCT are not related to each other; the lateral resolution of the OCT is controlled by the scanning optics and is limited by the diffraction limit, which is a function of wavelength. While the axial resolution is directly related to the coherence length of the light emitting source, and is defined by the following equation:

$$L_c = \frac{2\ln 2}{\pi} \times \frac{\lambda_0^2}{\Delta\lambda} \approx 0.44 \times \frac{\lambda_0^2}{\Delta\lambda} \quad (1.1)$$

where λ_0 is the centre wavelength and $\Delta\lambda$ is the full-width at half maximum (FWHM) of a light emitting source with Gaussian emission spectrum. A general definition of axial resolution is the FWHM of the coherence length, and a detailed description of how this equation is derived can be found in [8]. Therefore, higher axial resolution can be achieved by using a broadband light-emitting source, such as superluminescent diodes (SLDs).

A typical TD-OCT system is schematically shown in Fig. 1.1 [9]. Low coherence light is emitted from a broadband light emitting source, the light is split into two arms by the beam splitter, one directed at the sample arm (containing the specimen of interest), the other to a reference arm (usually a mirror). The interference of light reflected back

from these two arms is then detected by a photodiode, but interference only occurs when the path lengths from both arms match to within the coherence length of the light. By scanning the reference arm, an axial reflectivity profile of the sample can be obtained, and this reflectivity profile is called an A-scan, which contains information about the spatial dimensions and location of structures within the sample. It is noteworthy that, for the A-scan, the emitted and reflected light is collinear. By scanning the optical beam in the transverse direction across the sample, a cross-section (B-scan) is achieved. And also by combining multiple cross-sections, a 3D image can be generated.

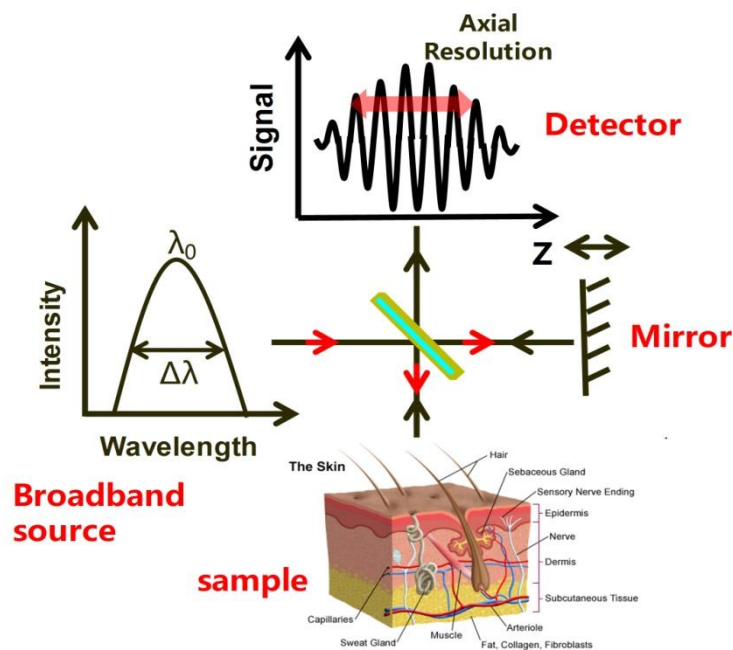


Fig. 1.1. Schematics of a TD-OCT system [9].

Fig. 1.2 schematically shows a typical SLS FD-OCT system, as can be seen, SLS FD-OCT systems vary from DT-OCT systems in that, instead of using a broadband source (SLDs) as the light source, and the interference is achieved by encoding the

optical frequency in time with a fast sweeping laser through a range of frequencies. The axial scan can be calculated immediately through a Fourier transform from the acquired spectra, without movement of the mirror [10], which improves the signal to noise and hence the speed of imaging significantly.

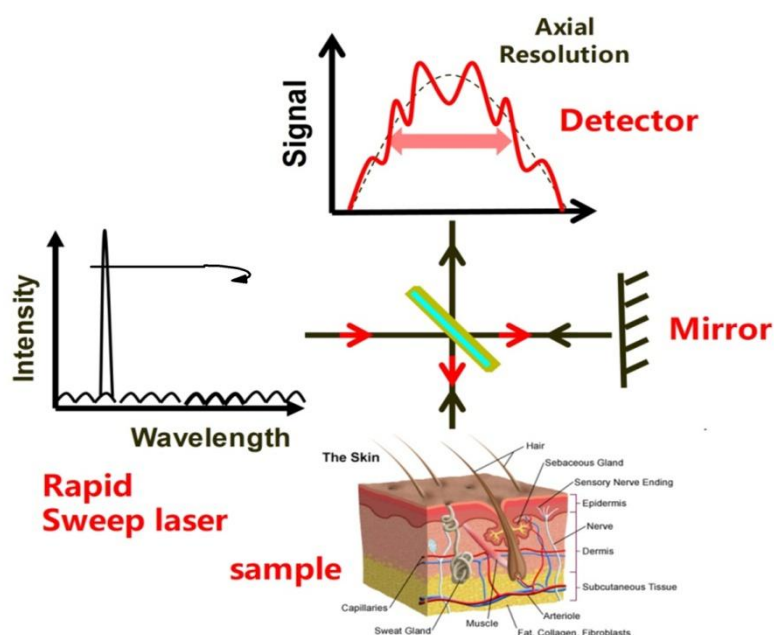


Fig. 1.2. Schematics of a SLS FD-OCT system [9, 10].

1.2 Superluminescent Diodes (SLD)

1.2.1 Overview of Superluminescent Diodes

An superluminescent light emitting diode (SLD) is an edge emitting semiconductor light source based on the internal amplification of spontaneous emission, which was invented by Dr. Gerard A. Alphonse at RCA Laboratories in 1986. This light source was developed as a key component in the next generation of fiber-optic gyroscopes [11], low coherence interferometry for tissue imaging, such as optical coherence

tomography, and wavelength-division multiplexing (WDM) system testing [12].

The unique property of the superluminescent diode is the combination of the high power and brightness of laser diodes (LDs), i.e. optical gain, with the low coherence of light-emitting diodes (LEDs), i.e. broad spectral emission. The key difference between LDs and SLDs is that there is insufficient optical feedback to support lasing. A summary of differences in operation, characteristics, and structures between LDs, SLDs and LEDs is displayed in table 1[13].

| Property | LD | SLD | LED |
|------------------------|---------------------|--|--|
| Light emission process | Stimulated emission | Amplified spontaneous emission | Spontaneous emission |
| Optical Bandwidth | Small | Large | Larger |
| Optical Power | High | Medium | Low |
| Coherence | Large | Small | Small |
| Device structure | Optical waveguide | Optical waveguide (inhibit optical feedback) | Waveguide structure or normal emission |

Table. 1.1 Summary of properties in operation, characteristics, and structures of LDs, SLDs, and LEDs [13].

1.2.2 Principles of SLD Operation

Similar to a LD, the structure of a SLD is based on an electrically driven p-n junction, with its active region sandwiched in between waveguide layers. A typical SLD structure is shown in Fig. 1.3. When the device is operated under forward bias, the hole current flows from the p-type layer through to the n-type layer underneath, and the electron current will flow in the opposite direction. The luminescence is generated in the active region through the spontaneous recombination of electrons and holes and

is then amplified when traveling along the waveguide of the SLD operating in positive net-modal gain, as indicated in inset of Fig. 1.3.

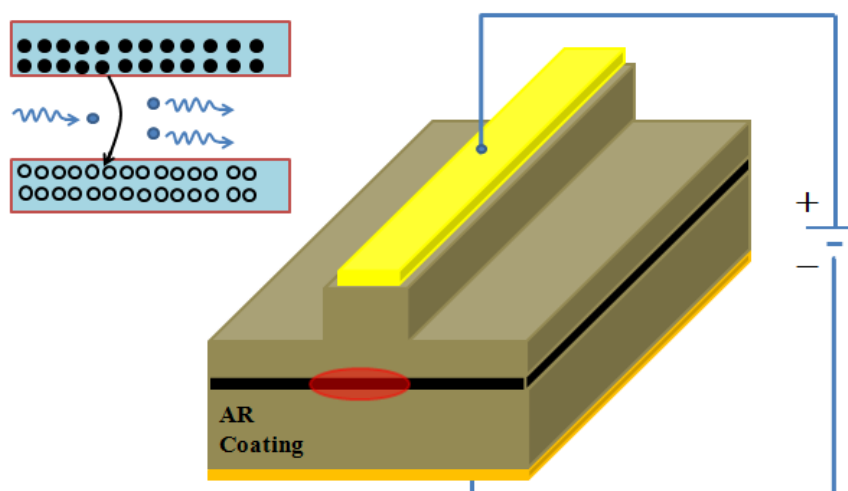


Fig. 1.3. Schematic diagram of a typical SLD with AR coating.

The SLD is designed to have high single pass amplification for spontaneous emission generated along the waveguide to achieve high output power, but with insufficient optical feedback to achieve lasing, which can be successfully obtained by using a tilted waveguide and/or anti-reflection coated facets or introducing an absorber section.

1.2.3 Main Characteristics

1.2.3.1 Dependence of power on current

High output power is a key feature for SLDs, which depends exponentially on optical gain and is linear with the spontaneous emission rate [14]. As a result, a high modal gain is highly desirable to achieve high output power.

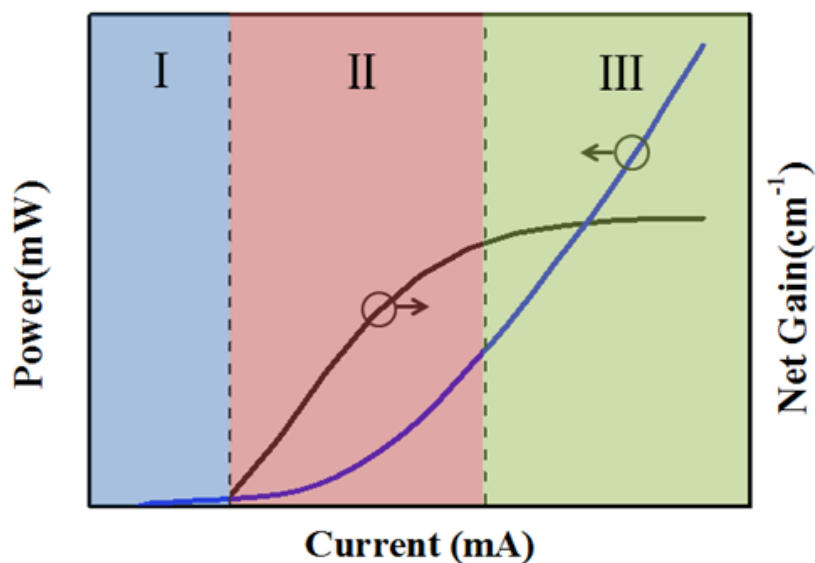


Fig. 1.4. Schematic of L-I curve and net modal gain curve against current [14].

Fig 1.4 schematically shows an example of typical net gain, and power-current characteristic of an SLD. As indicated, in region one, there is no gain, and only spontaneous emission exists, the output power linearly increases with current at very low efficiency. Increasing the current, there is a soft knee observed in the L-I curve in region two, corresponding to the transition between the spontaneous emission dominated region and the amplified spontaneous emission dominated region. In this region, the net gain is linearly increasing with input current and the power increases exponentially with injection current. At high currents, the net gain saturates, a superlinear L-I curve is obtained due to the amplification of spontaneous emission. The output power in this region becomes linear with input current again while with high efficiency, though not as high as a LD. [15].

1.2.3.2 SLD spectral properties and coherence length

In addition to high power, large bandwidth is another key feature for the SLD. There are several parameters used to describe the spectral properties of SLDs, but the main parameters are spectrum bandwidth, centre wavelength and peak wavelength. The spectrum bandwidth is expressed in terms of the full width at half maximum (FWHM) of the power spectral density of SLDs. The bandwidth of the spectrum is essentially determined by the optical gain spectrum of the material. The centre wavelength (λ_{centre}) is defined as central wavelength between the two FWHM points of the power spectral density. And the peak wavelength (λ_{peak}) is defined as a wavelength where the maximum intensity can be achieved, which may be different from the λ_{centre} due to the asymmetry of the power spectral density.

The coherence length (L_c) is an important quantity utilized to characterize the coherence of the light emitting source. It is usually defined as the propagation distance over which a coherent light wave maintains a required degree of coherence. The SLD coherence length is governed by the FWHM of the SLD spectrum through the equation:

$$L_c = K \frac{\lambda^2}{\Delta\lambda} \quad (1.2)$$

where λ is centre wavelength, $\Delta\lambda$ is the FWHM of the SLD spectrum, and the K is a coefficient related to the spectrum properties. Therefore, the value of coherence length is inversely proportional to the spectrum bandwidth. SLDs are optical sources with a

large spectral bandwidth, which corresponds to a small coherence length. Based on low-coherence interferometry, SLDs can be used to achieve high spatial resolution in imaging systems.

1.2.3.3 Optical feedback to the SLD

High gain in the SLDs active region is crucial to achieve high output power, however this results in high sensitivity of the SLD to optical feedback. Optical feedback, due to the residual reflections from facets and coupling fibers, leads to high residual spectral modulation, which is observed as parasitic Fabry-Perot modulation. The spectral ripple is a measure of the fluctuation of the power spectral density of the SLD over a small range of wavelength, which can be observed by using a high-resolution optical spectrum analyzer. The effect of spectral ripple is more pronounced in high power SLDs and occurs mainly around the peak wavelength where the optical gain is highest. The spectral ripple always exists to some extent, and it is undesirable since the presence of an excessive spectral ripple in the power spectral density of the SLD results in secondary subpeaks in the self-coherence function [8], which will limit the longitudinal resolution.

1.2.3.4 Temperature performance of SLDs

It is known that SLDs are designed in such a manner to have very high lasing threshold currents (two to three times) than those in semiconductor lasers [14]. This increase in threshold current is mainly due to the insufficient optical feedback. SLDs working at such a high level of current leads to thermal issues, which in turn,

may result in a strong reduction of the optical power with temperature, since the output power of SLDs is exponential to optical gain. In semiconductor devices, the optical gain depends strongly on temperature; therefore, cooling arrangement and power supplies are always required for the operation of SLDs.

1.2.4 SLDs Fabrication

Different waveguide structures are employed for SLDs for different purposes. A number of device designs are schematically shown in the Fig. 1.5, including tilted single contact device (a), standard single contact device with antireflection (AR) coating (b), tapered waveguide device (c), curved waveguide structure (d), etched angled facet structure (e), multisection device (f), and so on.

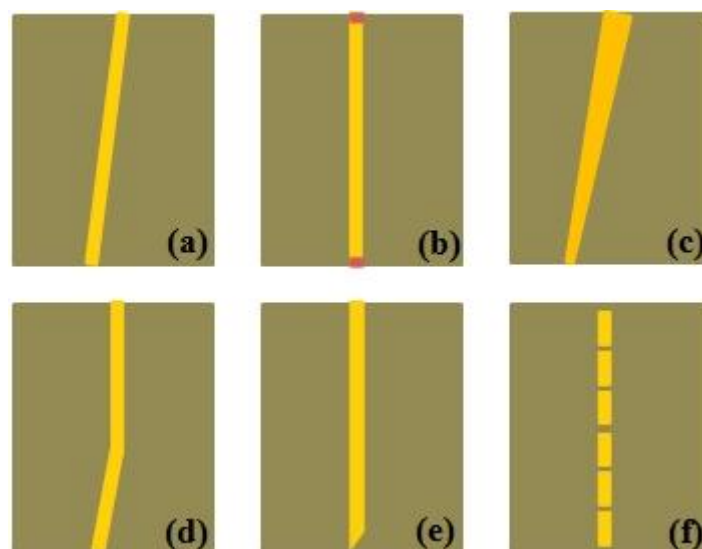


Fig. 1.5 Schematic plan view of various SLD structures [13].

The most commonly used structure for SLDs is a single contact waveguide stripe with a tilted angle ($\sim 7^\circ$ in GaAs based structure) with respect to the facet [16, 17]. By

doing so, the light reflected from the facets will be poorly coupled back into the cavity, leading to a reduced optical feedback that inhibits lasing action. AR coating applied to the facets is another useful method to reduce optical feedback, and is often used in conjunction with a tilted waveguide structure. A tapered waveguide structure is usually employed for SLDs for achieving high output power from the facet, but at the expense of poor coupling efficiency into the optical fiber [18]. Etched angled facets have also been utilized. By using etched angled facet on a waveguide normal to the cleaved facet, the reflection of light back into the waveguide from the etched angled facet can be significantly reduced to less than 1×10^{-5} [19, 20].

Most recently, there is a large research effort to develop multisection SLDs, especially for QD based SLDs. Multisection structures have several advantages over single contact structures through allowing more flexibility in tailoring the emission spectrum [21], controlling the degree of relative optical feedback [22], allowing the optical gain, and loss as well the spontaneous emission to be determined with ease [23, 24]. However, the fabrication of multi-section devices is more complicated than single contact devices. Also the drive for multi-section devices is more complex since commercial devices based on multi-section devices are required to have extensive and expensive characterization tests prior to sale.

1.2.5 Self- Assembled QDs for SLDs

Size-quantization introduced by large confinement energy has significant effects on

the density of states (DOS) of the active region. In addition to the quantum well (QW) case, where the carriers are confined in one dimension, we can also imagine the situations, where the carriers are confined in two directions, i.e. quantum wire and even in all three directions, i.e. quantum dot (QD). All these different cases are illustrated in Fig. 1.6 [25, 26].

It is seen that, an ideal zero-dimensional QD system results in discrete energy states with fixed photon energies. The DOS represents a series of delta-function peaks centered at the atomic-like energy levels. The number of carriers at the operating energy is significantly enhanced, which leads to much steeper dependence of the gain on the injection current density, while the transparency current is reduced [25]. Also, in comparison to a conventional bulk semiconductor laser, where the temperature dependence of threshold current is mainly ascribed to the thermal spreading of the injected carriers over a wider energy range of states, which then results in reduced gain at a given injection. In the QD system, due to the delta-function like density of states, such thermal spreading is expected to be reduced significantly. Thus, from the point of view of laser applications, as compared to bulk and QW competitors, a QD laser would provide much lower threshold current density, high gain, reduced temperature sensitivity and much narrower emission line width.

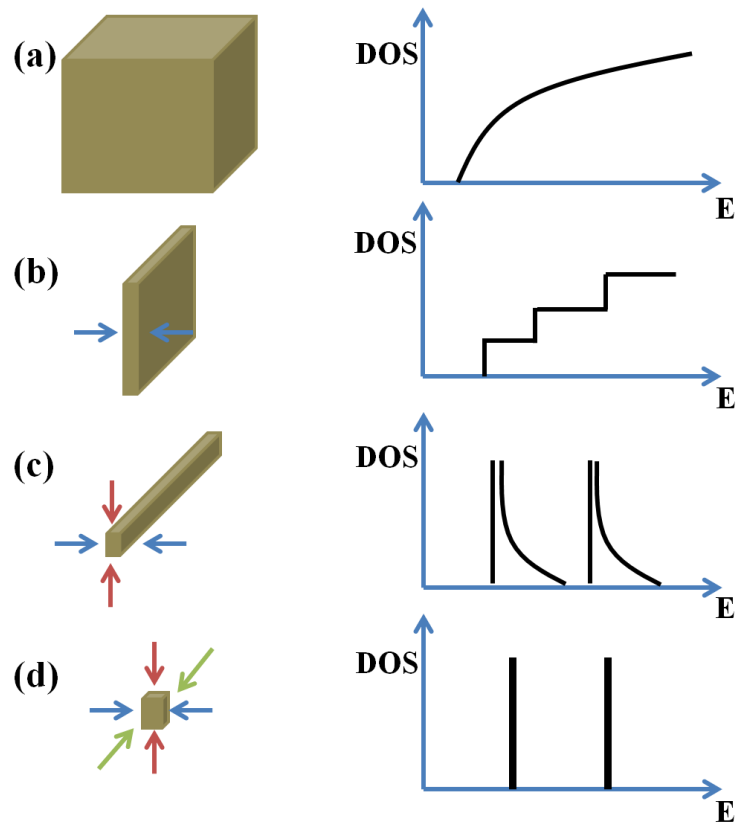


Fig. 1.6. Active region and its corresponding DOS of (a) bulk semiconductor, (b) quantum wells, (c) quantum wires, and (d) quantum dots [25, 26].

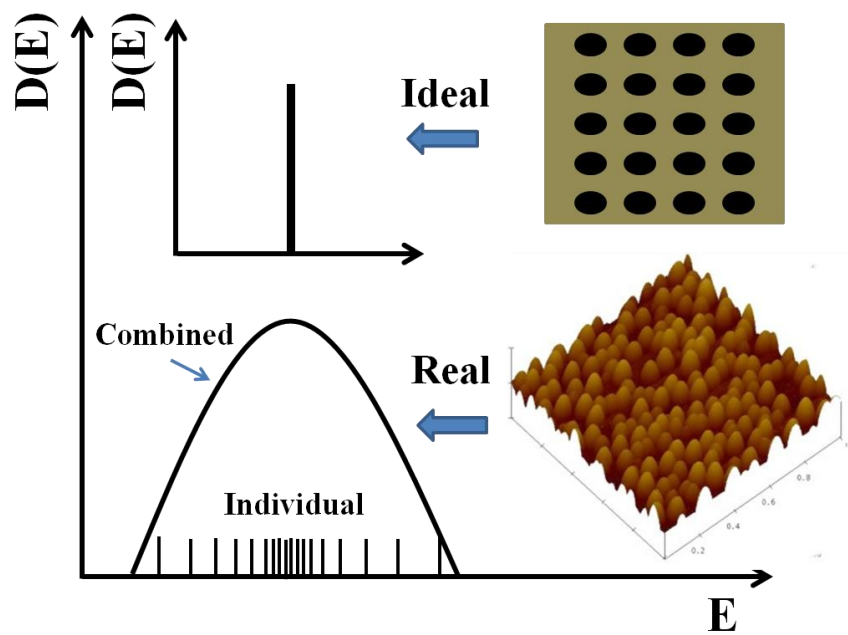


Fig. 1.7. Schematic of size distribution and emission spectra of ideal and real QD ensembles [13].

However, in reality, during the growth of SAQDs by using the Stranski-Krastanow (S-K) mode (the phenomenon of island formation during epitaxial growth of highly lattice-mismatched materials), the homogeneity of size and composition is not well controlled. The typical size uniformity is no better than 10% [27], which results in a naturally inhomogeneous broadening of the emission spectrum, as illustrated in the Fig. 1.7. For laser application, this inhomogeneity reduces the peak optical gain since only a small number of QDs can contribute to lasing and hence the optical power. However, this inhomogeneous broadening becomes an advantage for broadening the emission bandwidth in SLDs, where all the QDs can contribute to the emission. Another challenge for QD lasers is the relatively small gain due to the limited number of states, which results in the ground state being saturated at low current density. However, this is again highly beneficial for SLDs, as the introduction of excited states can further broaden the emission bandwidth [16, 21].

1.3 Broadband QD-SLD – “State-of-the-Art”

It has been predicted that the natural size and composition inhomogeneity as well as the state filling of the self-assembled quantum dots grown by SK mode is very beneficial for broadening the emission bandwidth. Quantum dots SLDs with tens of nanometers have been reported [16, 18, 28].

To further broaden the emission bandwidth of QD-based SLDs, various methods have

been pursued including: chirped QDs, QDs intermixing, and QD multi-section device and so on.

The idea of chirped multiple QD layers utilize a multi-layer stack of QDs in which the different QD layers are engineered to have different emission wavelengths. The effect of “chirping” can be achieved by introduction of multiple QD layers with different deposition amount to form each QD layer, or with different composition and thickness of strain reduce layer (SRL), or with dots in compositionally modulated well structures [17].

By using stacking chirped multiple InAs QD layers capped with $\text{In}_x\text{Ga}_{1-x}\text{As}$ SRL of different indium composition, as well as introducing a first excited state transition, an SLD with a emission bandwidth of 121nm has been achieved under pulsed operation with its corresponding power of 1.3mW [29]. An SLD incorporating InAs QDs in compositionally modulated InGaAs quantum wells was studied, this design consist of multiple dot-in-well layers with different indium compositions within each well, also the indium compositions of each well is carefully engineered to overlap the spectral emission from the ground state and first excited state of individual DWELL layers. As a result, an emission bandwidth of 85nm has been achieved under continuous wave operation with an output power of 2.5mW [17].

Post-growth rapid thermal annealing process has been widely utilized to modify the

optical properties of self-assembled quantum dots. Due to In-Ga inter-diffusion between the QDs and the surrounding barrier layers [30, 31], a narrowing of bandwidth in photoluminescence spectrum and a large blue-shift in the emission spectrum have been observed, which are desirable for the fabrication of wavelength tunable lasers and photonic integrated circuits. It is also noted that under low annealing temperature or short annealing duration, the emission bandwidth from QD structures by annealing process could broaden, which is mainly attributed to the effect of the increased interface fluctuations between the QDs and the surrounding matrix [32]. In addition, small spectrum modulation/spectral dips are expected since the energy separation between the ground state and the excited state of QDs could be reduced by annealing process [33]. Zhang *et al*, have reported the realization of a 146nm broadband quantum dot superluminescent diode by using rapid thermal annealing process with it CW output power as high as 15mW [32].

Recently, multi-section QD SLDs have attracted a lot of attention due to its flexible device geometry that permits independent adjustment of the power and the spectral bandwidth in the ground state (GS) and the excited states (ES) of the QD. By using such a design, an emission spectrum of 164nm with its corresponding power of 1.5mW has been achieved under pulse operation at room temperature [21].

For OCT application, according to the equation 1.1, the axial resolution, that is the

coherence length, is proportional to λ_0^2 (center wavelength) and is inversely proportional to $\Delta\lambda$ (spectral bandwidth). For skin tissue imaging, λ_0 is fixed in the biological “window” 1200-1350nm (due to minimum scattering and absorption). This region has been well served by GaAs based quantum dot materials, with possible bandwidths of up to ~160nm, corresponding to a theoretical OCT resolution of 5-6 μ m (current state-of-the-art). These theoretical values, for OCT system application, are capable of detecting different cells in skin tissue with a typical cell size of ~6-10 μ m [2]. Pushing spectral coverage to e.g. 300nm, centered at 1200nm provides a theoretical OCT resolution of ~2 μ m, promising the prospect of sub-cellular imaging of skin tissue.

1.4 Outline of This Thesis

Chapter 2: Experimental Techniques

In chapter 2, the experimental techniques used in this thesis are outlined. This chapter can be divided into three parts: in the first part, I initially give a brief introduction to molecular beam epitaxy (MBE), as all the samples studied in this thesis were grown by this technique. A method of quantum dot formation by using the Stranski-Krastanow growth mode is then discussed since this method has been widely and successfully employed to grow self-assembled quantum dots (SAQD). Then, several important experimental techniques are described such as photoluminescence spectroscopy (PL), electroluminescence (EL), photocurrent spectroscopy (PC).

Chapter 3: Ultra-Broad Spontaneous Emission from a Hybrid QW/QD Structure

In chapter 3, I introduce the first vertical hybrid QW/QD structure for application in broadband light emitting sources. These structures consist of an InGaAs QW and six InAs dot-in-well (DWELL) layers. The single QW is designed to emit at a wavelength coincident with the second excited state of the QDs. I compare two hybrid QW/QD structures where the QW position is changed along with an all-QD control sample. I study the optoelectronic properties for these two hybrid structures through photoluminescence (PL), current-voltage (I-V), capacitance-voltage (C-V), photocurrent (PC), and spontaneous emission measurements. Two hybrid samples show essentially identical forward I-V response, and a very similar C-V, as well as very similar PC spectra. However, very different spontaneous emission at room temperature is observed, i.e. only one structure shows a strong QW emission at $\sim 1130\text{nm}$. Significantly, by using the optimal structure, due to the combined effects of QD ground states, first excited state, and QW emission, I show that a spontaneous emission spectrum with a bandwidth of 250 nm centered at $\sim 1.2 \mu\text{m}$ is achieved under CW operation at room temperature. In order to further investigate carrier transport effects in the two hybrid structures, spontaneous emission is studied as function of temperature. The observed (calculated) differences in the activation energy of the QW emission obtained from Arrhenius plot (modeling of the band structure) for these two structures reflect the differences in the thermal energy required for electron and hole escape, which are also studied in this chapter.

Chapter 4: Gain and Lasing Characteristics of Hybrid QW/QD Laser

In chapter 4, I focus on the n-side hybrid QW/QD structure. I show that a positive modal gain spanning $\sim 300\text{nm}$, covering the wavelength range of $1100 - 1400\text{nm}$ is measured from the segmented contact device. I also report on simultaneous three-state lasing at room temperature, via ground state (GS), first excited state (ES1) of the QD and the lowest energy transition of a single QW for hybrid QW/QD lasers. I spectroscopically study lasers of different cavity lengths. By changing the cavity length/optical loss, different lasing sequences are observed. Additionally, I compare the hybrid QW/QD laser to a QD-only control device. I show that, for the hybrid QW/QD laser, the threshold current density for achieving simultaneous three-state lasing has been significantly reduced.

Chapter 5: Realization of Ultra-Broad Bandwidth Superluminescent Diodes Using Hybrid QW/QD Structure

In this chapter, I report on the first hybrid QW/QD superluminescent diode. In addition to the QD ground state (GS) transition, the QD first excited state (ES1) transition and the lowest energy transition of single QW (e1-hh1 transition), I show that emission from high order QW transitions (e1-hh2 and e1-hh3) at high current density, contributes to enhancing the spectral bandwidth by $\sim 70\text{nm}$. As a result, due to the combined contribution to the emission spectrum from QD GS, QD ES1, and the QW, a 3-dB emission bandwidth of $\sim 290\text{nm}$ centered at $\sim 1200\text{nm}$ with a

corresponding output power of 2.4mW is achieved at room temperature. I then assess the hybrid QW/QD SLD for application in an OCT system. The ultra-broad bandwidth enables a predicted axial resolution of $\sim 2.9\mu\text{m}$, a factor of 3-5 times better than standard OCT system using SLDs, indicating that this hybrid QW/QDs SLDs is highly desirable for application in OCT systems for submicron single cellular/molecular imaging.

Chapter 6: Study of QD-Induced Strain Modulation of a QW

Following on from chapter 5, in order to fully understand the origin of the high order QW transitions in the hybrid QW/QD structure, I focus attention on spatial strain modulation of the QW due to the QD layers. I experimentally demonstrate that in the hybrid QW/QD structure, the QD-induced strain can result in both broader QW transitions, and more pronounced high order transitions, both of which can be expected to be beneficial for broad spectral bandwidth device.

Chapter 7: New Design of Hybrid QW/QD Structure for High Power and Broad Bandwidth Superluminescent Diodes

Based on my previous work, in this chapter, I report the latest results on new device designs utilizing a larger number of QD layers with higher areal density transferring my designs to a commercial QD epitaxy company. The state separation of the devices is also higher than previous structures, leading to broader theoretical bandwidths and high temperature operation. Four structures are studied including three hybrid QW/QD structures and a QD-only structure. All of the hybrid QW/QD structures have

a 1080nm InGaAs QW positioned closest to the n-contact, and nine QD layers. I study designs for chirped and un-chirped structures. I show that, spectrally positioning the dots to overlap (chirping) provides smaller spectral modulation to the spontaneous emission spectra, yet still allows the identification of the QD GS and ES1, and QW. I also compare the designs for an asymmetric triangular QW and a rectangular symmetrical QW. Both structures are grown using a digital alloy approximation. I show that the modulation of the QW due to triangular In composition profile, also makes high order QW transitions more pronounced via PC spectroscopy. Finally, I show spontaneous emission spectra from a final structure consisting of chirped QDs and digital alloy triangular QW) under CW operation, without active cooling. The combined effect of this design and self-heating (Joule heating) produces a spontaneous emission spectrum spanning 350nm.

Chapter 8: Conclusion

This chapter summarizes the whole of my work.

Reference

- [1] T. H. Ko, D. C. Adler, J. G. Fujimoto, D. Mamedov, V. Prokhorov, V. Shidlovski, and S. Yakubovich, “Ultrahigh resolution optical coherence tomography imaging with a broadband superluminescent diode light source,” *Opt. Express.*, vol. **12**, pp. 2112–2119, May. 2004.
- [2] D. Huang, E. A. Swanson, C. P. Lin, J. S. Schuman, W.G. Stinson, W. Chang, M. R. Hee, T. Flotte, K. Gregory, C. A. Puliafito, and J. G. Fujimoto, “optical coherence tomography,” *Science.*, vol. **254**, pp. 1178-1181, Nov. 1991.
- [3] A. F. Fercher, W. Drexler, C. K. Hitzenberger, and T. Lasser, “Optical coherence tomography—principles and applications,” *Rep. Prog. Phys.*, vol. **66**, pp. 239–303, Jan. 2003.
- [4] Y. Wang, J. S. Nelson, and Z. Chen, “Optimal wavelength for ultrahigh resolution optical coherence tomography,” *Opt. Exp.*, vol. **11**, pp. 1411-1417, Jun. 2003.
- [5] J. Welzel, E. Lankeau, G. Hüttmann, and R. Birngruber, “OCT in dermatology,” in *Optical Coherence Tomography*. Berlin, Germany/New York: Springer-Verlag, 2008, pp. 1103–1122.
- [6] S. Chen, K. Zhou, Z. Zhang, J. R. Orchard, D. T. D. Childs, M. Hugues, O. Wada, and R. A. Hogg, “Hybrid Quantum Well/Quantum Dot Structure for Broad Spectral Bandwidth Emitters,” *IEEE J. Select. Topics Quantum Electron.*, vol. **19**, no. 4, pp.1900209-1900209-9, Jul/Aug. 2013.
- [7] A. F. Fercher, K. Mengedoht, and W. Werner, “Eye-length measurement by interferometry with partially coherent light,” *Opt. Lett.*, vol. **13**, pp.186-188, Mar. 1988.
- [8] C. Ackay, P. Parrein, and J. P. Rolland, “Estimation of longitudinal resolution in optical coherence imaging,” *Appl. Opt.*, vol. **41**, pp. 5256– 5262, Aug. 2002.
- [9] R. Leitgeb, C. K. Hitzenberger, and A. F. Fercher, “Performance of fourier domain vs. time domain optical coherence tomography,” *Opt. Exp.*, vol. **11**, pp. 889-894, Apr. 2003.
- [10] J. M. Schmitt, “Optical Coherence Tomography (OCT): A Review,” *IEEE J. Select. Topics Quantum Electron.*, vol. **5**, pp.1205-1215, Jul/Aug. 1999.
- [11] W. K. Burns, C. L. Chen, and R. P. Moeller, “Fiber-optic gyroscopes with broad-band sources,” *J. Lightw. Technol.*, vol. **LT-1**, pp. 98–105, Mar. 1983.
- [12] S. S. Wagner, T. E. Chapuran, “Broadband high-density WDM transmission using

- superluminescent diodes,” *Electron. Lett.*, vol. 26, pp. 696-697, 1990.
- [13] Z. Y. Zhang, R. A. Hogg, X. Q. Lv, and Z. G. Wang, “Self-assembled quantum dot superluminescent light-emitting diodes,” *Adv. Opt. Photon.*, vol. 2, pp. 201-228, Jan. 2010.
- [14] V. Shidlovski, “Superluminescent diodes. Short overview of device operation principles and performance parameters,” SuperlumDiodes Ltd., 2004.
- [15] T. P. Lee, C. A. Burrus, and B. I. Miller, “A Stripe-Geometry Double-Heterostructure Amplified-Spontaneous-Emission (superluminescent) Diode,” *IEEE J. Quant. Electron.*, vol. QE-9, pp.820-828, Aug. 1973.
- [16] Z. Y. Zhang, Z. G. Zhang, B. Xu, P. Jin, Zh. Sun, and F. Q. Liu, “High performance quantum-dot superluminescent diodes,” *IEEE Photon. Technol. Lett.*, vol. 16, pp. 27-19, 2004.
- [17] S. K. Ray, K. M. Groom, M. D. Beattie, H. Y. Liu, M. Hopkinson, and R. A. Hogg, “Broad-band superluminescent light-emitting diodes incorporating quantum dots in compositionally modulated quantum well,” *IEEE Photon. Technol. Lett.*, vol. 18, pp. 58-60, 2006.
- [18] Z. Y. Zhang, R.A. Hogg, P. Jin, T.L. Choi, B. Xu, and Z.G. Wang, “High power quantum dot superluminescent LED with broadband drive current insensitive emission spectra using a tapered active region,” *IEEE Photon. Technol. Lett.*, vol. 20, pp. 782-784, May. 2008
- [19] C. F. Lin, “Superluminescent diodes with angled facet etched by chemically assisted ion beam etching,” *Electron. Lett.*, vol. 27, no. 11, pp. 968-970, May. 1991.
- [20] Z. Y. Zhang, I. J. Luxmoore, C. Y. Jin, H. Y. Liu, Q. Jiang, K. M. Groom, D. T. Childs, M. Hopkinson, A. G. Cullis, R. A. Hogg, “Effect of facet angle on effective facet reflectivity and operating characteristics of quantum dot edge emitting lasers and superluminescent light emitting diodes”, *Appl. Phys. Lett.*, vol. 91, no. 8, pp. 081112-1 – 081112-3, Aug. 2007.
- [21] Y. Xin, A. Martinez, T. A. Nilsen, A. Moscho, Y. Li, A. L. Gray, and L. F. Lester, “1.3 μm quantum dot multi-section superluminescent diode with extremely broad bandwidth ($>150\text{ nm}$),” *IEEE Photon. Technol. Lett.*, vol. 19, pp. 501–503, Apr. 2007.
- [22] W. Zhou, O. Qasaimeh, J. Phillips, S. Krishna, and P. Bhattacharya, “Bias-controlled wavelength switching in coupled-cavity $\text{In}_{0.4}\text{Ga}_{0.6}\text{As}/\text{GaAs}$ self-organized quantum dot lasers,” *Appl. Phys. Lett.*, vol. 74, pp. 783-785, Feb. 1999.

- [23] J. D. Thomson, H. D. Summers, P. J. Hulyer, P. M. Snowton, and P. Blood, "Determination of single-pass optical gain and internal loss using a multisection device," *Appl. Phys. Lett.*, vol. **75**, pp. 2527-2529, Aug. 1999.
- [24] G. M. Lewis, P. M. Snowton, J. D. Thomson, H. D. Summers, and P. Blood, "Measurement of true spontaneous emission spectra from the facet of diode laser structures," *Appl. Phys. Lett.*, vol. **80**, pp. 1-3, Jan. 2002.
- [25] V. M. Ustinov, A. E. Zhukov, A. Y. Egorov, and N. A. Maleev, (2003) *Quantum dot lasers*, Oxford, New York.
- [26] D. Bimberg, M. Grundman, and N. N. Ledentsov, (1999) *Quantum dot heterostructures*, Wiley, New York.
- [27] Y. Ebiko, S. Muto, D. Suzuki, S. Itoh, K. Shiramine, T. Haga, Y. Nakata, and N. Yokoyama, "Island size scaling in InAs/GaAs self-assembled quantum dots," *Phys. Rev. Lett.*, vol. **80**, pp. 1650-2653, 1998.
- [28] M. Rossetti, L. H. Li, A. Markus, A. Fiore, L. Occhi, C. Velez, S. Mikhrin, I. Krestnikov, and A. Kovsh, "Characterization and modeling of broad spectrum InAs-GaAs quantum-dot superluminescent diodes emitting at 1.2–1.3 μm ," *IEEE J. Quantum Electron.*, Vol. **43**, pp. 676–686, 2007.
- [29] L. H. Li, M. Rossetti, A. Fiore, L. Occhi, and C. Velez, "Wide emission spectrum from superluminescent diodes with chirped quantum dot multilayer," *Electron. Lett.*, Vol. **41**, pp. 41–43, 2005.
- [30] F. Heinrichsdor, M. Grundmann, O. Stier, A. Krost, and D. Bimberg, "Influence of In / Ga intermixing on the optical properties of InGaAs / GaAs quantum dots," *J. Cryst. Growth.*, Vol. **195**, pp. 540–545, 1998.
- [31] S. Fafard and C. N. Allen, "Intermixing in quantum-dot ensembles with sharp adjustable shells," *Appl. Phys. Lett.*, vol. **75**, pp. 2374–2376 (1999).
- [32] Z. Y. Zhang, R. A. Hogg, B. Xu, P. Jin, and Z. G. Wang, "Realization of extremely broadband quantum-dot superluminescent light-emitting diodes by rapid thermal-annealing process," *Opt Lett.*, vol. **33**, pp. 1210–1212, 2008.
- [33] Z. Y. Zhang, Q. Jiang, I. J. Luxmoore, and R. A. Hogg, "A *p*-type-doped quantum dot superluminescent LED with broadband and flat-topped emission spectra obtained by post-growth intermixing under a GaAs proximity cap," *Nanotechnology.*, vol. **20**, pp. 055204-1-4, 2009.

Chapter 2: Experimental Techniques

2.1 Introduction

In this chapter, the experimental techniques used in this thesis are outlined. This chapter is divided into three parts: in the first part, initially an introduction to molecular beam epitaxy (MBE) is given, as all the samples studied in this thesis are grown by this technique. A method of quantum dot formation by using the Stranski-Krastanow (SK) growth mode is then discussed since this method has been widely and successfully employed to grow self-assembled quantum dots (SAQD). Finally, several important experimental techniques are described such as photoluminescence (PL) spectroscopy, electroluminescence (EL), and photocurrent spectroscopy (PC).

2.2 Molecular Beam Epitaxy (MBE)

Molecular beam epitaxy (MBE) is a means of growing high purity epitaxial layers of compound semiconductor that was developed in the early 1970s [1, 2, 3]. Through almost 40 years of study, MBE has evolved into one of the most valuable techniques for growing *III-V* compound semiconductors as well as several other materials [3]. Due to the high degree of control of thickness, doping and composition with MBE, it is widely used in the development of optoelectronic and electric devices [3].

MBE takes place in an ultra-high vacuum environment (less than 10^{-11} Torr) [3], with thermal evaporated sources, the molecular beams are deposited on the heated crystalline substrate, forming high-quality thin epitaxial layers [3]. MBE has several important features, such as: low substrate temperatures which can effectively reduce the diffusion of impurities to obtain a steep impurity distribution of the epitaxial layers; low growth rates that are typically on the order of a few angstroms per second while the beams can be shuttered in a fraction of a second [3, 4], leading to atomically precise control of doping, composition and thickness of the epitaxial layers [3]. Also, under the high vacuum environment, the growth process and the surface of the sample can be analyzed and monitored *in situ*.

The MBE system is constituted by three main parts: a growth chamber, a buffer (preparation chamber), and a transfer chamber (load lock) [3]. Samples can be transferred into and out of any one vacuum chamber by the load lock while maintaining the vacuum conditions of other chambers [3]. The preparation chamber is used to prepare and store samples. Some material characterization can also be carried out in this chamber with the proper equipment. The growth chamber is the place where the epitaxial growth takes place.

The MBE growth chamber and several of its components are illustrated schematically in Fig. 2.1. The sample is loaded on the substrate stage, which is rotated at a certain speed to obtain uniform growth rate over the substrate [5, 6]. The molecular beams

are formed in heated effusions cells, which are independently heated. These effusion cells are thermally isolated by using a succession of heat shields. In a research type MBE system, the cells are located around 10-15 cm in front of the substrate holder [3, 7], once the incident angle is fixed, the beam intensities (growth rate) is mainly controlled by the cell temperature and the flux is regulated by a computer-controlled shutter positioning in front of each effusion cell.

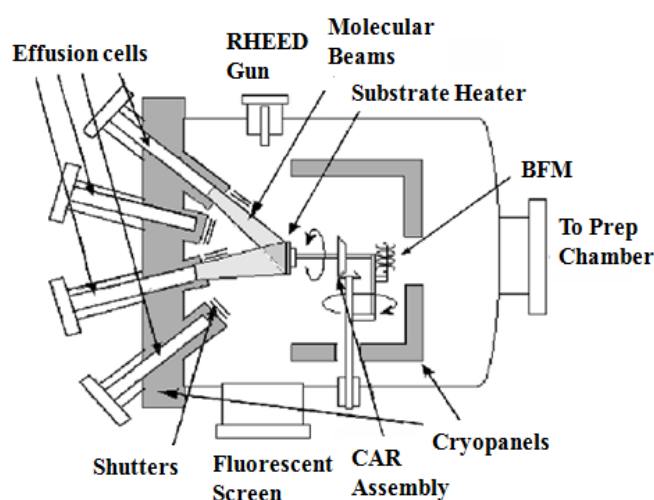


Fig. 2.1 Schematic diagram of a typical MBE system growth chamber [3].

To obtain high quality films, it is critical that the substrate surface is free of crystallographic and other defects, since these defects degrade the optoelectronic properties of the device. Auger electron spectroscopy was used to determine the wafer cleanliness in the preparation chamber [2]. But nowadays, “epi-ready” wafers, which are pre-cleaned and oxidized [3], are widely used. A thin oxide film is formed as a protective layer by the manufacturers, which can be removed in the growth chamber.

Reflection high energy electron diffraction (RHEED) is one of the most important tools for *in-situ* assessment of the epitaxial growth in MBE. The layout of the RHEED system is schematically shown in Fig. 2.1. The electrons emitted from the RHEED gun strike the sample surface at a very shallow angle ($\sim 0.5\text{-}3^\circ$) [3, 5, 6], resulting in a sensitive probe of the semiconductor surface [3]. The electrons are then reflected from the sample surface and strike the fluorescent screen forming a series of reflection and diffraction patterns, which provides useful information about the surface crystallography.

RHEED is an important *in situ* analytical instrument in MBE which can be used in many ways, for instance, it can be used to calibrate the substrate temperature [8], via the observation of the transition from an amorphous image to a streaky RHEED pattern when the oxide protective layer is removed, for example, the deoxidation temperature for GaAs is usually 600°C [3]. Also, the intensity oscillations of the RHEED can be used as an accurate and quick method for determining the growth rate since the oscillation frequency (period) corresponds to the monolayer growth rate [3, 8, 9]. By taking GaAs as an example, where a monolayer is the thickness of one full layer of Ga and one full layer of As atoms [3], a typical form of RHEED intensity oscillation is shown in Fig. 2.2 [8]. In addition, the RHEED pattern can be used for determining the formation of quantum dots. Since the two-dimensional growth (i.e. layer by layer) typically shows a stripe pattern in RHEED, the change of RHEED pattern from a stripe pattern to a discontinuous line or “spotty” pattern corresponds to

the two-dimensional (2D) to 3D growth mode transition. [10].

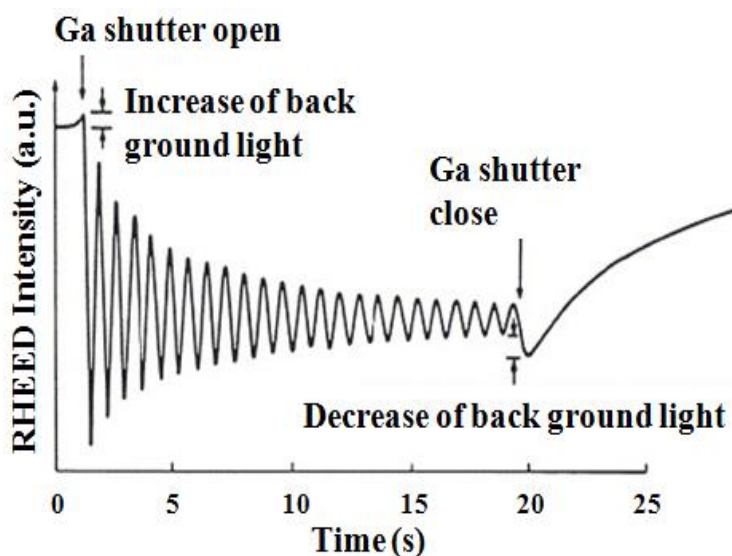


Fig. 2.2 An example of REHHD intensity oscillation of GaAs layer on a GaAs surface. The period corresponds to the growth rate of one monolayer of GaAs and the amplitude gradually decreases [3, 8].

2.3 A Method of Quantum Dots Formation: Stranski-Krastanow (S-K) Growth Mode

The drive for novel optoelectronic devices based on semiconductor nanostructures with reduced dimensionality has led to tremendous interest in the realization of quantum dot structures as a result of their unique properties for laser applications such as ultralow threshold current density and temperature insensitive operation, due to their discrete, zero-dimensional electronic states [11-14]. The phenomenon of island formation during the epitaxial growth of highly lattice-mismatched materials, i.e. the Stranski-Krastanow (S-K) growth mode [15], has been widely used to form relatively homogeneous QD ensembles [16-18].

Fig. 2.3 schematically illustrates the process of formation of InAs QDs observed during the epitaxial growth of InAs on GaAs (001) that has a lattice mismatch of 7.1%. For the initial growth of a few atomic layers, a smooth strained InAs layer forms a so-called wetting layer. As the epitaxial overgrowth proceeds, there is a concomitant increase of the strain energy of the layer, and prior to the incorporation of dislocations, the atoms tend to bunch up and form isolated, coherent QD islands [19, 20]. This spontaneous formation of QDs is energetically favorable, as the compressive strain can be elastically relaxed, therefore the strain energy can be effectively reduced within the QDs. Since the formation of QD clusters is a spontaneous process during the epitaxial growth, they are referred to as self-assembled QDs. [19]. The QD size can be tuned within a certain range by changing the epitaxial conditions of which the most important are the temperature of the substrate and the amount of deposited dot material [3]. Smaller dots emit photons of shorter wavelength with higher energies while larger dots emit photons of longer wavelength, corresponding to smaller energies, which is due to the combined effect of variation of carrier confinement and strain in the QDs.

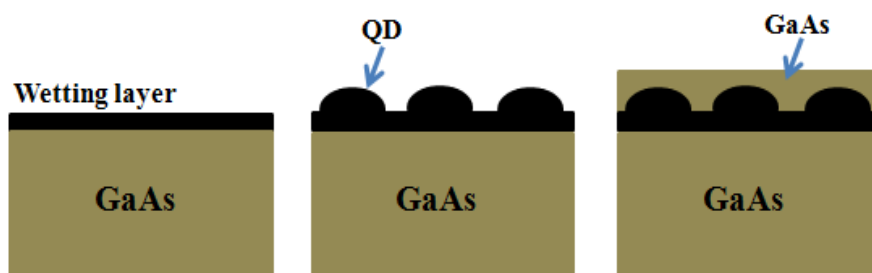


Fig. 2.3 Schematic diagram of S-K mode for growth of quantum dot [3, 24].

Self-assembled QDs by the S-K mode have a lot of advantages over other techniques. This is a relatively simple method to form a giant number of nanostructures (10^{10} - 10^{11} cm^{-2}) with relatively high uniformity ($\sim 10\%$) in size and composition. In addition, at adequate conditions, the QDs can be incorporated in the host material without dislocations and defects due to the spontaneous re-ordering in size caused by elastic relaxation and by strain-induced renormalization of the surface energy of facets [21-23].

In addition to S-K growth mode, Volmer-Weber (V-W) growth mode has also been utilized to growth QDs. Similar to S-K mode, in V-W growth mode, QDs are also obtained during epitaxial growth of one material on top of another one that has a smaller lattice constant [3], however, compared with S-K mode, lattice mismatch between two epitaxial layers in V-W mode is even larger, therefore, there will be no wetting layer formed in this case.

2.4 Experimental Techniques

2.4.1 Photoluminescence Spectroscopy

Photoluminescence (PL) is a process of the re-radiation of light after the absorption of incident photons. Fig.2.4 gives an overview of the main process of photoluminescence in a direct gap material such as GaAs. The incoming photons which are provided by an excitation source (the source can be any laser or lamp whose energy equals or exceeds the band gap of the material to be examined) are absorbed. This may inject electrons into the conduction band and holes into the valance band. For incident energies higher than the band-gap, the initially created electrons (holes) are located in states high up the conduction band (valance band), and they rapidly relax to the bottom of their bands by LO-phonon emission, acoustic phonon emission and carrier-carrier scattering to form a carrier population at the lattice temperature, before recombining by emitting photons. This process is indicated by the cascade of transitions shown in Fig. 2.4.

The electron and hole may subsequently attract each other by the Coulomb interaction to form a neutral pair that is an exciton, which can be conceived as a hydrogen-like system similar to hydrogen positronium atom with the electron and hole in a stable orbit around each other [24, 25]. There are two basic types of exciton are observed in the many crystalline materials. As illustrated schematically in Fig. 2.5 [24], they are the free exciton and the tightly bound exciton. Free excitons are delocalized states

which can move freely within the crystal. Due to their larger radius, the binding energy for free excitons is quite small, with typical values of around 0.01eV. Therefore, for many materials, the free excitons can only be clearly observed at low temperature since the maximum energy of thermal excited phonon at room temperature is around $k_B T \sim 25\text{meV}$ [3]. Compared with free excitons, tightly bound excitons have a much smaller radius in which case they are localized states that can be tightly trapped to specific atoms or molecules. The binding energy for bound excitons is around 0.1-1eV, which makes them stable even at room temperature.

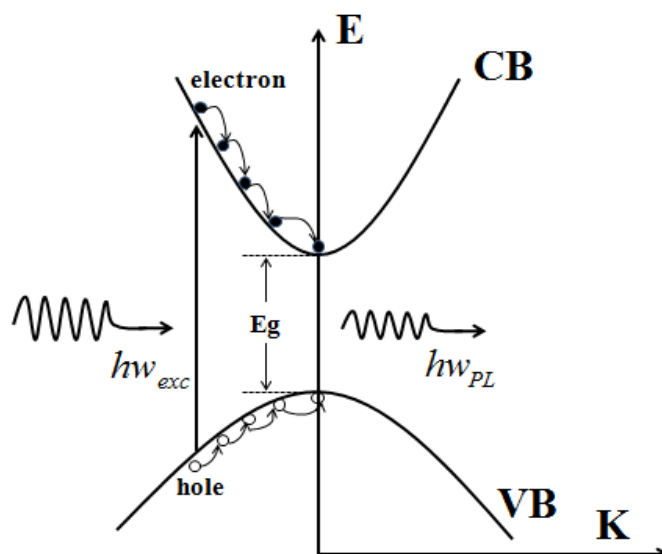


Fig. 2.4 Schematic diagram of the photoluminescence process [24].

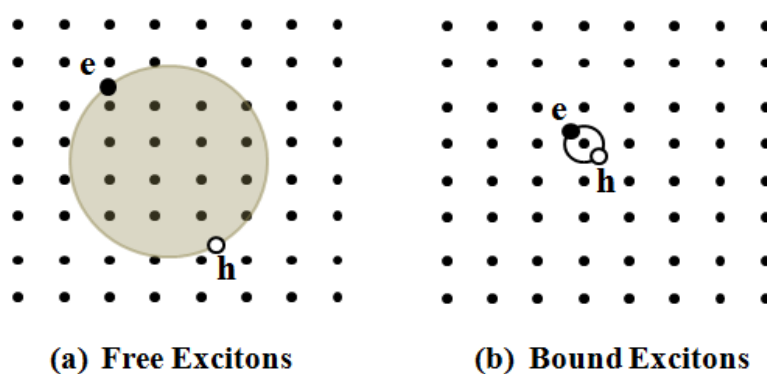


Fig. 2.5 Schematic diagram of a free-exciton and a tightly bound exciton [24].

Photoluminescence spectroscopy is a powerful contactless, non-destructive technique to investigate the optical properties of impurities in semiconductor material [26]. PL spectra can also be utilized to determine the bandgap of a semiconductor. This provides a method to quantify the elemental composition in compound semiconductors. In addition, individual spectral features observed in the PL spectra

can reveal impurities contained within the host material. The intensity of PL obtained from a material reflects the relative amount of radiative and nonradiative recombination rates. It is known that the non-radiative rates are usually related to impurities and defects, and so this technique can also be utilized to qualitatively monitor variations in material quality as a function of growth conditions [27].

For a bulk material such as $\text{Al}_x\text{Ga}_{1-x}\text{As}$ at low temperature, thermal broadening is effectively inhibited. It is then believed that the linewidth of the PL spectra are influenced by the inherent properties of the alloy material, therefore the fluctuation of the alloy composition over the area of excitation, which will be reflected in the energy of the luminescence, are responsible for the linewidth broadening of the luminescence peak. A detailed description of alloy broadening in the photoluminescence spectra of bulk materials has been presented by Schubert *et al* [28]. And, a detailed description of alloy broadening in QW can be found in J. Singh *et al*, [29]. For single ternary quantum well structures, taking say GaAs/ $\text{Al}_x\text{Ga}_{1-x}\text{As}$ quantum well as an example, there will also be a luminescence linewidth broadening, if there are fluctuations in the well width [30]. Therefore, the photoluminescence spectra provide a means to investigate the degree of perfection of the interface between *III-V* semiconductors.

With regard to QDs, two lineshape broadening mechanisms are usually described. They are inhomogeneous broadening and homogeneous broadening. Inhomogeneous broadening talk about the variation in QD size, composition with ensemble, while

homogeneous broadening related to the reduction in lifetime of individual QDs due to scattering with phonons and free carries and so on.

Photoluminescence spectra can be measured with an experimental arrangement as shown schematically in Fig. 2.6. The sample is mounted in a variable temperature cryostat and sample temperature can be controlled by temperature controller from 10K to 320K. The excitation source used is a commercial diode pumped solid state laser (DPSSL) driver where the photons can be continuously generated. The maximum power can be achieved in our PL setup is one watt, whereas in most of my experiments, only few to tens of milliwatts are often adequate to obtain good signal, depending on the material to be examined, along with the system and the detector sensitivity as well. Light excited by the laser passes through the optical chopper, where the light is “chopped” at ~50Hz, to provide a reference for the lock-in amplifier. The chopped light is collimated and illuminated on the sample mounted in cryostat. The PL signal undergoes dispersion through a DM 150 DOUBLE monochromator, which selects a wavelength to transmit to the detector. In our case, an InGaAs detector is used for the near-infrared range (1.1-1.3 μ m). The resolution of the system is determined by the slit width of the monochromator. By scanning the monochromator and measuring the intensity at each wavelength with a sensitive detector the PL spectrum can be recorded with the lock-in amplifier.

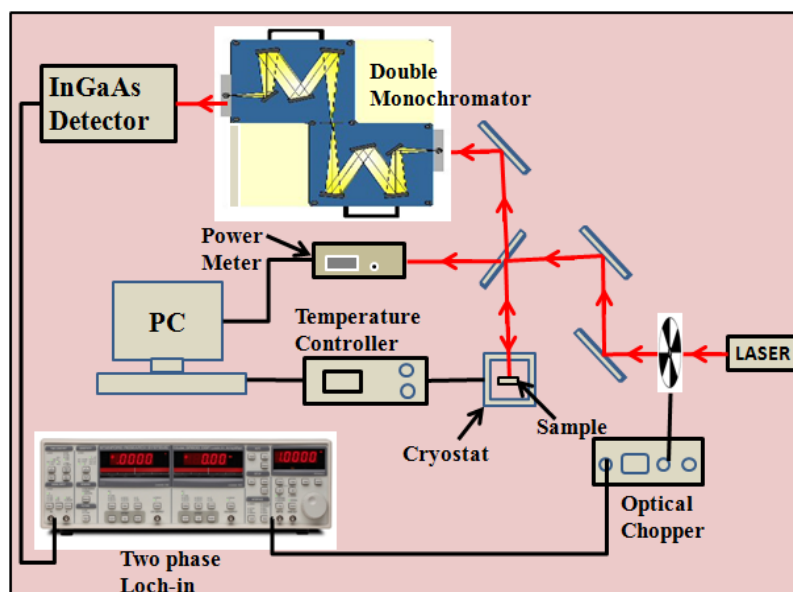


Fig. 2.6 Schematic diagram of photoluminescence experimental setup.

Optical choppers are widely used in spectroscopy experiments in combination with lock-in amplifier, as it is a common way of obtaining high signal-noise ratio, since using the optical chopper gives a frequency dependent signal and the lock-in will only amplify signals modulated at that specific frequency.

2.4.2 Electroluminescence

Electroluminescence (EL) is a process by which light is generated by passing an electrical current through an optoelectronic device. Light emitting diodes and laser diodes are typical electroluminescent devices. The microscopic mechanisms that determine the emission spectrum are exactly the same as photoluminescence discussed above. The key difference is that the carriers (i.e. electron and hole pairs) are injected electronically rather than optically which varies their distribution within the structure.

A schematic diagram of the layer structure and circuit for a typical electroluminescent device is shown in Fig. 2.7 [24]. The device consists of several epitaxial layers grown on a thick substrate. The epitaxial layers are made up of a p-n junction with an active region at the junction. Under forward bias operation, electrons are injected from the n-type layer and holes are injected from the p-type layer, electrons and holes are then recombined in the intrinsic/active region. In direct band gap semiconductors, the radiative recombination lifetime is \sim ns scale whilst on the other hand, in indirect band gap semiconductors; the radiative recombination lifetime is \sim μ s. As a consequence most of the recombination is non-radiative releasing heat to the lattice. This long radiative lifetime in the indirect band gap semiconductors is because the valance band maximum and the conduction band minimum are at different point in the Brillouin zone, the conservation of momentum requires that a phonon must either be emitted or absorbed. This second-order process (emitting both a photon and phonon) during the transition makes the radiative lifetime much longer than for direct band-gap transitions.

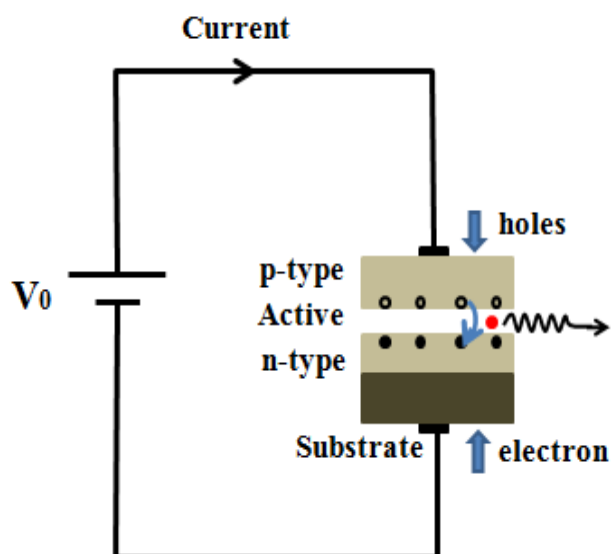


Fig. 2.7 Schematic diagram of circuit for electroluminescent device [24].

2.4.3 Photocurrent Spectroscopy (PC)

Photocurrent (PC) spectroscopy is a direct, sensitive and relative simple absorption related technique [31], which has been widely utilized to investigate the electronic properties of semiconductor low dimensional structures, such as quantum well, and quantum dots [31, 32]. It combines the advantages of both electrical and optical techniques [33, 34]. PC is a two-step process. Firstly, absorption in the QW/QD is governed by the electron-hole wave function overlap. Secondly, the escape of carriers and their transport to the contacts is required to generate a current. Therefore, the observed PC signal can provide further information about the ratio of recombination and escape rates of photo-generated carriers [35].

Fig.2.8 shows a schematic diagram of the experimental apparatus used to measure the PC spectra. The PC experiment is carried out on optical p-i-n mesa diodes of

diameter $400\mu\text{m}$. Light from a tungsten lamp source, dispersed by a monochromator, is focused on the p-type surface of the sample; an optical chopper is applied to modulate the incident light. Therefore at this frequency, a modulation of the sample current is induced. A DC bias is applied to the sample by the voltage source, varying the reverse bias results in an electric field oriented along the growth direction. The PC signal is recorded by using standard lock-in amplifier techniques.

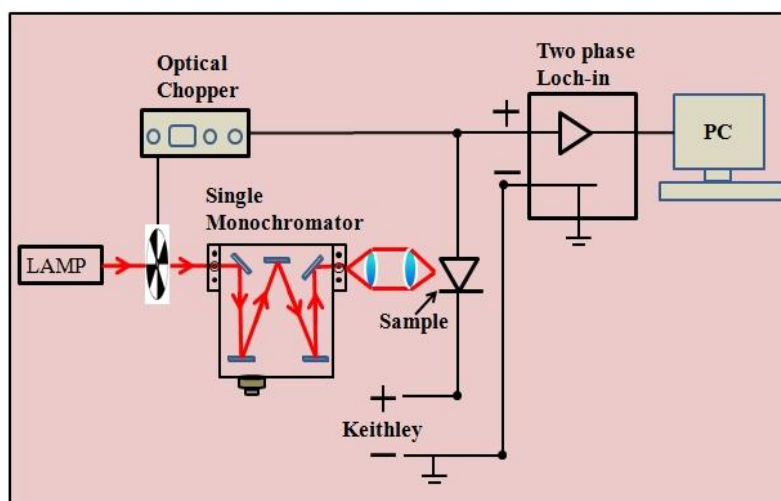


Fig. 2.8 Schematic diagram of photocurrent experimental setup.

The band diagram for a typical p-i-n structure is illustrated in Fig. 2.9 [33], an interband absorption process is indicated, and under reverse bias large electric fields can be achieved in the intrinsic region with negligible dark current through the device. Photons absorbed in the intrinsic region generate electron-hole pairs, which are rapidly swept towards the contacts by the E-field; the carriers then escape to the external circuit, either by tunneling or by thermal excitation, thus leading to the observed PC signal.

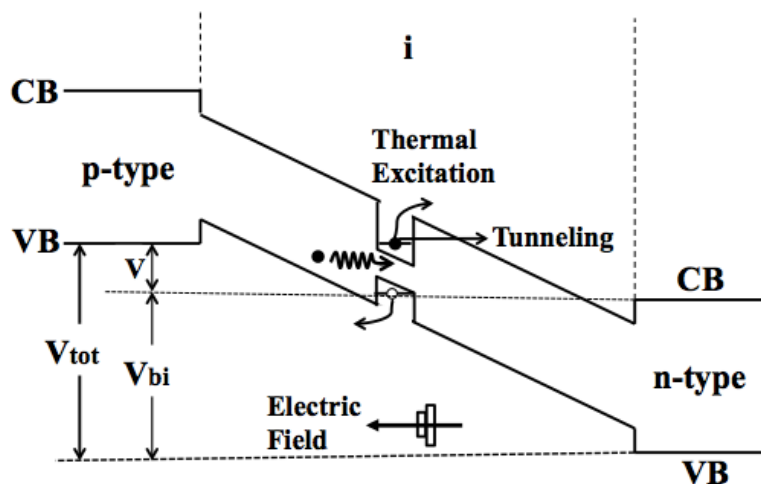


Fig. 2.9 Schematic band diagram of a heterojunction p-i-n device under reverse bias V [31].

Comparison between the PL and PC can reveal further information about the quality of the heterostructure [36]. The existence of a redshift of the PL emission with respect to the absorption observed in PC is known as Stokes' shift. The Stokes' shift is expected to be zero in a perfect system. However, the variation of well widths and/or compositional fluctuations during the epitaxial growth leads to the localization of recombining excitons, which results in the Stokes' shift.

Reference

- [1] Cho, "Film deposition by molecular beam epitaxy techniques," *J. Vac. Sci. Technol.*, vol. **8**, pp. S31-S38, 1971.
- [2] A. Cho, and J. Arthur, "molecular beam epitaxy," *Prog. Solid-State Chem.*, vol. **10**, pp. 157-192, 1975.
- [3] V. M. Ustinov, A. E. Zhukov, A. Y. Egorov, and N. A. Maleev, *Quantum dot lasers*, Oxford, New York, 2003.
- [4] G. Turner, B. Nechay, S. Eglash, "Frequency-domain analysis of time dependant reflection high-energy electron diffraction intensity data," *J. Vac. Sci. Technol.*, vol. **B8**, pp. 283-287, 1990.
- [5] A. Y. Cho and K. Y. Cheng, "Growth of extremely uniform layers by rotating substrate holder with molecular beam epitaxy for applications to electro-optic and microwave devices," *Appl. Phys. Lett.*, vol. **38**, no. 5 pp. 360-362, 1981.
- [6] K. Y. Cheng, A. Y. Cho, and W. R. Wagner, "Molecular-beam epitaxial growth of uniform $\text{Ga}_{0.47}\text{In}_{0.53}\text{As}$ with a rotating sample holder," *Appl. Phys. Lett.*, vol. 39, no. 8. pp. 607-609, 1981.
- [7] B. A. Joyce, "molecular beam epitaxy," *Rep. Prog. Phys.*, vol. **48**, pp. 1637-1697, 1985.
- [8] J. H. Neave, B. A. Joyce, P. J. Dobson, N. Norton, "Dynamics of film growth of GaAs by MBE from Rheed observations," *Appl. Phys. A.*, vol. **31**, no. 1, pp. 1-8, 1983.
- [9] J. Harris, B. Joyce, and P. Dobson, "Oscillations in the surface structure of Sn-doped GaAs during growth by MBE," *Surf. Sci.* vol. **103**, pp. L90-L96, 1981.
- [10] R. P. Campion, K. W. Edmonds, L. X. Zhao, K. Y. Wang, C. T. Foxon, B. L. Gallagher, C. R. Staddon, "The growth of GaMnAs films by molecular beam epitaxy using arsenic dimmers," *J. Cryst. Growth.*, vol. **251**, no. 1-4, pp. 311-316, 2003.
- [11] Y. Arakawa and H. Sakaki, "Multidimensional quantum well laser and temperature dependence of its threshold current," *Appl. Phys. Lett.*, vol. **40**, no. 11, pp. 939-941, 1982.
- [12] D. Bimberg, N. Kirstaedter, N. N. Ledentsov, Zh. I. Alferov, P. S. Kop'ev, V. M. Ustinov, "InGaAs-GaAs quantum-dot lasers," *IEEE J. Sel. Top. Quantum Electron.*, vol. **3**, no. 2, pp. 196-205, 1997.

- [13] F. Heinrichsdorff, M.-H. Mao, N. Kirstaedter, A. Krost, D. Bimberg, A. O. Kosogov, and P. Werner, “Room-temperature continuous-wave lasing from stacked InAs/GaAs quantum dots grown by metalorganic chemical vapor deposition,” *Appl. Phys. Lett.*, vol. **71**, no. 1, pp. 22-24, 1997.
- [14] J. C. Campbell, D. L. Huffaker, H. Deng, D. G. Deppe, “Quantum dot resonant cavity photodiode with operation near 1.3 μm wavelength,” *Electron Lett.*, vol. **33**, no. 15, pp. 1337-1339, 1997.
- [15] N. Stranski and L. Krastanov *Sitzungsber. Akad. Wiss. Wien, Math.-Naturwiss. Kl., Abt. 2B* **146**, 797 (1938).
- [16] D. J. Eaglesham, and M. Cerullo, “Dislocation-free Stranski-Krastanow growth of Ge on Si(100),” *Phys. Rev. Lett.*, vol. **64**, no.16, pp. 1943–1946, 1990.
- [17] D. Leonard, K. Pond, and P. M. Petroff, “Critical layer thickness for self-assembled InAs islands on GaAs,” *Phys. Rev. B.*, vol. **50**, no. 16, pp. 11687–11692, 1994.
- [18] I. Mukhametzhanov, R. Heitz, J. Zeng, P. Chen, and A. Madhukar, “Independent manipulation of density and size of stress-driven self-assembled quantum dots,” *Appl. Phys. Lett.*, vol. **73**, no. 13, pp. 1841-1843, 1998.
- [19] W. Seifert, N. Carlsson, M. Miller, M-E. Pistol, L. Samuelson and L. R. Walle, “In-site growth of quantum dot structures by the Stranski-Krastanow growth mode,” *Prog. Crystal Growth and Charact.*, Vol. 33, pp. 423-471, 1996.
- [20] P. B. Joyce, T. J. Krzyzewski, G. R. Bell, B. A. Joyce, T. S. Jones, “Composition of InAs quantum dots on GaAs(001): Direct evidence for (In, Ga)As alloying,” *Phys. Rev. B.*, vol. 58, pp. R15981–R15984, 1998.
- [21] V. A. Shchukin, N. N. Ledentsov, P. S. Kop'ev, and D. Bimberg, “Spontaneous Ordering of Arrays of Coherent Strained Islands,” *Phys. Rev. Lett.*, vol. **75**, pp. 2968–2971, 1995.
- [22] V.A. Shchukin, N. N. Ledentsov, M. Grundmann, P.S. Kop'ev, D. Bimberg, “Strain-induced formation and tuning of ordered nanostructures on crystal surfaces,” *Surf. Sci.*, vol. **352-354**, pp. 117-122, 1996.
- [23] N. N. Ledentsov, M. Grundmann, N. Kirstaedter, O. Schmidt, R. Heitz, J. Böhrer, D. Bimberg, V. M. Ustinov, V.A. Shchukin, A. Yu. Egorov, A.E. Zhukov, S. Zaitsev, P. S. Kop'ev, Zh. I. Alferov, S. S. Ruvimov, A. O. Kosogov, P. Werner, U. Gösele, J. Heydenreich, “Ordered arrays of quantum dots: Formation, electronic spectra, relaxation phenomena, lasing,” *Solid-State Electron.*, vol. **40**, no. 1-8, pp.785-798, 1996.
- [24] M. Fox. *Optical Properties of Solids*. Oxford, New York. (2001).

- [25] D. L. Dexter and R. S. Knox. *Excitons*. Wiley, New York. (1965).
- [26] H. B. Bebb, and E. W. Williams. *Semiconductors and Semimetals*. Academic Press. New York. 1972; P. J. Dean, “Photoluminescence as a diagnostic of semiconductors,” *Prog. Cryst. Growth Charact.*, vol. **5**, no. 1-2, pp. 89-174, 1982.
- [27] S. Perkowitz. *Optical Characterization of Semiconductor: Infrared, Raman, and Photoluminescence Spectroscopy*. Academic Press. London. (1993).
- [28] E. F. Schubert, E. O. Göbel, Y. Horikoshi, K. Ploog, and H. J. Queisser, “Alloy broadening in photoluminescence spectra of $\text{Al}_x\text{Ga}_{1-x}\text{As}$,” *Phys. Rev. B.*, vol. **30**, no. 2, pp. 813–820, 1984.
- [29] J. Singh and K. K. Bajaj, “Role of interface roughness and alloy disorder in photoluminescence in quantum-well structure,” *J. Appl. Phys.*, vol. **57**, pp. 5433-5437, 1985.
- [30] C. Weisbuch, R. Dingle, A.C. Gossard, W. Wiegmann, “Optical characterization of interface disorder in GaAs-Ga $_{1-x}$ Al $_x$ As multi-quantum well structures,” *Sol. Stat. Comm.*, vol. **38**, no. 8, pp. 709-712, 1981.
- [31] P. W. Fry, I. E. Itskevich, S. R. Parnell, J. J. Finley, L. R. Wilson, K. L. Schumacher, D. J. Mowbray, M. S. Skolnick, M. Al-Khafaji, A. G. Cullis, M. Hopkinson, J. C. Clark, and G. Hill, “Photocurrent spectroscopy of InAs/GaAs self-assembled quantum dots,” *Phys. Rev. B.*, vol. **62**, no. 24, pp. 16784–16791, 2000.
- [32] R. T. Collins, K. V. Klitzing, and K. Ploog, “Photocurrent spectroscopy of GaAs/ $\text{Al}_x\text{Ga}_{1-x}\text{As}$ quantum wells in an electric field,” *Phys. Rev. B.*, vol. **33**, no. 6, pp. 4378–4381, 1986.
- [33] P. W. Fry, I. E. Itskevich, D. J. Mowbray, M. S. Skolnick, J. J. Finley, J. A. Barker, E. P. O'Reilly, L. R. Wilson, I. A. Larkin, P. A. Maksym, M. Hopkinson, M. Al-Khafaji, J. P. R. David, A. G. Cullis, G. Hill, and J. C. Clark, “Inverted Electron-Hole Alignment in InAs-GaAs Self-Assembled Quantum Dots,” *Phys. Rev. Lett.*, vol. **84**, no. 4, pp. 733–736, 2000.
- [34] W.-H. Chang, T. M. Hsu, C. C. Huang, S. L. Hsu, C. Y. Lai, N. T. Yeh, T. E. Nee, and J.-I. Chyi, “Photocurrent studies of the carrier escape process from InAs self-assembled quantum dots,” *Phys. Rev. B.*, vol. **62**, no. 6, pp. 6959, 2000.
- [35] P. N. Brunkov, A. Patan, A. Levin, L. Eaves, P. C. Main Yu. G. Musikhin, B. V. Volovik, A. E. Zhukov, V. M. Ustinov, and S. G. Konnikov, “Photocurrent and capacitance spectroscopy of Schottky barrier structures incorporating InAs/GaAs quantum dots,” *Phys. Rev. B.*, vol. **65**, no. 8, pp. 085326-1 - 085326-6, 2002.

- [36] C. Delalande, G. Bastard, J. Orgonasi, J. A. Brum, H. W. Liu, M. Voos, G. Weimann and W. Schlapp, “Many-Body Effects in a Modulation-Doped Semiconductor Quantum Well,” *Phys. Rev. Lett.*, vol. **59**, no. 23, pp. 2690-2692, 1987.

Chapter 3: Ultra-Broad Spontaneous Emission from a Hybrid QW/QD Structure

3.1 Introduction

In this chapter, the first vertical hybrid QW/QD structure for application in broadband light emitting sources is introduced. These structures consist of an InGaAs QW and six InAs dot-in-well (DWELL) layers. The single QW is designed to emit at a wavelength coincident with the second excited state of the QD. I compare two hybrid QW/QD structures where the QW position within the multi-layer stack is changed in addition to an all-QD control sample. I study the optoelectronic properties for these two hybrid structures through photoluminescence (PL), current-voltage (I-V), capacitance-voltage (C-V), photocurrent (PC), and spontaneous emission measurements. Two hybrid samples show essentially identical forward I-V response, and a very similar C-V, as well as very similar PC spectra. However, very different spontaneous emissions at room temperature are observed, i.e. only one structure shows a strong QW emission at ~1130nm. Significantly, by using the optimal structure, due to the combined effects of QD ground states, first excited state, and QW emission, a spontaneous emission spectrum with a bandwidth of 250 nm centered at ~ 1.2 μm is achieved under CW operation at room temperature. In order to further investigate the carrier transport effects in the two hybrid structures,

spontaneous emission is studied as a function of temperature. The observed (calculated) differences in the activation energy of the QW emission obtained from Arrhenius plot (modeling of the band structure) for these two structures reflect the differences in the thermal energy required for electron and hole escape, which is also studied in this chapter.

3.2 Background

The realization of broad spectral band-width emitters and amplifiers is of considerable interest for a range of applications such as optical coherence tomography (OCT), fiber-optic gyroscopes, and test wavelength division multiplexing (WDM) systems [1, 2, 3]. In particular, it has been demonstrated that broadband sources operating at a central wavelength in the biological “window”, $\sim 1000\text{-}1300\text{nm}$ offer the possibility to perform OCT imaging with high quality and deep penetration in biological tissue. For instance, typically $\sim 1050\text{nm}$ [4, 5] is used for ophthalmology and $\sim 1200\text{-}1300\text{nm}$ [6] is used for imaging skin tissue due to the minimum of optical dispersion in water, and the minimum in scattering and absorption, respectively. Devices with broad bandwidth (e.g. superluminescent diodes (SLDs)) are required in order to improve the axial resolution in OCT systems, therefore enabling the instruments to distinguish finer features in specimens.

To achieve broad bandwidth, various methods have been pursued, such as using chirped QWs [7], QW intermixing [8], or introducing higher-order transitions of the

QW [9]. However, the engineering of broad spectral bandwidth QW devices is challenging due to issues with even carrier distribution and photon re-absorption in asymmetric multi-QW structures [10]. Active QW intermixed devices are also challenging, and have not been reported with characteristics suitable for application [11].

Most recently, self-assembled QD-based devices have attracted significant attention due to their naturally large inhomogeneous size distribution and state-filling effects when grown by the Stranski-Krastanow mode [12, 13]. A broadened emission can be achieved by chirping the emission energy of layers in a multilayer stack [14], growing an inhomogeneous dot distribution [15], or post-growth annealing [16]. In these QD-based amplifiers and superluminescent diodes, the maximum spectral bandwidth is achieved when the gain due to the first excited state and the ground state are balanced. However, when this requirement is satisfied, there is a significant absorption in the second excited states, and the increasing degeneracy of higher energy QD states limits the 3 dB bandwidth to around 150 nm [13, 16, 17]. This situation is schematically demonstrated in Fig. 3.1, where the modal gain for the QD ground state, first excited state and second excited state is empirically modeled as a function of average number of carriers per QD (discussion with Richard Hogg). This is done using a random population [18] and Gaussian distributions for the gain in each of the three states. The linewidths of the states is selected to match results obtained from QD lasers measured within our group [19, 20].

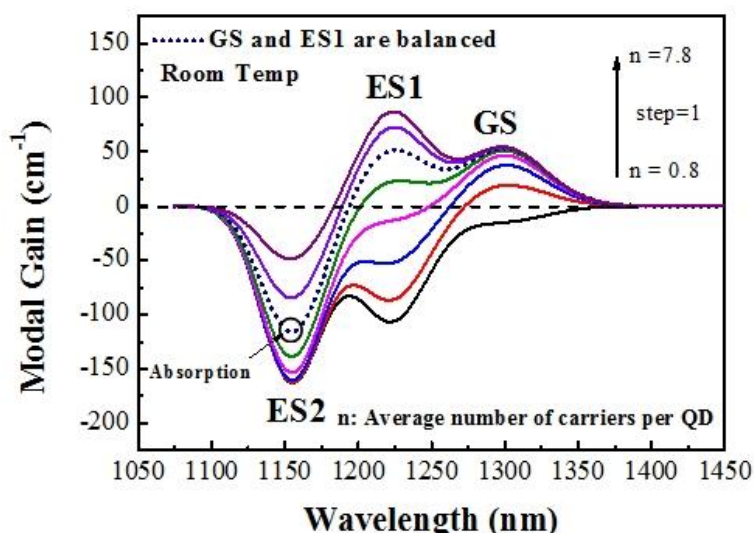


Fig. 3.1 Modeling of room temperature modal gain spectra as a function of average number of carriers per QD for the GS, ES1 and ES2 of 10-layer 1300nm InAs QD. Dashed line represents the situation where the modal gain spectrum due to the GS and ES1 are balanced.

In this chapter, a single QW is introduced into a multi-layer stack of QDs, spectrally positioned to emit at a wavelength equivalent to the second excited state of the QDs. It is proposed that the higher saturated gain of the QW will offset losses associated with the second excited state of the QDs. Two hybrid QW/QD structures are studied optoelectronically through PL, I-V, C-V, PC and EL. I show that the significant difference in the EL spectra is attributed to the different carrier transport/distribution effects due to the placement of the QW rather than due to other possible differences in the device structure. From this optimal structure, the measured spontaneous emission (from both the QW and QDs) results in a full width at half maximum (FWHM) of 250nm being demonstrated. By analysis of the temperature dependent EL, a model of the flow of carriers in the hybrid structures is proposed and described indicating that the hybrid QW/QD structure is highly desirable for broadband application.

3.3 Experiments

I studied three p-i-n structures termed “n-side”, “p-side” (referring to the location of the well relative to the stack of dot layers) and “control”. The structures under study were grown by a V90 solid source molecular beam epitaxy reactor on a (100) Si-doped GaAs substrate by Dr. M. Hugues. Fig. 3.2 shows a schematic of the n-side structure. The epitaxy for the n-side sample starts with a 200 nm thick n-type GaAs buffer ($2 \times 10^{18} \text{ cm}^{-3}$) layer, followed by a 2.3 μm thick n-type ($2 \times 10^{18} \text{ cm}^{-3}$) lower $\text{Al}_{0.3}\text{Ga}_{0.7}\text{As}$ cladding layer, above this is a 25 period superlattice of GaAs (0.5nm)/ $\text{Al}_{0.4}\text{Ga}_{0.6}\text{As}$ (0.5nm). This has proved that it is advantageous to use the superlattice for filtering or blocking threading dislocations. Such a filtering effect is governed by the misfit strain (arise from adjacent layers) which force threading dislocations away from the growth direction [21]. Another function of superlattice is to help confine carriers into the active region [22]. Above the first superlattice is grown an un-doped active region. Above the active region is grown a second 25 period GaAs(0.5nm)/ $\text{Al}_{0.4}\text{Ga}_{0.6}\text{As}$ (0.5nm) superlattice, followed by a 1.8 μm thick p-type ($5 \times 10^{17} \text{ cm}^{-3}$) upper $\text{Al}_{0.3}\text{Ga}_{0.7}\text{As}$ cladding layer, and finally a 300 nm thick highly p-doped ($>1 \times 10^{18} \text{ cm}^{-3}$) GaAs contact layer. For the growth of the active region, firstly 45 nm of undoped GaAs and a 7 nm $\text{In}_{0.34}\text{Ga}_{0.66}\text{As}$ single QW were grown, followed by six $\text{In}_{0.18}\text{Ga}_{0.82}\text{As}/\text{InAs}/\text{In}_{0.18}\text{Ga}_{0.82}\text{As}$ DWELL layers. Each DWELL layer of dots was formed by depositing 2.7 monolayers (ML) of InAs on a 1 nm $\text{In}_{0.18}\text{Ga}_{0.82}\text{As}$ layer, capped with a 6 nm $\text{In}_{0.18}\text{Ga}_{0.82}\text{As}$ layer. The seven layers of the hybrid QW/QD structure were each separated by a 45 nm GaAs barrier layer, of

which the initial 5 nm was grown at 520 °C, the remaining 40 nm of spacer layer was grown at an elevated temperature (600 °C) to form high-growth temperature spacer layers (HGTSLS). The use of such a HGTSLS has been demonstrated to reduce the density of defects and dislocations, improving the optical properties of the stacked layers [23]. To obtain a high quality QW with a sharp interface between the QW and the GaAs barriers, a low growth rate and relatively high growth temperature have been used for the high indium concentration InGaAs QW and GaAs barriers [24]. To achieve high dot density with large-size inhomogeneity, here a relatively low growth temperature was used during the formation of the QDs [13].

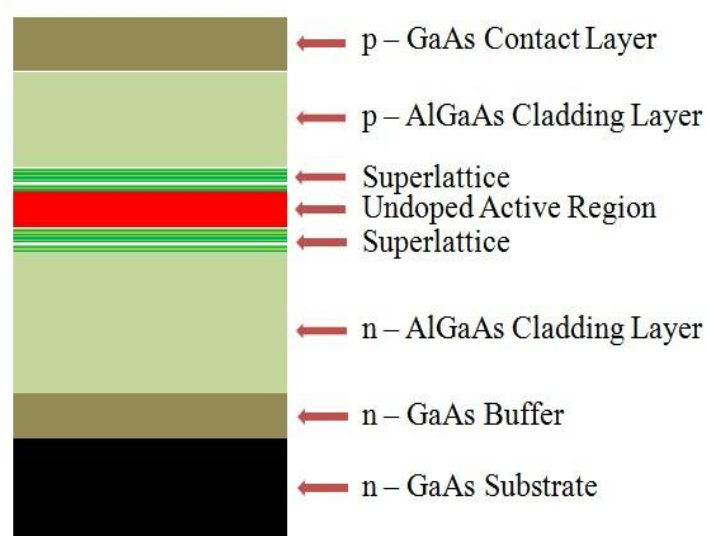


Fig. 3.2 Schematic of epitaxy layer structure.

This structure contrasts with previous QW/QD structures used for tunnel injection of carriers [25] as due to the thick barriers (45nm) there is not expected to be any tunneling between the QW and QDs. For the p-side sample, the structure is nominally identical except for the arrangement of the active region. Each active

region comprises the same components, but the growth sequence between the QW and the stack of QD layers has been reversed. In order to verify the effects of the single QW, a control structure containing only QDs was grown under identical conditions to those described above, but with the QW replaced by a DWELL layer, i.e. it contained 7 QD layers in its active region. Schematics of the active region for n-side, p-side and control are presented in Fig. 3.3. Fig. 3.4(a) shows a transmission electron micrograph (TEM) of the whole active region of the n-side sample, and Fig. 3.4(b) shows the TEM of the whole active region of the p-side sample [26]. It is clear to see that, hybrid structures (both n-side and p-side) consist of 6 DWELL and a single QW. For n-side sample, as seen, in Fig. 3.4(c), a sharp interface between the QW and the GaAs barrier is achieved. Compared to the n-side sample, as seen in Fig. 3.4 (d), the p-side sample shows a comparatively rough interface between the QW and the GaAs barrier layer. We believe that the origin of surface roughness on p-side QW is attributed to the strain field of the underlying QD layers modifying the growth of the p-side InGaAs QW. The role of QD strain modifying the optical properties of the n-side sample is discussed in later chapters.

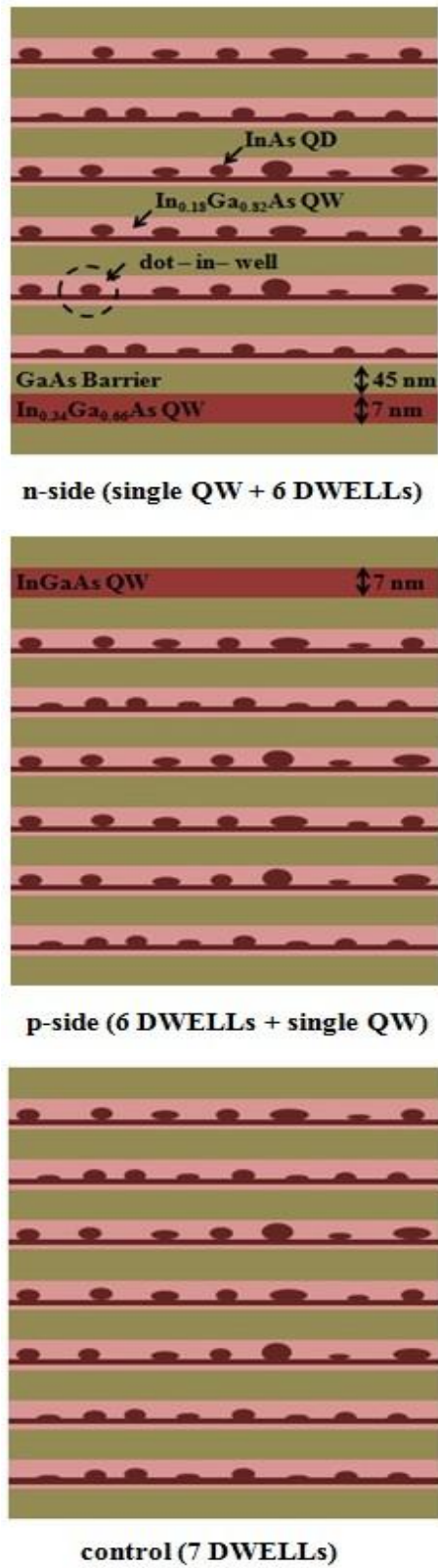


Fig .3.3 schematic of active region for n-side, p-side and control.

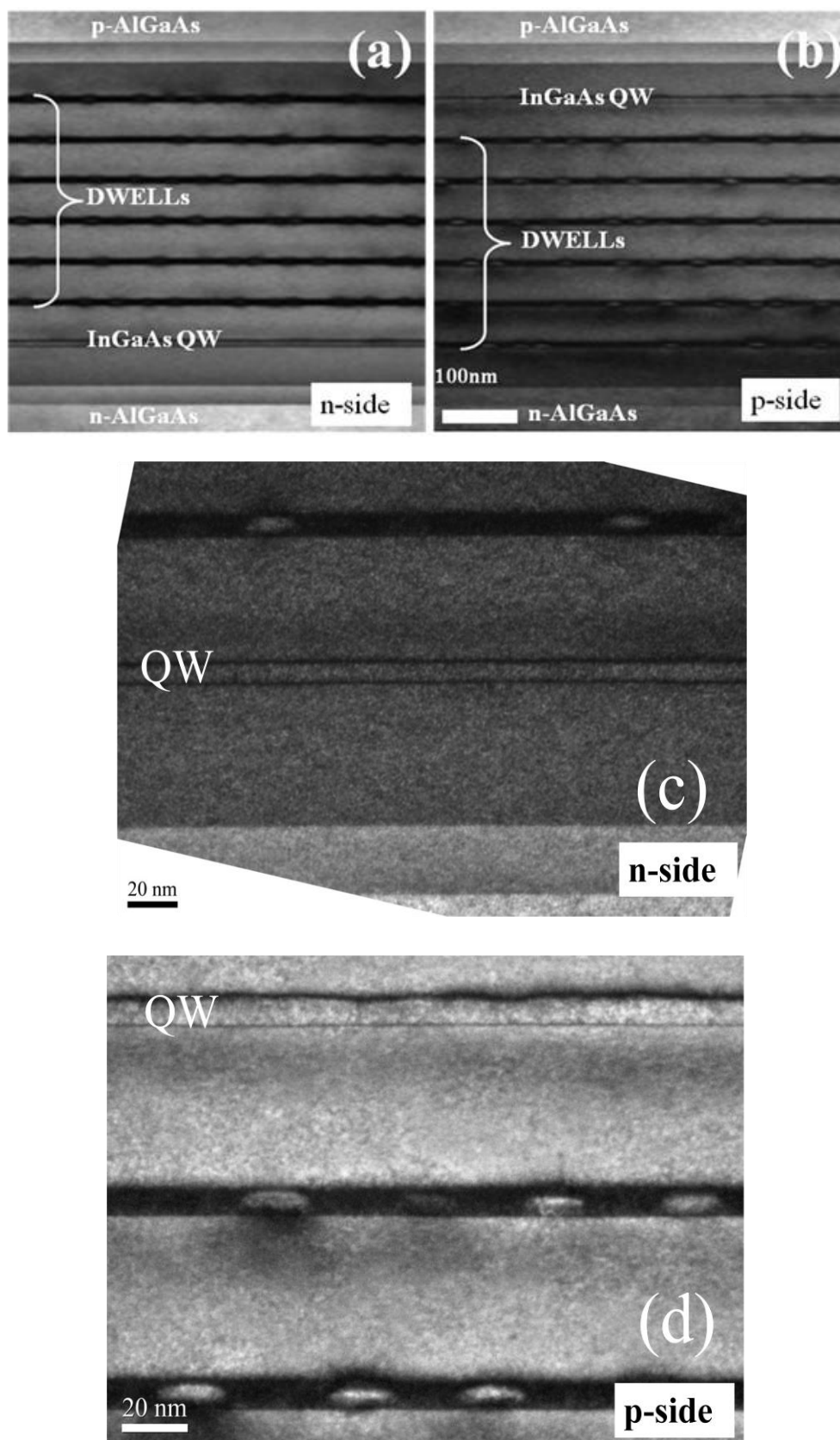


Fig. 3.4 TEM results for n-side and p-side samples [26].

To characterize the material properties such as spontaneous emission, photocurrent, and capacitance-voltage profile, optical access p-i-n mesa diodes were fabricated, which are schematically shown in Fig. 3.5(a). The first step in this process was the patterning of the top surface with an Au/Zn/Au p-type contact, which was then annealed at 360 °C. This was then followed by a wet chemical mesa etch using a 1:1:1 ratio of CH₃COOH, HBr and K₂Cr₂O₇ to a depth of 1.8 μm. The sample was then mechanically thinned for ease of cleaving. Finally a Ti/Au n-type contact was deposited on the back side of the sample and annealed at 340 °C. Devices were cleaved from the sample and mounted onto TO5 headers using gold epoxy at 120 °C, the devices were then wire bonded to enable testing. And the top view of a finished mesa diode is presented in Fig. 3.5(b).

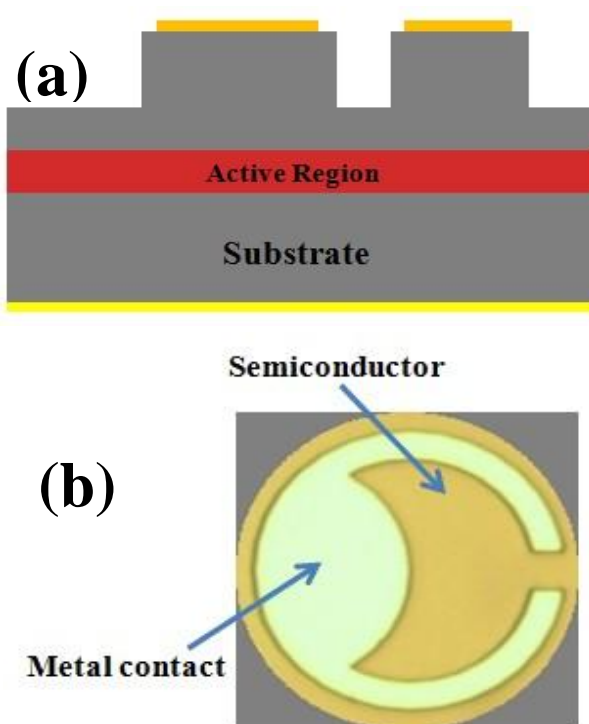


Fig. 3.5 (a) Schematic of optical access p-i-n mesa diode. (b) Top view of a finished device with a diameter of 250 μm.

3.4 Results and Discussion

Fig. 3.6 shows the normalized room temperature photoluminescence (PL) spectra from a single QW test sample (single QW in an undoped GaAs/AlGaAs heterostructures) grown under the same conditions as the wafer described above, and the control sample. PL was obtained using a commercial PL mapper (RPM2000) at room temperature. By mapping across the whole 2 inch wafer, mapping data of PL intensity and PL peak wavelength show that a relatively good uniformity of PL across the whole wafer is achieved from both wafers. The central wavelength and FWHM from the QW test sample are 1126 nm and 25 nm respectively. The PL obtained from the control sample exhibits emission peaks at 1295 nm, 1215 nm, and 1126 nm, attributed to the GS, the ES1 and the ES2 of the QDs. As shown, the emission wavelength of the QW structure is designed to emit at a wavelength equal to the ES2 of the ensemble of QDs, with a QW width of 7nm and [In] of 34% being required to achieve this wavelength.

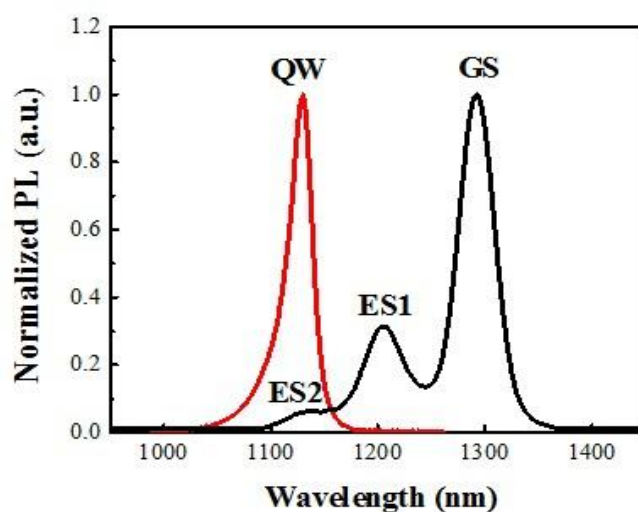


Fig. 3.6 Normalized PL spectrum for QW test sample and control sample at room temperature.

Fig. 3.7 shows the PL spectra at 77K for n-side and p-side wafers under the same excitation conditions. Cap etching is applied to both wafers (with the same etching conditions) to remove the highly doped contact layer and partially etch the AlGaAs layer to obtain a stronger PL signal. For the n-side wafer, the PL spectrum shows a clear luminescence peak at 1205nm, which is attributed to the ground state transition of the InAs QD's. The feature that is partially resolved at ~1140nm arises from the first excited state transition of InAs QD's. An additional strong luminescence peak at 1077 nm is also observed. One possibility is that this emission is due to the second excited state (ES2) of the QDs. However, due to state filling effects, a significant ES2 transition is not expected until ES1 is saturated at an intensity level approximately twice that of the GS [27]. It is also noted that the QW is expected to emit at approximately this wavelength. Due to the apparent lack of saturation of ES1 and the spectral position, I attribute the feature at 1077nm to the QW. Similar spectra are seen for the p-side wafer. It is noteworthy that compared to the n-side wafer, there is a comparative increase in the PL intensity of the QW in the p-side wafer, as the wafer is illuminated from the p-side, the p-side QW can be expected to receive more photo-excited carriers.

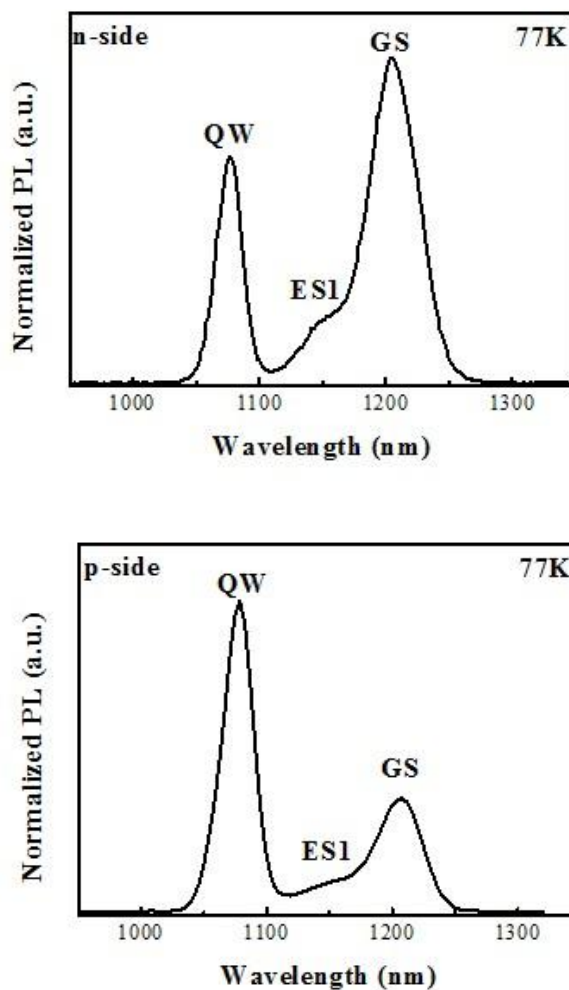


Fig. 3.7 PL results for n-side and p-side samples at 77K under the same excitation condition.

Fig.3.8 shows forward voltage-current (V - I) and capacitance-voltage (C - V) characteristics of the n-side, p-side and control sample at room temperature. All devices have the same diameter of 250 μm . The essentially identical forward I - V indicates that the three devices are electrically identical. Very similar C - V characteristics are also observed for the three samples.

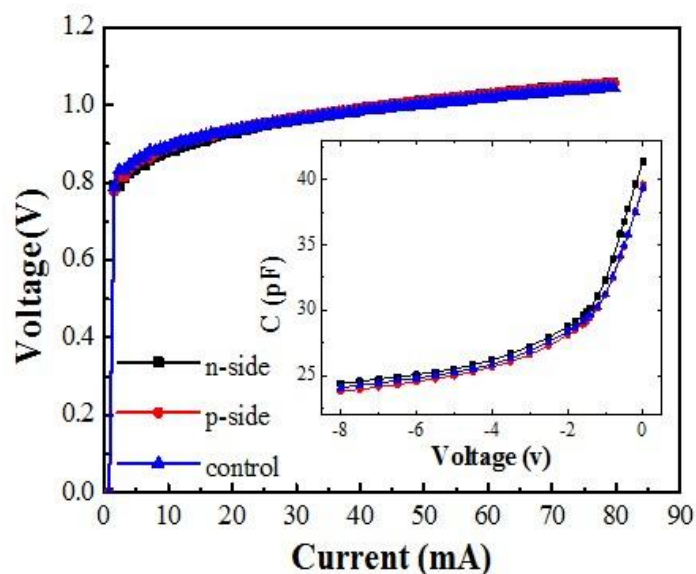


Fig. 3.8 Forward current-voltage and capacitance-voltage characteristics of mesa diodes for n-side, p-side and control samples with the same diameter at room temperature [26].

Fig. 3.9(a) and Fig. 3.9(b) show the photocurrent spectra for the control sample and the n-side sample as a function of applied bias at room temperature. As seen in Fig. 3.9(a), at 0 volt (short-circuit), a series of well-defined peaks arising from the InAs QDs interband absorption (GS, ES1, ES2, etc.), are observed from 0.94 to 1.15 eV. As the applied reverse bias is increased from 0 to 6 V, a linear shift of the QD interband transitions (GS and ES1) to lower energy is clearly observed, suggesting that the dots have a permanent dipole moment at 0V [28]. Similar spectra are seen for the n-side sample, which is present in Fig.3.9 (b). However, a strong PC signal is observed at ~ 1.09 eV. Comparison to data for a control sample, which contains only QDs, suggests that this peak is due to the QW. As the applied reverse bias is increased, a quadratic shift of the energy transitions to lower energy and a concomitant broadening of the PC peak is observed due to the quantum confined Stark effect (QCSE) [29]. The agreement with the predicted transition and QCSE

allows us to attribute this feature to absorption by the lowest energy QW transition. Fig. 3.9(c) shows overlapping PC spectra of an n-side, p-side and control sample at reverse bias of 2 V. It is clear to see that, the n-side and p-side samples display almost the same PC spectrum. The energy of the all transitions (QDs and QW) for n-side sample is slightly shifted with respect to the same transitions on the p-side sample. This is attributed to variations in indium composition in the InGaAs layers making up the QW and DWELL layers in the two samples. In addition, the QW PC peak for the p-side sample is broader, and this is associated with the modulation of the QW observed in TEM.

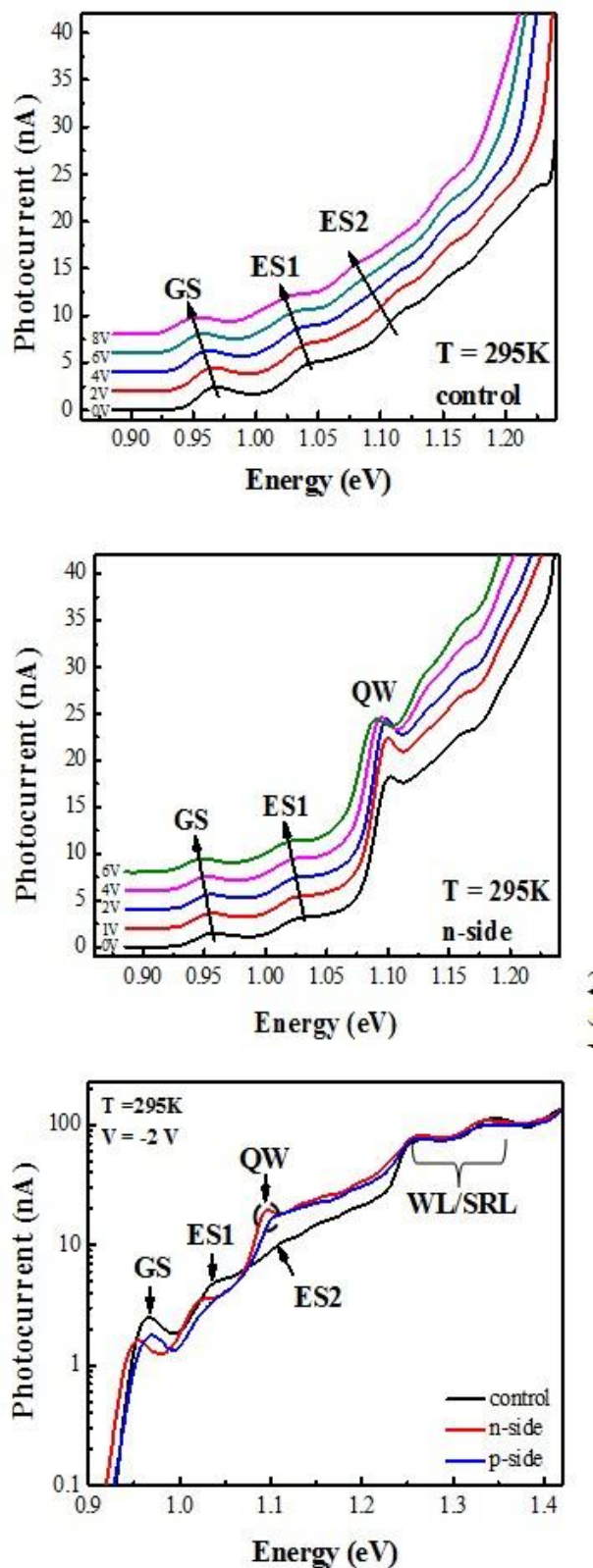
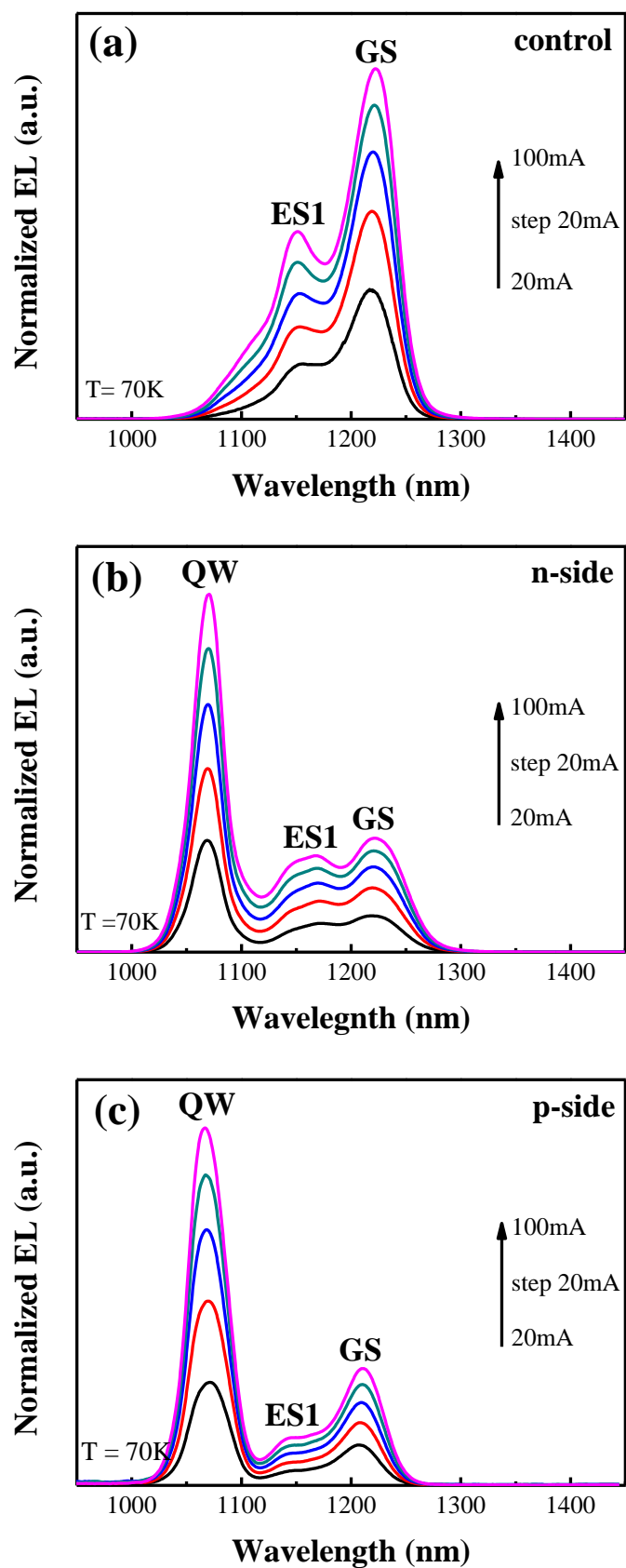


Fig. 3.9 (a) and (b) PC spectra as a function of applied reverse bias for control and n-side samples at room temperature. (c) Overlapping PC spectra of an n-side, p-side and control sample at reverse bias of 2V at room temperature [26].

Fig. 3.10(a)-(c) show normalized spontaneous emission spectra obtained from the mesa diode devices (measured normal to the surface of the mesa diode, and all devices have the same diameter of $250\mu\text{m}$), for various injection currents at 70K. For the control sample (Fig. 3.10(a)), only two features are resolved corresponding to the QD ground state and first excited state transitions. There is no significant second excited state emission observed, as these states are not occupied at these current densities. At this temperature, an additional peak is observed from the hybrid QW/QD samples (Fig. 3.10(b) and Fig. 3.10(c)), and due to its intensity being considerably stronger than the QD-related emission and the spectral position (1068nm), it is attributed to emission from the QW. The form of the emission is noteworthy, as the strong QW emission is at significantly higher energy than the unsaturated QD emission. Compared to the n-side sample, there is an increase in the emission linewidth of the QW in the p-side sample. This is in agreement with line-widths measured in the room temperature PC and is again attributed to the modulation of the QW observed in TEM as discussed previously. However, in the room temperature EL spectra (Fig. 3.10(d)), only the n-side sample shows a strong QW emission at $\sim 1130\text{nm}$. Also, as indicated in Fig. 3.10(e), the n-side sample shows a room temperature spontaneous emission with a 3dB bandwidth of $\sim 250\text{nm}$, suggesting this type of hybrid structure (n-side) has a great potential for achieving broad bandwidth SLDs and SOAs.



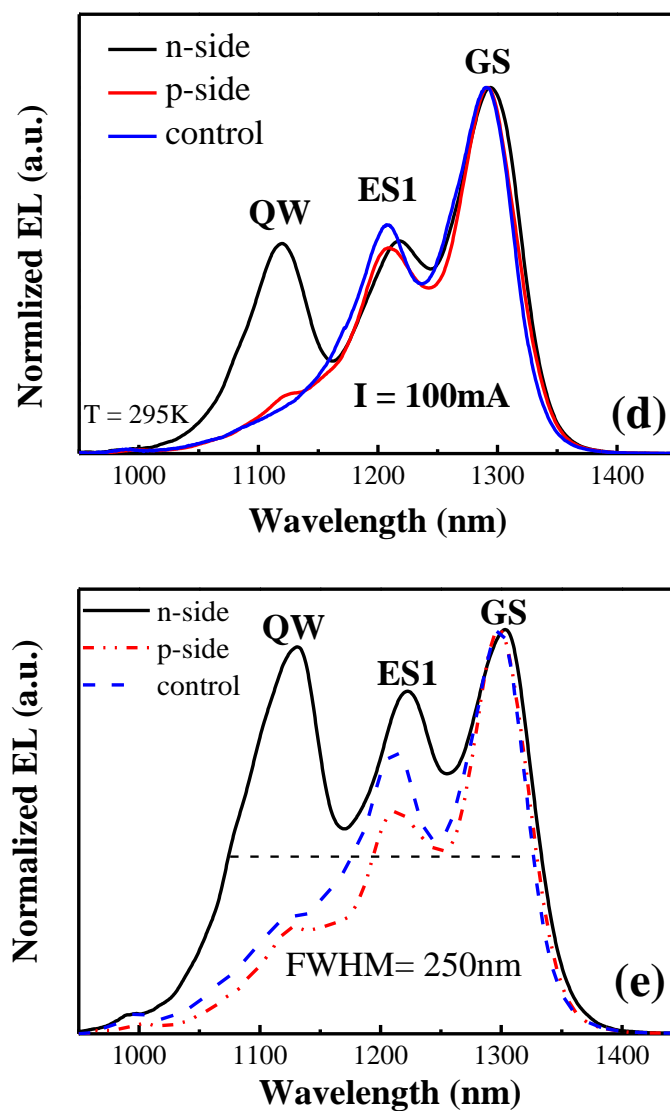


Fig. 3.10 Normalized spontaneous emission spectra for (a) control, (b) n-side, and (c) p-side samples as a function of current at 70K. (d) Normalized spontaneous emission for n-side, p-side and control samples at room temperature at a current of 100mA. (e) Plots of the normalized spontaneous emission for n-side, p-side and control samples at a current density of 760A/cm^2 under CW operation at room temperature [26].

In view of the very similar PL spectra, PC spectra, as well as the essentially identical forward and reverse bias current-voltage response (I-V), and capacitance-voltage (C-V), the difference in the EL spectra are attributed to different carrier transport/distribution effects due to the placement of the QW rather than due to any other differences in the device structure. In order to investigate these transport effects, the spontaneous emission was analyzed as a function of device temperature.

For the n-side sample, as shown in Fig. 3.10(b), at 70K, at 100mA, the emission is dominated by the QW at 1068nm, with the QD ground state at 1218nm and the ES1 observed at ~1166nm. As the temperature is increased to room temperature, the QW emission peak intensity reduces by a factor of ~25 whilst the QD emission reduces by a factor of ~4. Monitoring the emission wavelength as a function of temperature allows the further identification of the QW emission at 1130nm at room temperature. A similar reduction in EL intensities is exhibited by the p-side sample. At low temperature, the emission is dominated by the QW at 1066nm, and as temperature increases, the QW emission shifts to longer wavelength with its peak intensity rapidly reducing in magnitude relative to the n-side QW. At room temperature, the QW is almost “dark”. For calculating the activation energies for QW emission quenching of the n-side and p-side samples, spontaneous emission spectra of the QW as a function of temperature from 175 to 295K are observed as shown in the Fig. 3.11(a) and Fig. 3.11(b) for n-side and p-side samples, respectively. By making an Arrhenius plot of the integrated QW EL intensity (by assuming the QW emission as a

Gaussian function) at a contact drive current of 80mA, an activation energy can be extracted to assist in deducing the origin of the differences in the quenching of the QW emission. This is plotted in Fig. 3.12, and activation energies for the QW emission quenching of the n-side sample and p-side sample are 110 ± 5 meV and 60 ± 5 meV, respectively. I re-measured using a drive current of 20mA, and the observed activation energies for the QW emission quenching of the n-side sample and p-side sample are quite similar, with its values 105 ± 5 and 57 ± 5 meV, respectively.

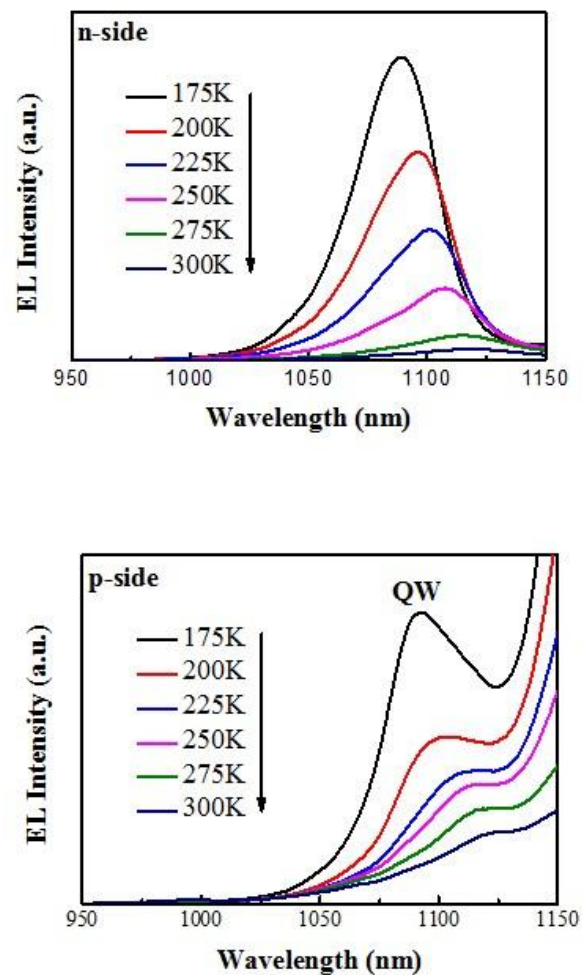


Fig. 3.11 Spontaneous emission of QW from n-side and p-side samples as a function of temperature from 175 to 295K.

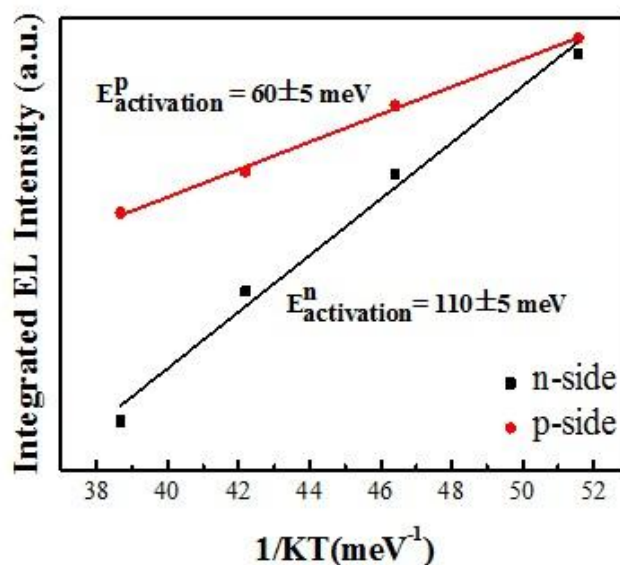


Fig. 3.12 Integrated spontaneous emission intensity (obtain by assuming the emission spectra in Fig. 11 as Gaussian) against $1/KT$. Activation energies for QW emission quenching of the n-side and p-side samples are 110 ± 5 and 60 ± 5 meV, respectively [26].

Fig. 3.13 plots a schematic of the conduction and valence band of the QW, along with the lowest energy electron and hole states. The QW energy levels were calculated using an effective mass approximation method (this modeling is obtained by my colleague Jon Orchard). This model included temperature and strain dependent effects, and standard material parameters [30]. A single 7 nm 0.34 InGaAs QW clad with GaAs barriers on either side was simulated. An electric field of 10 kV/cm was also applied to the simulation structure. As seen, from the modeling results, the calculated activation energy for the QW conduction and valence band are 163meV and 120meV, respectively.

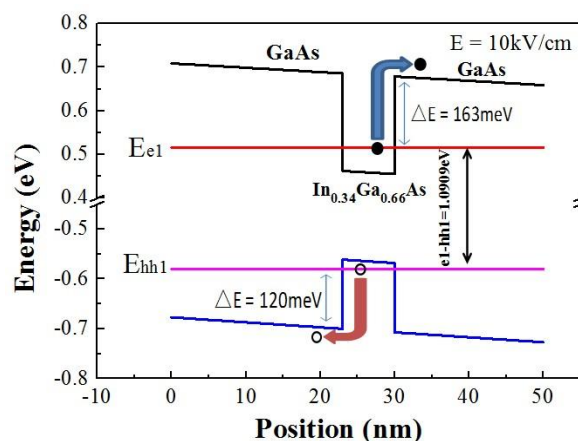


Fig. 3.13 Modeling results of the band structure for a single InGaAs QW. The QW energy levels were calculated using an effective mass approximation method. This model included temperature and strain dependent effects, and standard material parameters. A single 7 nm 34% InGaAs QW was simulated, clad with GaAs barriers on either side. An electric field of 10 kV/cm was also applied to the simulation structure [27].

These observations and calculations suggest the following qualitative argument for the observed change in spontaneous emission, described schematically in Fig.3.14.

At low temperature (Fig. 3.14(a)), for the n-side sample, electrons injected from the n-contact are efficiently captured by the QW and relax into the lowest confined state.

The holes injected from p-contact are inefficiently captured by the dots, due to more restrictive energy and momentum conservation conditions as compared to the QW, resulting in the holes transiting through the structure to the QW. Hence, the QW traps

both electrons and holes and dominates the EL spectra at low temperatures. As the temperature is increased, the electrons are provided with more thermal energy, allowing them to escape the QW resulting in a more spatially uniform electron distribution, enhancing carrier capture in, and emission of the dots at the expense of

the QW as shown in Fig. 3.14(b). Similarly, for a p-side, at low temp, electrons flow freely from the n-side AlGaAs into quantum well Conduction band, and holes flow

freely from p-side AlGaAs into the valence band of quantum resulting in strong QW emission as seen in Fig. 3.15(a). While at high temp, electrons are captured by QDs as they flow towards the quantum well. And holes are thermally liberated from the quantum well and flows into the quantum dots as seen in Fig. 3.15(b). And this account for reduced emission from the quantum well.

It is proposed that the differences in the activation energies of the QW emission for the n-side sample and the p-side sample calculated from the Arrhenius plot reflect the differences in the thermal energy required for electron and hole escape, which drives the process for quenching the QW emission, and enhancing QD related emission. The origin of only n-side shows a strong emission (while p-side QW is silent) at room temperature that is because the n-side QW properties are being driven by electron escape, whilst the p-side QW properties are driven by hole escape. Compared with the p-side QW that is driven by hole escape, for the n-side sample, electrons have greater difficulty to jump out of the GaAs barrier due to a larger thermal barrier leading to stronger QW emission. The discrepancy between the calculated thermalisation energy (from the band structure) and the Arrhenius plot is due to a number of factors. Key parameters such as the rate of capture into the well, carrier lifetime, and phonon related capture into the QDs cannot be expected to be invariant with temperature.

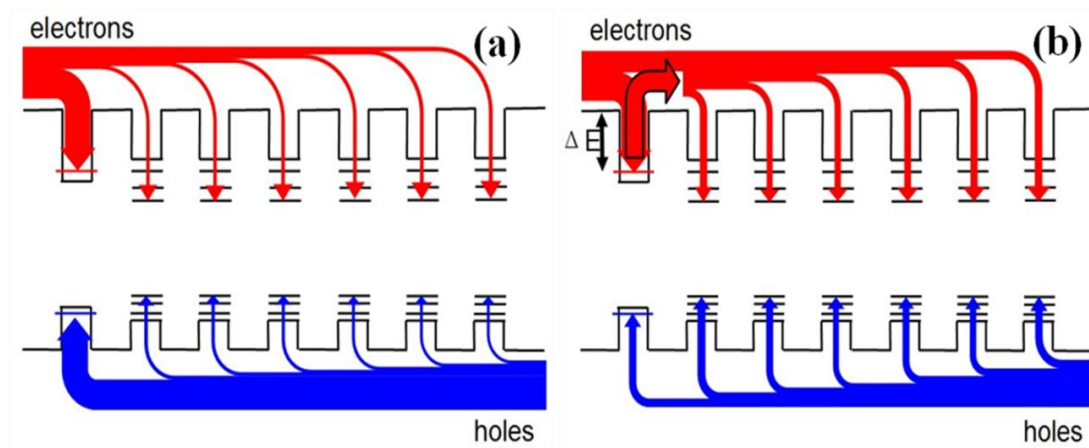


Fig. 3.14 Schematic diagram of the relative potential of the n-side structure and flow of carriers at low and high temperature [23].

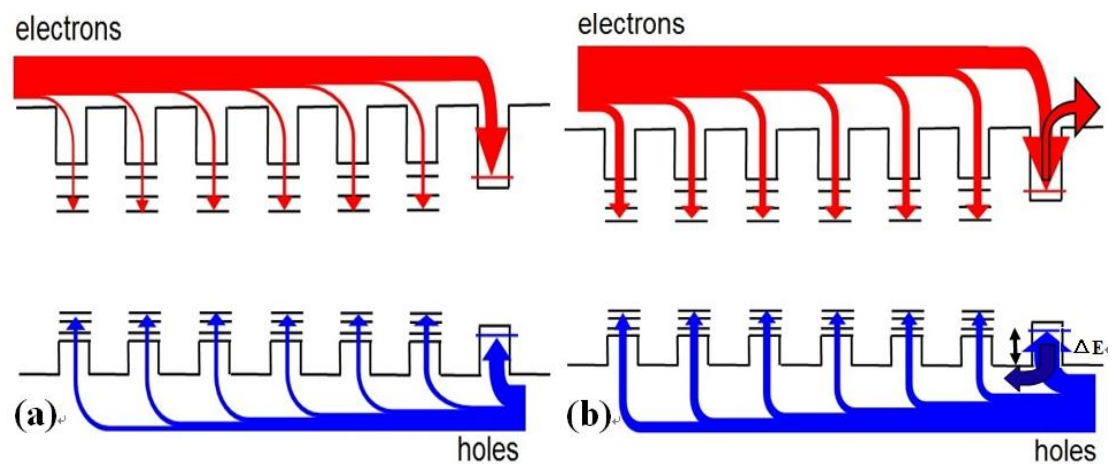


Fig. 3.15 Schematic diagram of the relative potential of the p-side structure and flow of carriers at low and high temperature.

3.5 Conclusion

A hybrid QW/QD structure for application in broadband sources has been introduced. The hybrid structures incorporate a single InGaAs QW and six InAs dot-in-well layers. The QW is spectrally positioned to be coincident with emission from the second excited state of the QDs. I have compared two hybrid samples where the QW

position is changed, and have investigated the opto-electronic properties (such as I - V , C - V and PC), and temperatures dependent spontaneous emission for both hybrid QW/QD samples. From experimental results and calculations, we conclude that, the significant difference in room temperature spontaneous emission is due to the different carrier transport/distribution effects between the n-side and p-side samples. I have shown that spontaneous emission spectra with 250 nm bandwidth have been achieved under CW operation at room temperature from the n-side sample, indicating that this type of hybrid QW/QD structure is highly promising as broadband light sources.

3.6 Future work

As discussed above, the placement of the QW results in very different carrier transport and/distribution effect in hybrid QW/QD structures. Hence it would be interesting to vary the QW position in the active region, for instance, we can try to place the single QW in the middle of the stack of QD layers. Changing the emission energy of the QW and/or, using an InGaAsN QW with different band-offsets would also allow the carrier transport effects to be studied [31].

Further investigation of the carrier dynamics such as the carrier transport in the barriers of the hybrid QW/QD structure and the influence of carrier capture by the QW and QDs on transport would be valuable. Time resolved PL can be utilized to study custom hybrid QW/QD structures, by recording the time resolved emission (rise

time and decay time) from the single QW and QDs (each of them emitting at different wavelength). This may be helpful to investigate the carrier distribution in both space and time [32].

Reference

- [1] T. H. Ko, D. C. Adler, J. G. Fujimoto, D. Mamedov, V. Prokhorov, V. Shidlovski, and S. Yakubovich, "Ultrahigh resolution optical coherence tomography imaging with a broadband superluminescent diode light source," *Opt. Express.*, vol. 12, no. 10, pp. 2112–2119, May 2004.
- [2] W. K. Burns, C. L. Chen, and R. P. Moeller, "Fiber-optic gyroscopes with broad-band sources," *J. Lightw. Technol.*, vol. LT-1, no. 1, pp. 98–105, Mar. 1983.
- [3] S. J. Park, C. H. Lee, K. T. Jeong, H. J. Park, J. G. Ahn, and K. H. Song, "Fiber-to-the-home services based on wavelength-division-multiplexing passive optical network," *J. Lightw. Technol.*, vol. 22, no. 11, pp. 2582–2591, Nov. 2004.
- [4] A. F. Fercher, W. Drexler, C. K. Hitzenberger, and T. Lasser, "Optical coherence tomography-Principles and application," *Rep. Prog. Phys.*, vol. 66, pp. 239-303, 2003.
- [5] Y. Wang, J. S. Nelson, and Z. Chen, "Optimal wavelength for ultrahigh resolution optical coherence tomography," *Opt. Exp.*, vol. 11, pp. 1411–1417, Jun. 2003.
- [6] J. Welzel, E. Lankenau, G. Hüttmann, and R. Birngruber, "OCT in dermatology," in *Optical Coherence Tomography*. Berlin, Germany/New York: Springer-Verlag, 2008, pp. 1103–1122.
- [7] C. F. Lin, and B. L. Lee, "Extremely Broadband AlGaAs/GaAs superluminescent diodes," *Appl. Phys. Lett.*, vol. 32, pp.1598-1600, 1997.
- [8] T. K. Ong, M. Yin, Z. Yu, Y. C. Chan, and Y. L. Lam, "High performance QW intermixing superluminescent diodes," *Meas. Sci. Technol.*, vol. 15, pp. 1591-1595, 2004.
- [9] A. T. Semenov, V. K. Batovrin, I. A. Garmash, V. R. Shidlovsky, M. V. Shramenko, and S. D. Yakubovich, "(GaAl)As SOW superluminescent diodes with extremely low coherence length," *Electron. Lett.*, vol. 31, no.4, pp. 314-315, 1995.
- [10] C. Lin, B. Lee, and P. Lin, "Broad-band superluminescent diodes fabricated on a substrate with asymmetric dual quantum wells," *IEEE Photon. Technol. Lett.*, vol. 8, pp. 1456-1458, Nov.1996.
- [11] T. Ong, M. Yin, Z. Yu, Y. Chan and Y. Lam, "High performance quantum well intermixed superluminescent diodes," *Meas. Sci. Technol.* vol.15, pp. 1591–1595, 2004.
- [12] Z. Z. Sun, D. Ding, Q. Gong, W. Zhou, B. Xu, and Z. G. Wang, "Quantum-dot

- superluminescent diode: A proposal for an ultra-wide output spectrum,” *Opt. Quantum Electron.*, vol. 31, pp. 1235-1246, 1999.
- [13] Z. Y. Zhang, R. A. Hogg, X. Q. Lv, and Z. G. Wang, “Self-assembled quantum-dot superluminescent light-emitting diodes,” *Adv. Opt. Photon.*, vol. 2, pp.201-228, 2010.
- [14] L. H. Li, M. Rossetti, A. Fiore, L. Occhi, and C. Velez, “Wide emission spectrum from superluminescent diodes with chirped QD multilayers,” *Electron. Lett.*, vol. 41, no. 1, pp. 41–43, Jan. 2005.
- [15] X. Q. Lv, N. Liu, P. Jin, and Z. G. Wang, “Broadband emitting superluminescent diodes with InAs QD in AlGaAs Matrix,” *IEEE Photon. Technol. Lett.*, vol. 20, no.20, pp. 1742-1744, Oct. 2008.
- [16] Z. Y. Zhang, R. A. Hogg, B. Xu, P. Jin, and Z. G. Wang, “Realization of extremely broadband quantum-dot superluminescent light-emitting diodes by rapid thermal-annealing process,” *Opt. Lett.*, vol. 33, no. 11. pp. 1210-1212, Jun. 2008.
- [17] Y. Xin, A. Martinez, T. A. Nilsen, A. Moscho, Y. Li, A. L. Gray, and L. F. Lester, “1.3 μm QD multi-section superluminescent diode with extremely broad bandwidth ($>150\text{ nm}$),” *IEEE Photon. Technol. Lett.*, vol. 19, no. 7, pp. 501–503, Apr. 2007.
- [18] M. Grundmann and D. Bimberg, “Theory of random population for quantum dots,” *Phys. Rev. B*, vol. 55, no. 15, pp. 9740-9745 Apr 1997.
- [19] Ryan Roy Alexander, “GaAs based quantum dot lasers for 1.3 μm optical communications” PhD thesis, Mar, 2009.
- [20] H. Shahid, D. T. D. Childs, B. J. Stevens, and R. A. Hogg, “Negative differential gain due to many body effects in self-assembled quantum dot lasers,” *Appl. Phys. Lett.*, vol. 99, no. 6, pp. 061104-1 – 061104-3, Aug. 2011.
- [21] P. L. Gourley, T. J. Drummond, and B. L. Doyle, “Dislocation filtering in semiconductor superlattice with lattice-matched and lattice-mismatched layer material,” *Appl. Phys. Lett.*, vol. 49, no. 17, pp.1101-1103, 1986.
- [22] R. Dingle, H. L. Störmer, A. C. Gossard, and W. Wiegmann, “Electron mobilities in modulation -doped semiconductor heterojunction superlattices,” *Appl. Phys. Lett.*, vol. 33, pp. 665-667, 1978.
- [23] H. Y. Liu, I. R. Sellers, T. J. Badcock, D. J. Mowbray, M. S. Skolnick, K. M. Groom, M. Gutiérrez, M. Hopkinson, J. S. Ng, J. P. R. David, and R. Beanland, “Improved performance of 1.3 μm multilayer InAs quantum-dot lasers using a high-growth-temperature GaAs spacer layer,” *Appl. Phys. Lett.*, vol. 85, no 5, pp.

704-706, Jun. 2004.

- [24] T. Takeuchi, Y. Chang, A. Tandon, D. Bour, S. Corzine, R. Twist, M. Tan, and H.-C. Luan, "Low threshold 1.2 μm InGaAs quantum well lasers grown under low As/III ratio," *Appl. Phys. Lett.*, vol. **80**, pp.2445-2447, 2002.
- [25] P. Bhattacharya and S. Ghosh, "Tunnel injection In_{0.4}Ga_{0.6}As/GaAs QD lasers with 15 GHz modulation bandwidth at room temperature," *Appl. Phys. Lett.*, vol. **80**, no. 19, pp. 3482-2484, Mar. 2002.
- [26] S. Chen, K. Zhou, Z. Zhang, J. R. Orchard, D. T. D. Childs, M. Hugues, O. Wada, and R. A. Hogg, "Hybrid Quantum Well/Quantum Dot Structure for Broad Spectral Bandwidth Emitters," *IEEE J. Select. Topics Quantum Electron.*, vol.**19**, no. 4, pp.1900209-1900209-9, Jul/Aug. 2013.
- [27] K. Matsuda, K. Ikeda, T. Saiki, H. Saito and K. Nishi, "Carrier-Carrier interaction in single In_{0.5}Ga_{0.5}As QD at room temperature investigated by near-field scanning optical microscope," *Appl. Phys. Lett.*, vol. **83**, no. 11, pp. 2250-2252, Sep. 2003.
- [28] P. W. Fry, I. E. Itskevich, D. J. Mowbray, M. S. Skolnick, J. J. Finley, J. A. Barker, E. P. O'Reilly, L. R. Wilson, I. A. Larkin, P. A. Maksym, M. Hopkinson, M. Al-Khafaji, J. P. R. David, A. G. Gullis, G. Hill, and J. C. Clark, "Inverted electron-hole alignment in InAs-GaAs self-assembled QD," *Phys. Rev. Lett.*, vol. **84**, no. 4, pp. 733-736, Jan. 2000.
- [29] D. A. B. Miller, D. S. Chemla, T. C. Damen, A. C. Gossard, W. Wiegmann, T. H. Wood, and C. A. Burrus, "Band-edge electroabsorption in QW structure: the quantum-confined stark effect," *Phys. Rev. Lett.*, vol. **53**, no. 22, pp. 2173-2176, Nov. 1984.
- [30] <http://www.nextnano.de/nextnano3/index.htm>
- [31] M. Galluppi, L. Geelhaar, and H. Riechert, "Nitrogen and indium dependence of the band offsets in InGaAsN quantum wells," *Appl. Phys. Lett.*, vol. **86**, pp.131925-131925-3, Mar. 2005.
- [32] S. Raymond, S. Fafard, P. J. Poole, A. Wojs, P. Hawrylak, S. Charbonneau, D. Leonard, R. Leon, P. M. Petroff, and J. L. Merz, "State filling and time-resolved photoluminescence of excited states in In_xGa_{1-x}As/GaAs self-assembled quantum dots," *Phys. Rev. B.*, vol. **54**, no.16, pp.11548-11554, 1996.

Chapter 4: Gain and Lasing Characteristics of Hybrid QW/QD Laser

4.1 Introduction

In the previous chapter, it was demonstrated that at room temperature, only the n-side sample has strong emission from the QW, and I have also shown that, due to the joint combination of QW and QDs, an ultra-broad spontaneous emission with a 3 dB bandwidth of 250nm has been achieved.

In this chapter, based on the n-side hybrid QW/QD material, a positive modal gain spanning $\sim 300\text{nm}$, covering the wavelength range of 1100 – 1400nm is measured from a segmented contact device. Simultaneous three-state lasing at room temperature, via the ground state (GS), first excited state (ES1) of the QD and the lowest energy transition of the single QW is achieved for hybrid QW/QD lasers. Lasers of different cavity lengths are studied spectroscopically. By changing the cavity length (mirror loss), different lasing sequences are observed and possible origins of this behavior are discussed. Additionally, it is shown that compared to QD-only device, the threshold current density for achieving simultaneous three-state lasing is significantly reduced.

4.2 Background

Semiconductor lasers with broadband lasing spectrum are highly desirable for certain applications, e.g., for mode locking, sensing, and low-coherence imaging [1, 2]. Also the capability of bias controlled multi-mode lasing in a broad wavelength range, can be used as wavelength switching components, which have great potential for multichannel optical communication, read and write operation, and wavelength-division multiplexing [3-6]. Recently, QD based devices have attracted significant attention due to their discrete, zero-dimensional electronic states [7], by changing the cavity loss, lasing can be achieved at any of the QD discrete energy states. With this in mind, simultaneous two-state lasing at room temperature has been achieved in InAs QD lasers [8] via the GS and ES1 transitions due to incomplete gain clamping and Pauli-blocking of the carrier relaxation to the GS. Also researchers have observed three-state lasing phenomena from a QD device at low temperature. It has previously been reported that, by utilizing a high current density in a modulation p-doped InAs/InGaAs/GaAs QD layer structure, simultaneous three-state lasing, from 1151nm to 1309nm, has been achieved at room temperature [9]. However, due to increasing degeneracy of the QD excited states, the threshold current density for simultaneous three-state lasing was as high as $\sim 23\text{kA/cm}^2$.

In this chapter, I describe results obtained from segmented contact narrow ridge laser device fabricated from the n-side hybrid QW/QD active material. A positive modal gain spanning $\sim 300\text{nm}$ is obtained from the segmented contact device. I also

investigate the bias-controlled room temperature operation of simultaneous three-state lasing over 160nm. By changing the cavity length of the lasers, different lasing sequences are observed and discussed. Significantly, the threshold current density for achieving simultaneous three-state lasing has been reduced from our previous results using a QD-only gain element, from 23000 to 1025A/cm² [9].

4.3 Experiments

The structure under study in this chapter is the n-side sample. This laser structure consisting of six-stacked InAs QD layers and a single InGaAs QW embedded in AlGaAs waveguide was grown on a (100) Si-doped GaAs substrate by a V90 MBE reactor. The detailed material epitaxial growth of this structure was described in chapter 3.

To allow the lasing characteristics, as well as the gain and absorption spectra to be measured, the wafers were processed into segmented contact devices following a standard ridge-waveguide laser process, which is schematically shown in the Fig. 4.1(a), the sample was etched to form a 3 μm wide ridge waveguide by inductively coupled plasma (ICP) etching via a double trench. The ridges were etched down to 200nm above the active ridge for optical field confinement. Highly selective wet etch (H₂O₂: Citric Acid 5:1 by volume) was used to isolate the adjacent contacts by removing the p⁺ GaAs contact layer providing a resistance of ~800Ω between adjacent contacts. After evaporation of Au-Zn-Au top contacts, electroplated

bond-pads were then applied. The sample was then mechanically thinned. Finally an InGe/Au n-type contact was deposited on the back side of the sample. The device has cleaved facets on both ends. Fig. 4.1(b) presents a schematic view of the final multi-section device, which is composed of 12 segmented-contact sections, with each contact section being $500\ \mu\text{m}$ in length, giving a total cavity length of 6mm.

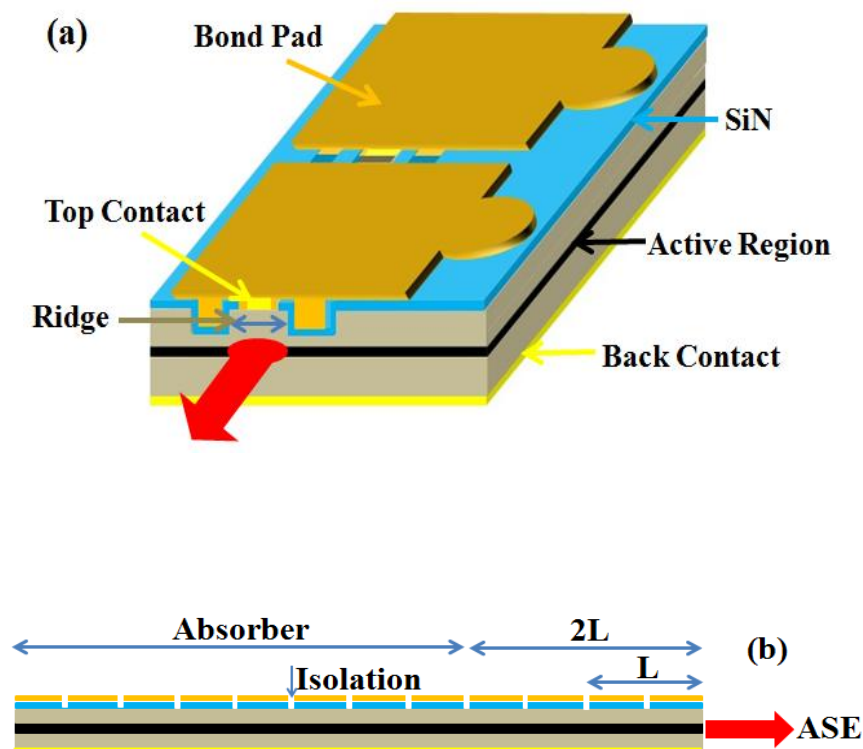


Fig. 4.1 (a) schematic of a segmented contact device (here I only showed two sections of the segment contact device). (b) Side view of the final segmented contact device.

The segmented contacted method was employed to obtain the optical gain and the internal loss with the use of a multi-section device, as illustrated in Fig. 4.1. This method, which analyses amplified spontaneous emission measured as a function of

the pumped stripe length, is described by several groups [10, 11, 12]. For the 1mm/section testing, the first four sections of the multi-section device were configured to form two 1-mm sections. The last eight sections were utilized as an absorber to suppress the round-trip amplification of light for a single-pass measurement. To obtain the gain, first of all, we measure the ASE intensity I_{L1} when only the first two sections of length L (see Fig. 4.1) are pumped with a current density of J , we then measure the ASE I_{L2} while the first four sections of length $2L$ are pumped with the same current density of J . The single-pass ASE intensity is captured by a lensed optical fiber and recorded using an optical spectrum analyzer. In this case, the net modal gain G was obtained by the following equation:

$$G = \frac{1}{L} \left[\ln \left(\frac{I_{2L}}{I_L} - 1 \right) \right] \quad 4.1$$

It is noted that, this equation can allow the gain spectra to be simply measured in absolute units directly from the recorded ASE intensity.

This technique also allows the absorption spectrum to be measured. The ASE intensity is measured in two different cases. The ASE intensity I_1 is measured when the first two sections of length L are biased with a current density of J , the ASE intensity I_2 is measured while the first two sections of length of L are biased at 0 voltage and the second two sections of length of L are biased with a current density of J . As long as the spontaneous emission from both section are equal, the optical loss suffered in the first two sections of length L is given by:

$$\alpha = \frac{1}{L} \ln \left(\frac{I_1}{I_2} \right) \quad 4.2$$

In a similar way to the gain spectrum measurement, the absorption spectrum is also obtained in real units.

4.4 Results and Discussion

Fig. 4.2 is an example of measured ASE spectra at room temperature on an n-side hybrid QW/QD laser structure, while pumping the first two sections of length L (1mm), then pumping the first four sections of length $2L$ (2mm), for a current density of $750\text{A}/\text{cm}^2$.

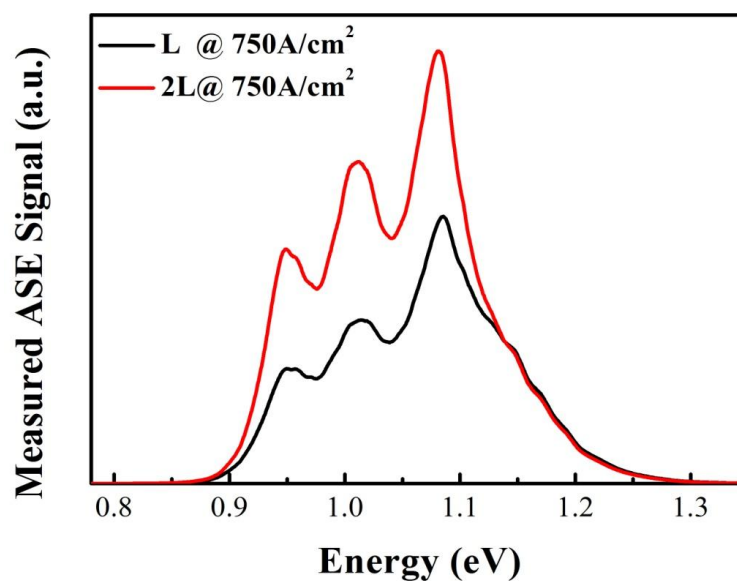


Fig. 4.2 An example of measured ASE spectra for length L and $2L$, at the same current density.

The net modal gain spectrum as well as the absorption spectrum obtained by analysis of the ASE spectra in Fig. 4.2 is presented in Fig. 4.3. In the low photon energy/long wavelength limit below the band edge of the material, the absorption tends to be a

constant value with photon energy/wavelength. This allows the internal loss of $10 \pm 0.5 \text{cm}^{-1}$ to be determined. As we expected, the same value of $10 \pm 0.5 \text{cm}^{-1}$ are observed at low photon energy for both the net modal gain spectrum and the absorption spectrum, leading further confidence in identifying this as the internal loss. This value is somewhat higher than expected and is attributed to imperfect device fabrication. With this value, the net modal gain can be simply converted to the modal gain. Additionally, the transparency point ($h\nu = \Delta E_F$) can be easily determined as the point where the modal gain is zero [11], where the light could propagate in the cavity with no change of light intensity. It is also noticed that the magnitude of the maximum gain for QD GS is significantly less than the measured absorption by a factor of ~ 2 , which is consistent with previous work on InAs QD [13]. While the integrated area (corresponding to the best-fit assuming the spectrum as a Gaussian function) for net gain/absorption spectrum is similar. Additionally, the gain spectrum is observed to be shifted to lower energy relative to the absorption spectrum, the increased linewidth of gain and the shift to lower energy is attributed to free carrier effects within the QDs [14]. As the injection current is increased, more carriers will be filled into the dot, leading to the re-normalization of band offset due to stronger Coulomb attraction arise from increased numbers of electron-hole pairs, which accounts for the shift of gain spectrum to lower energy. While, compared to the absorption spectrum, the increased linewidth of gain spectrum is attributed to the increased homogenous broadening of the optical gain.

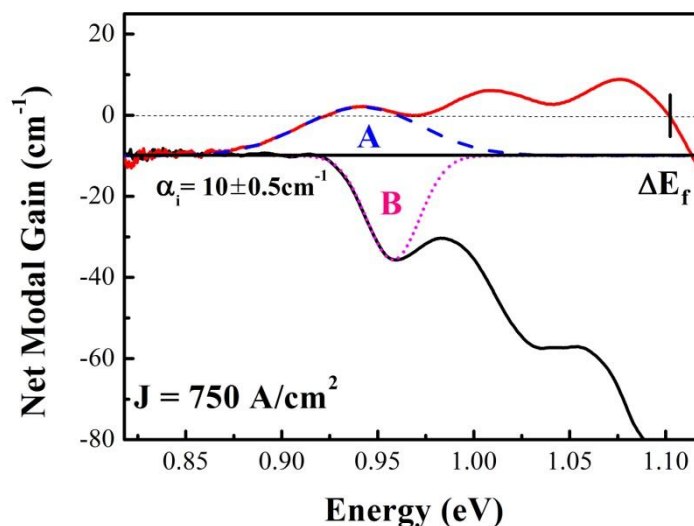


Fig. 4.3 The measured net modal gain spectrum as well as the absorption spectrum at 750A/cm² from multi-section device. A (blue dash line) and B (pink shot dash line) represent the integrated area (corresponding to the best-fit assuming the spectrum as a Gaussian function) for the ground state net gain and absorption, respectively.

Fig. 4.4(a) plots the modal gain spectra of the hybrid QW/QD sample as a function of current density at room temperature. As shown in Fig. 4.4(a), the gain spectrum is dominated at low current densities by the QD GS emission at 1320 nm. As current density is increased, the GS gain saturates and the modal gain for ES1 at 1230 nm increases. At the highest current densities, a peak in gain emerges at 1150 nm, which dominates the spectrum at the highest current density of 917 Acm⁻². A ~20 nm redshift in the QD ground-state and excited-state emission, as compared to the mesa-diode is noted, and is attributed to spatial variation of the epitaxial material. The 1150 nm gain peak is therefore attributed to the QW. Modal gain spanning ~1100 nm to ~1400 nm is observed in this structure over these carrier densities. The net modal gain spans 240nm, from 1110 nm to 1340 nm. There is a significant improvement in the net-modal gain (modal gain) bandwidth of 35 % (50%) with respect to previous work in ref. [15]. Improved device fabrication, resulting in a

reduction of the internal loss, can be expected to increase the span of positive net modal gain. Increased current densities will also increase the modal gain and net modal gain coverage to lower wavelengths.

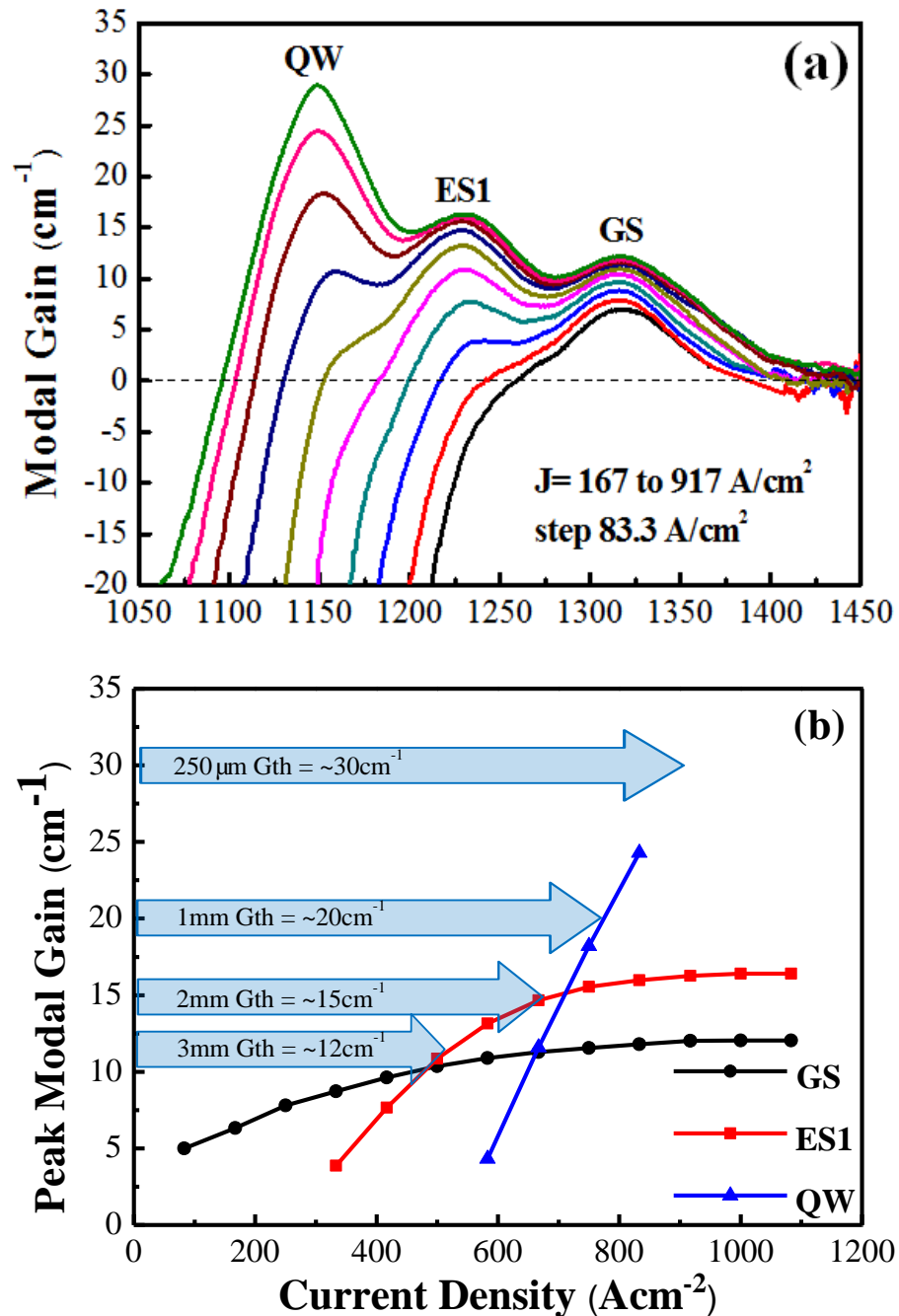


Fig. 4.4 (a) Modal gain spectra as a function of current density. (b) Peak modal gain spectrum against current density for QD GS, the QD ES1, and the lowest energy transition of QW. The arrows indicate, for each cavity lengths, the required threshold modal gain for GS to achieve lasing.

Fig. 4.4(b) shows the measured peak modal gain as a function of current density for the GS, ES1 and the QW from the n-side sample. At low injection current density, modal gain due to the QD GS dominates and gradually increases with increasing current density. Due to the limited density of states in the QD material, the modal gain for the QD GS is fully saturated with a saturated modal gain of $12 \pm 1 \text{ cm}^{-1}$. This value for saturated modal gain is in line with previous work on similar structures [16]. Due to the increased degeneracy of the excited state, it is expected that the saturated modal gain of the ES1 would be twice that of the GS ($\sim 24 \text{ cm}^{-1}$). However, the modal gain of ES1 appears to saturate at a peak gain value of 17 cm^{-1} . Whilst the saturation of QD gain at a value below that of full inversion has been shown [17], recent work on 1300nm QD laser has shown a saturated gain of the ES1, which is twice of the GS [14]. It therefore appears that ES1 does not fully saturate in this structure, yet pins at an average QD occupancy around 6 e-h pairs per QD [18]. For such values of QD carrier occupancy, we do not expect gain from ES2, lending further confidence in our assignment of the origin of the gain at 1150nm being due to the QW. This assignment is also based on studies of the spontaneous emission as a function of temperature and current density [see chapter 3]. The arrows indicate, for each cavity lengths, the required threshold modal gain for GS to achieve lasing. By assuming the internal loss is fixed at 10 cm^{-1} for each cavity length, it is therefore the threshold modal gain of 30 cm^{-1} , 20 cm^{-1} , 15 cm^{-1} and 12 cm^{-1} are required to achieve GS lasing for $250 \mu\text{m}$, 1 mm , 2 mm and 3 mm . This threshold modal gain- cavity characteristic will be discussed in detail later in this chapter. A key conclusion reached here is that

the modal gain for the QDs ES1 can be clamped at low current density whilst the QW still increases in modal gain with further increasing current density. This is important for achieving a broad flat emission spectrum for a superluminescent diode (discussed in detail later in chapter 5). In addition, this may provide evidence for dissimilar carrier lifetimes in the QW and QDs, and/or a lack of a continuous quasi-Fermi level between the QW and QDs. The occurrence of a dissimilar carrier lifetime between the QDs and QW is needed to explain the apparent clamping of the gain in the QDs, yet monotonous increase in gain in the QW. In such a case the QDs and QW are not efficiently coupled in terms of carrier transfer between the energetically and spatially different states (in such a case the carrier lifetime would be dominated by the fastest recombination rate). Further experimental work is needed in order to further understand the carrier transport and lifetime properties of these hybrid structures.

In order to further confirm the values obtained for the modal gain and explore the bias-controlled multi-state lasing in the hybrid QW/QD laser, lasers of different cavity lengths were studied spectroscopically. All the device characterization was performed at room temperature, under pulsed operation with 5 μ s pulse width and 1% duty cycle to minimize self-heating of the device.

Fig. 4.5 shows the electroluminescence (EL) spectra as a function of drive current density for a 250- μ m-long and 3- μ m-wide segmented contact laser before the onset of

lasing at room temperature. As seen, at relatively low pumping current density of 100A/cm^2 , only one emission peak is observed at $\sim 1310\text{nm}$, which is due to the GS transition of the InAs QDs. As current density is increased, the GS emission saturates, and two emission peaks due to the first excited state of the QD at 1128nm and the single QW at 1150nm increases, at higher current densities, the ES1 emission also becomes saturated while the QW still increases in intensity with further increasing current density.

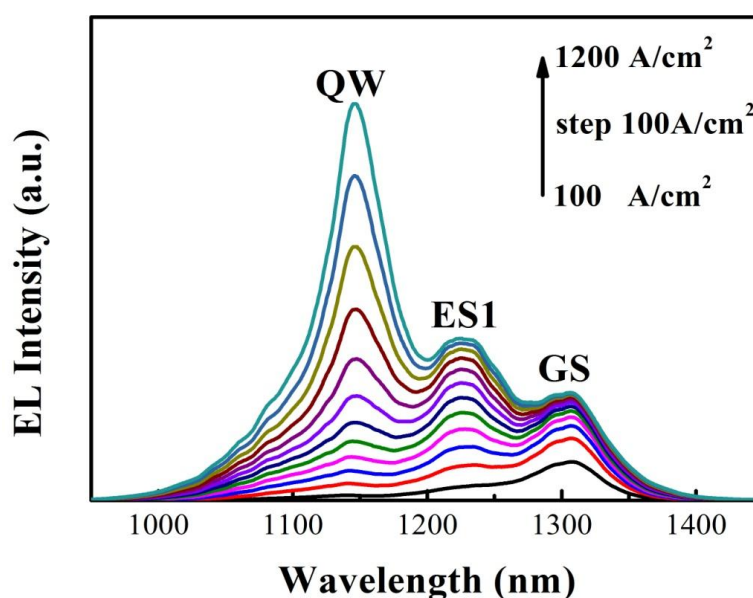


Fig. 4.5 EL spectra for 250- μm -long segmented contact 3 μm narrow ridge laser as a function of drive current density before the onset of lasing at room temperature.

Fig. 4.6 shows the light-current characteristic of hybrid QW/QD laser for a cavity length of 500 μm at room temperature. The inset of Fig. 4.6 shows the emission spectra as a function of current density. Referring to Fig. 4.4(b), at this cavity length, the mirror loss is too large to allow QD lasing, so that lasing is observed only from the single InGaAs QW, which is confirmed by the lasing wavelength of 1150nm, with a

threshold current density of $\sim 925 \text{ A/cm}^2$. The emission peaks at $\sim 1310 \text{ nm}$ and $\sim 1128 \text{ nm}$ correspond to the GS and the ES1 of the InAs QD ensemble, as measured by the spontaneous emission of mesa diodes [see chapter 3] and the EL spectrum from the short cavity device [see Fig. 4.5].

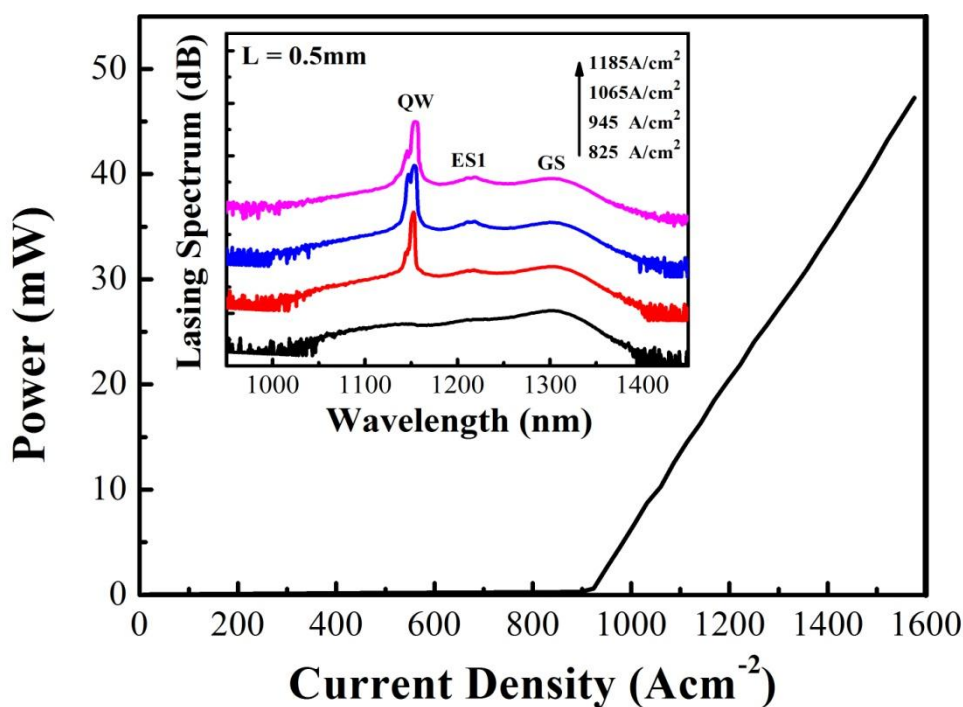


Fig. 4.6 L-I curve of hybrid QW/QD laser for a cavity length of 500- μm -long laser at room temperature. The inset shows the lasing spectra as a function of current density.

The output power-current characteristic of the hybrid QW/QD laser for a cavity length of 3-mm at room temperature is shown in Fig. 4.7(a). The inset shows the EL emission spectra at various injection current densities. As the cavity length is increased, the threshold modal gain for achieving device lasing is reduced to $\sim 12 \text{ cm}^{-1}$ as shown in Fig. 4.4(b). Lasing occurs first on the GS once its threshold has been reached. As the current injection is increased, ES1 lasing at 1128nm is also

observed, suggesting that as expected for QDs, efficient gain clamping does not occur for the ES1 once the GS has reached its threshold [8]. Further increasing the current density, while maintaining lasing from the GS and the ES1 of the QD, QW lasing at 1150nm is also observed. There are three 'kinks' clearly observed in the power-current curve, corresponding to the onset of lasing of GS, ES1 and QW. The positions of the three lasing peaks are in good agreement with the absorption peaks obtained in the PC spectrum [see Fig. 9 in chapter 3], as well as the gain peaks measured from the modal gain spectrum [see Fig. 4.4(a)].

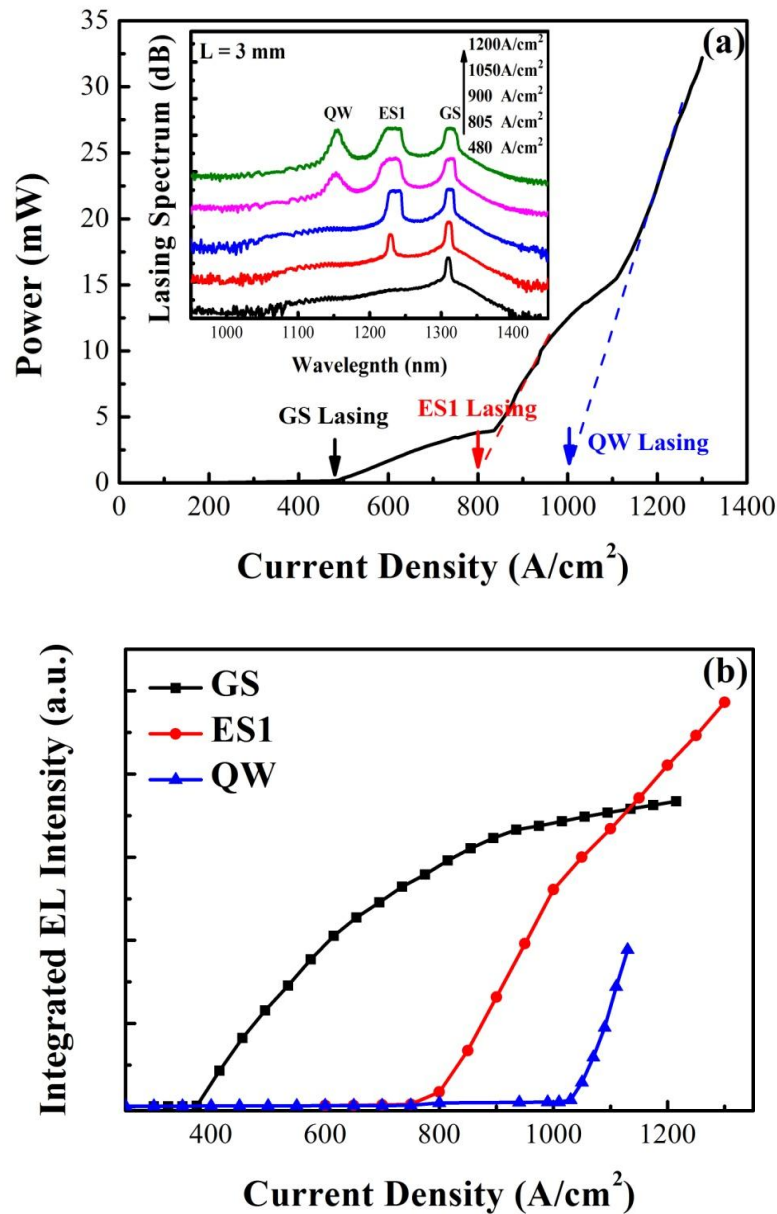


Fig. 4.7 (a) L-I curve of hybrid QW/QD laser for a cavity length of 3-mm-long laser at room temperature. The inset shows the lasing spectra at various injection current densities. (b) The integrated GS lasing peak, the integrated ES1 lasing peak and the integrated QW lasing peak verses the current density at room temperature.

In order to gather further insight into the lasing mechanism, the spectrally resolved light-current characteristic was studied. Fig. 4.7(b) shows the integrated GS lasing peak, the integrated ES1 lasing peak and the integrated QW lasing peak verses the current density at room temperature. As seen, the GS starts lase at a current density

of $\sim 390 \text{ A/cm}^2$, and ES1 lasing occurs at a current density of $\sim 805 \text{ A/cm}^2$. Increasing the current density to 950 A/cm^2 , the integrated intensity of the GS lasing peak saturates, the measured full width at half maximum (FWHM) of both the GS and the ES1 increase over this interval, which is attributed to non-ideal gain clamping in the inhomogeneously broadened optical gain and the contribution of QDs within the homogeneous linewidth of the lasing mode [19]. Further increasing the current density over 1025 A/cm^2 , lasing from the QW transition occurs, coincident with the onset of the QW lasing, a reduced slope efficiency of ES1 is observed. Also the FWHM of both the GS and the ES1 maintains an almost constant value after the onset of QW lasing. As expected, the span of the lasing spectrum is similar to our previous QD-only device [9]. The hybrid QW/QD laser can, therefore, achieve a room temperature bias-controlled multi-state lasing, however, by using this kind of hybrid QW/QD structure, the threshold current density for achieving simultaneous three-state lasing has been reduced from ~ 23000 [9] to $\sim 1025 \text{ A/cm}^2$. This kind of three-state lasing is highly desirable for multichannel optical communication, read and write operation and WDM systems.

Fig. 4.8(a) shows the light-current characteristics of the hybrid QW/QD laser with a cavity length of 2mm. 4.8(b) shows the emission spectra as a function of current density at room temperature. Again, referring to Fig. 4.4(b), at this cavity length, the threshold modal gain is expected to be $\sim 15 \pm 1 \text{ cm}^{-1}$, the saturated modal gain for the QD GS is $\sim 12 \text{ cm}^{-1}$, and the gain of the GS transition is too small to match the total

loss. GS lasing is inhibited and the device starts to lase at $\sim 1228\text{nm}$ from the QD ES1 transition, with a threshold current density of 700 A/cm^2 . This is in agreement with the modal gain data of Fig. 4.4(b), with lasing occurring at a point close to the intersection of the QW and ES1 curves. As the injection current density increases, additional lasing emission associated to the QW clearly appears around $\sim 1150\text{ nm}$. Further increase of the drive current density over $\sim 1125\text{ A/cm}^2$, a third lasing peak, attributed to the QD ground state, is observed at $\sim 1310\text{ nm}$. This is a surprising result as it is expected from Fig. 4.4(b) that the GS has insufficient gain to lase.

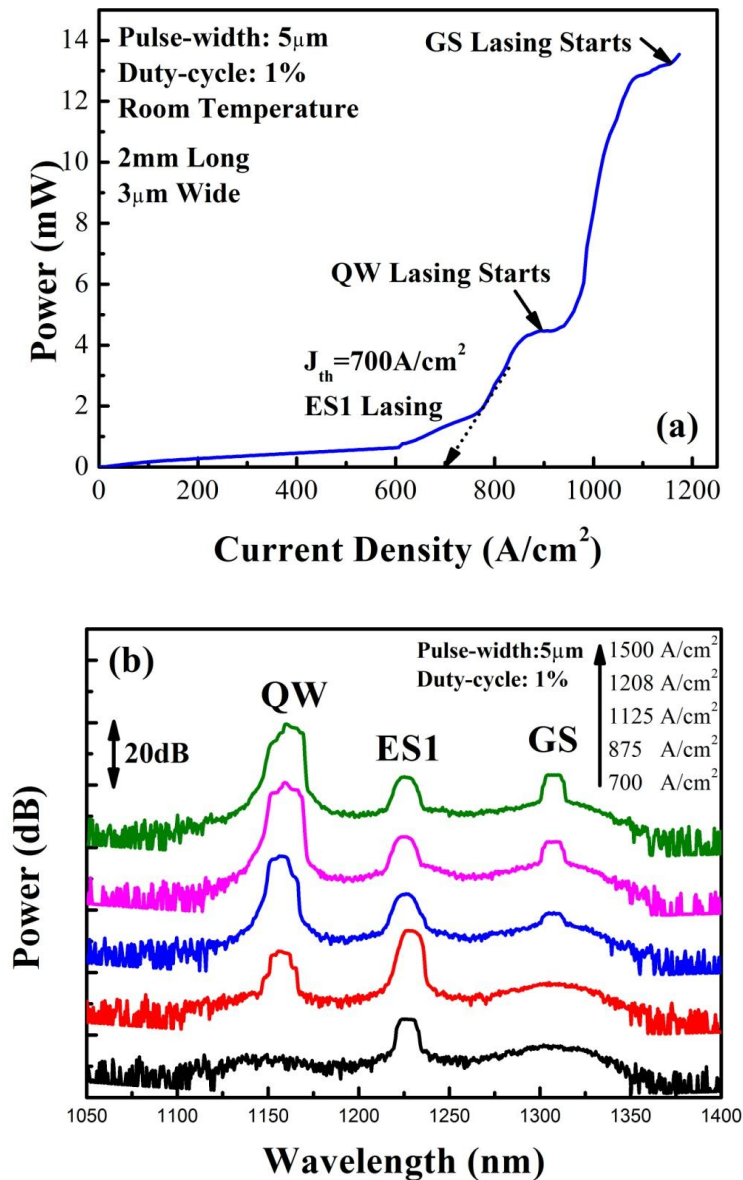


Fig. 4.8 (a) The L-I characteristics of hybrid QW/QD laser for a cavity length of 2mm long laser. (b) The emission spectra as a function of current density at room temperature [19].

Fig. 4.9 shows the spectrally resolved integrated lasing peak intensities of the GS, ES1, QW, as a function of the current density for 2mm long device. For injection current density equal to $\sim 700 A/cm^2$, lasing occurs via the ES1 transition. From 700 to $875 A/cm^2$, ES1 lasing emission dominates and gradually increases with increasing injection current density. The measured full width at half maximum (FWHM) of ES1 increases over this interval, as discussed previously, which is also attributed to

non-ideal gain clamping in the inhomogeneously broadened optical gain and the contribution of QDs within the homogeneous linewidth of the lasing mode [20]. When the drive current density reaches 875 A/cm^2 , the QW state begins to lase and rapidly dominates. Coincident with the onset of QW lasing, the integrated EL intensity of ES1 saturates before a rapid reduction as the current density increases. For high current density injection ($>1000 \text{ A/cm}^2$), the ES1 integrated EL intensity tends to a constant value. At the same time, the FWHM of ES1 maintains a constant value after the QW lasing onset, which, as expected, suggests that carriers are more effectively captured by the QW. At high drive current density ($> 1125 \text{ A/cm}^2$), the integrated EL intensity of the QW saturates and gradually decreases at very high current density. In the mean time, QD GS lasing is observed and its intensity gradually increases with increasing current density. Again, at this cavity length, bias-controlled simultaneous three-state lasing can also be achieved. However, this kind of lasing sequence is rather different from observations reported previously [8, 9, 20] where lasing occurred in the sequence of GS, ES1, ES2.

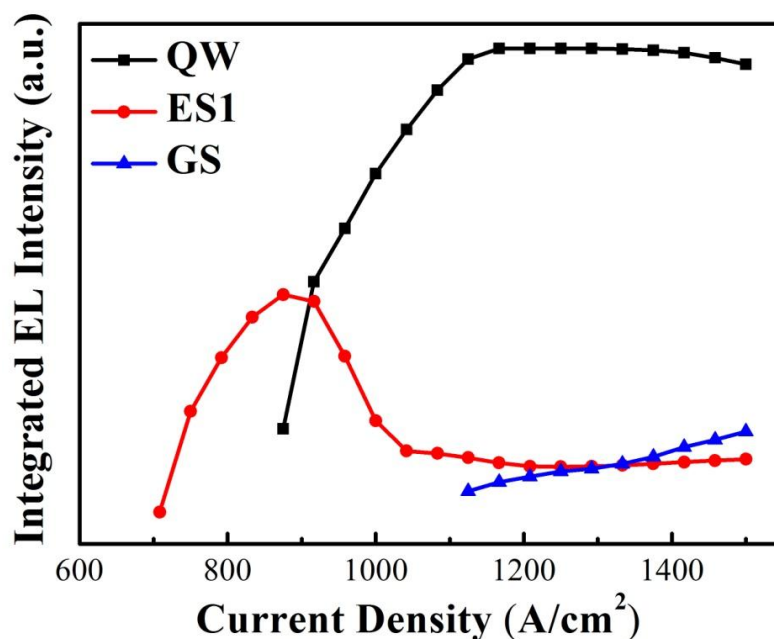


Fig. 4.9 The spectrally resolved integrated lasing peak intensities of the GS, ES1, and QW as a function of the current density for a cavity length of 2mm long hybrid laser [19].

Fig. 4.10(a) shows the output power-current characteristic of a 1-mm-long hybrid laser. The lasing spectrum at various current densities is presented in the inset of Fig. 4.10(a). At this cavity length, referring to Fig. 4.4(b), the threshold current density is expected to be $\sim 20\text{cm}^{-1}$, while the measured saturated modal gain for QD ES1, as seen in the Fig. 4, is $\sim 17\text{cm}^{-1}$, therefore, the gain of the ES1 transitions is not enough to compensate for the total loss, and the lasing proceeds via the QW transition at 1150nm with a current density of 690A/cm^2 , this is in line with the modal gain results for QW, with lasing occurs at a point where a threshold modal gain for lasing is reached. When the current density reaches 900A/cm^2 , an additional lasing emission appears at $\sim 1128\text{nm}$, which is attributed to the ES1 of the QDs. Fig. 4.10(b) shows the integrated lasing peaks of the ES1 and QW verses current densities, as seen, coincident with the onset of lasing, a rising slope of the QW line is observed, further

increasing the current density, the integrated intensity of ES1 peak saturates, with the integrated intensity of ES1 peak still increases with increasing current densities. Also we observed that the measured FWHM of the lasing peak for QW broadens obviously over this interval.

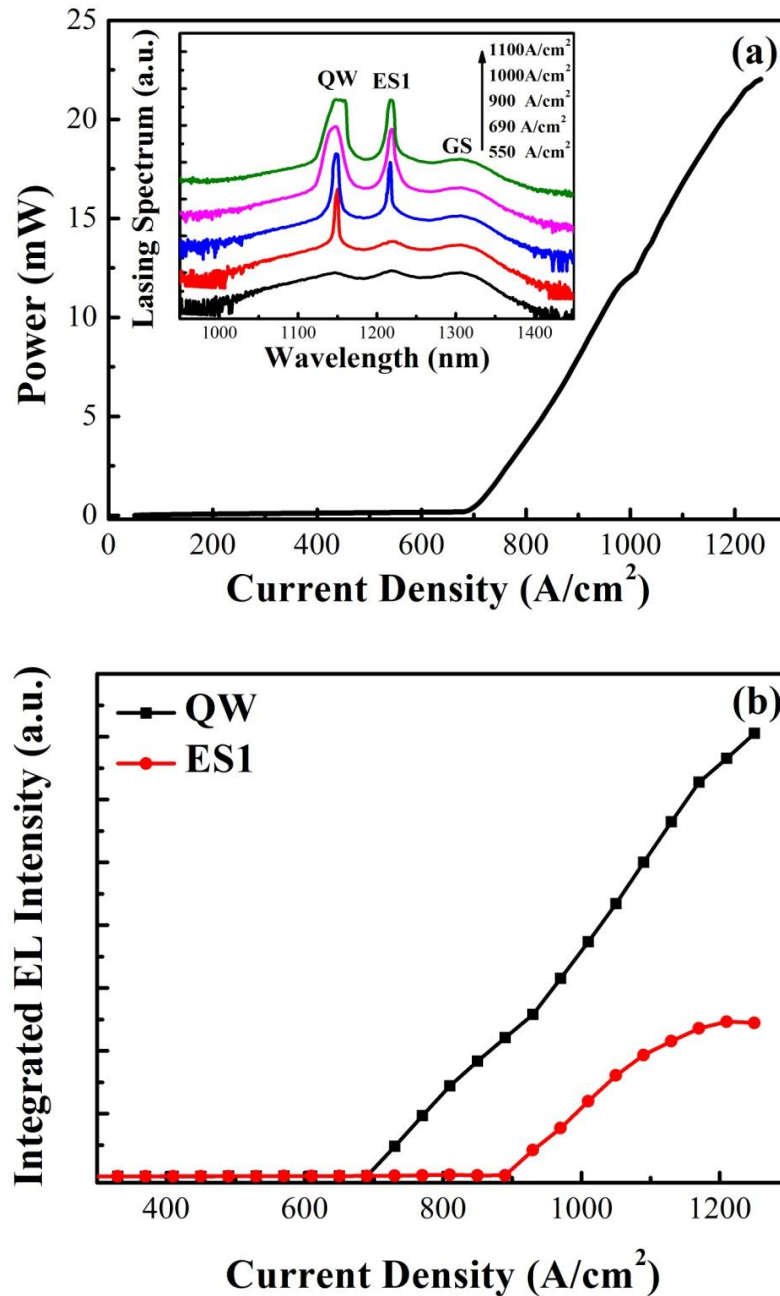


Fig. 4.10 (a) Output power-current characteristics of 1-mm-long hybrid laser. The inset shows the Lasing spectra at various current densities. (b) Integrated lasing peak intensities of ES1 and QW versus current densities.

It is to be noted that, unexpected GS lasing (ES1 lasing) is observed for 2-mm-long (1-mm-long) device, as for the 2-mm-long hybrid laser, the lasing of the GS occurs at a *higher* current density than the ES1 and the QW. This kind of lasing sequence is rather different from the results obtained from a 3-mm-long hybrid laser and the observations reported previously [8, 9, 20] where lasing occurs in the sequence of GS, ES1 and ES2. Also, for the 1-mm-long device, we observed that the lasing of ES1 occurs at a *higher* current density than the QW. The reason for those observed unexpected lasing phenomenon is not entirely clear, but may be due to the optical pumping of the QDs by the QW emission, where photons generated by the QW within the cavity are absorbed by the QDs, leading to more efficient filling of the QDs, effectively raising the GS/ES1 gain and enabling lasing from the GS/ES1. It should be remembered that if the QDs pin at an average carrier occupancy of ~ 6 e-h pairs per QD, the peak modal gain at 1130nm is made up of both gain from the QW and absorption in the QDs. Once lasing occurs, a much larger intracavity optical power is generated which may bleach this absorption, filling the QDs. Self pulsation/mode-locking of these lasers cannot be ruled out but has not been investigated.

4.5 Conclusion

In summary, I have shown that due to the combined contribution to gain spectrum from GS and ES1 of the QD and the lowest energy transition of the QW, positive modal gain spanning ~ 300 nm at room temperature, covering the wavelength of

1100-1400nm can be achieved. In particular, we have revealed that, the modal gain for QD ES1 can be clamped at low current density whilst the QW still increases in modal gain with further increasing current density.

Bias-controlled room temperature operation of simultaneous multi-state lasing over 160nm has been discussed, and it is shown that, three-state lasing can be achieved by using hybrid QW/QD structure, and the threshold current density for achieving three-state lasing has been reduced from 23000 to 1025A/cm² for the 3-mm-long device. In addition, by changing the cavity length/optical loss, different lasing sequences for achieving three-state lasing has been observed. Furthermore, unexpected lasing for certain cavity lengths has been introduced, suggesting the optical pumping of the QW to the QDs.

4.6 Future Work

Low threshold current density, temperature insensitivity and low chirp were reported from QD lasers, arising from zero-dimensional carrier confinement. However, due to their finite intraband relaxation time and the gain saturation effect, a high-modulation bandwidth has been recognized to be elusive to QD laser. Hybrid QW/QD laser may be a route to overcome modulation limitations of 1310 QD laser since the peak modal gain of GS can may be raised by optical pumping of QW emission, while the relaxation time can may be reduced due to fast photon-carrier scattering, leading to increased the modulation speed.

Reference

- [1] A. Kovsh, I. Krestnikov, D. Livshits, S. Mikhlin, J. Weimert, and A. Zhukov, "Quantum dot laser with 75nm broad spectrum of emission," *Opt. Lett.*, vol. 32, no 7, pp. 793-795, Mar, 2007.
- [2] H. S. Djie, B. S. Ooi, X. M. Fang, Y. Wu, J. M. Fastenau, W. K. Liu, and M. Hopkinson, "Room temperature broadband emission of an InGaAs/GaAs quantum dot laser," *Opt. Lett.*, vol. 32, no 1, pp. 44-46, Dec, 2007.
- [3] A. F. J. Levi, R. N. Nottenburg, R. A. Nordin, T. Tanbun-EK, and R. A. Logan, "Multielectrode quantum well lasers for digital switching," *Appl. Phys. Lett.*, vol. 56, no 12, pp. 1095-1097, Jan, 1990.
- [4] K. Berthold, A. F. J. Levi, S. J. Pearton, R. J. Malik, W. Y. Jan and J. E. Cunningham, "Bias-controlled intersubband wavelength switching in a GaAs/AlGaAs quantum well laser," *Appl. Phys. Lett.*, vol. 55, no 14, pp. 1382-1384, Jul, 1989.
- [5] A. P. Kanjamala, A. F. J. Levi, "Wavelength selective electro-optic flip-flop," *Electron. Lett.*, vol. 34, no 3, pp. 299-300, Feb, 1998.
- [6] W. D. Zhou, O. Qasaimeh, J. Phillips, S. Krishna, and P. Bhattacharya, "Bias-controlled wavelength switching in couple-cavity In_{0.4}Ga_{0.6}As/GaAs self-organized quantum dot lasers," *Appl. Phys. Lett.*, vol. 74, no 6, pp. 783-785, Dec, 1998.
- [7] D. Bimberg, M. Grundmann, and N. N. Ledentsov, *Quantum Dot Heterostructures* (Wiley, New York, 1998).
- [8] A. Markus, J. X. Chen, C. Paranthoën, A. Fiore, C. Platz, O. Gauthier-Lafaye, "Simultaneous two-state lasing in quantum-dot lasers," *Appl. Phys. Lett.*, vol. 82, no 12, pp. 1818-1820, Mar, 2003.
- [9] Z. Y. Zhang, Q. Jiang, and R. A. Hogg, "Simultaneous three-state lasing in quantum dot laser at room temperature," *Electron. Lett.*, vol. 46, no 16, pp. 1155-1157, Aug, 2010.
- [10] J. D. Thomson, H. D. Summers, P. J. Hulyer, P. M. Snowton, and P. Blood, "Determination of single-pass optical gain and internal loss using a multisection device," *Appl. Phys. Lett.*, vol. 75, no. 17, pp. 2527-2529, Aug. 1999.
- [11] P. Blood, G. M. Lewis, P. M. Snowton, H. Summers, J. Thomson, and J. Lutti, "Characterization of semiconductor laser gain media by the segmented contact method," *IEEE J. Select. Topics Quantum Electron.*, vol. 9, no 5, pp.1275-1282, Sep. 2003.

- [12] Y.-C. Xin, Y. Li, A. Martinez, T. J. Rotter, H. Su, L. Zhang, A. L. Gray, S. Luong, K. Sun, Z. Zou, J. Zilko, P. M. Varangis, and L. F. Lester, "Optical gain and absorption of quantum dots measured using an alternative segmented contact method," *IEEE J. Quantum Electron.*, vol. 42, no. 7, July, 2006.
- [13] S. Osborne, P. Blood, P. Snowton, J. Lutti, Y. C. Xin, A. Stintz, D. Huffaker, and L. F. Lester, "State filling in InAs quantum-dot laser structure," *IEEE J. Quantum Electron.*, vol. 40, no. 12, pp.1639-1645, Dec. 2004.
- [14] H. Shahid, D. T. D. Childs, B. J. Stevens, and R. A. Hogg, "Negative differential gain due to many body effects in self-assembled quantum dot lasers," *Appl. Phys. Lett.*, vol. 99, no. 6, pp. 061104-1 – 061104-3, Aug. 2011.
- [15] P. M. Snowton, I. C. Sandall, H. Y. Liu, and M. Hopkinson, "Gain in p-doped quantum well lasers" *IEEE J. Appl. Phys.*, vol. 101, no 1, pp. 013107-1 – 013107-7, Jan, 2007.
- [16] R. R. Alexander, D. T. D. Childs, H. Agarwal, K. M. Groom, H-Y. Liu, M. Hopkinson, R. A. Hogg, M. Ishida, T. Yamamoto, M. Sugawara, Y. Arakawa, T. J. Badcock, R. J. Royce, and D. J. Mowbray, "Systematic study of the effects of modulation p-doping on 1.3- μm quantum-dot lasers," *IEEE J. Quantum Electron.*, vol. 43, no. 12, Dec, 2007.
- [17] D. R. Matthews, H. D. Summers, P. M. Snowton, and M. Hopkinson, "Experimental investigation of the effect of wetting-layer states on the gain-current characteristic of quantum-dot lasers," *Appl. Phys. Lett.*, vol. 81, no. 26, pp.4904-4906, Dec. 2002.
- [18] S. M. Chen, K. J. Zhou, Z. Y. Zhang, D. T. D. Childs, M. Hugues, A. J. Ramsay, and R. A. Hogg, "Ultra-broad spontaneous emission and modal gain spectrum from a hybrid quantum well/quantum dot laser structure," *Appl. Phys. Lett.*, vol. 100, no. 4, pp. 041118-1 – 041118-3, Jan. 2012.
- [19] S. M. Chen, K. J. Zhou, Z. Y. Zhang, O. Wada, D. T. D. Childs, M. Hugues, X. Jin and R. A. Hogg, "Room temperature simultaneous three-state lasing in hybrid quantum well/quantum dot laser," *Electron. Lett.*, vol. 48, no. 11, pp. 644-646. May. 2012.
- [20] M. Sugawara, N. Hatori, H. Ebe, M. Ishida, Y. Arakawa, T. Akiyama, K. Otsubo, and Y. Nakata, "Modeling room-temperature lasing spectra of 1.3 μm self-assembled InAs/GaAs quantum-dot lasers: homogeneous broadening of optical gain under current injection," *J. Appl. Phys.*, vol. 97, no 4, pp. 043523-1 – 043523-8, Jan, 2005.

Chapter 5: Realization of Ultra-Broad Bandwidth Superluminescent Diodes Using Hybrid QW/QD Structure

5.1 Introduction

Since the axial resolution of OCT is governed by the coherence length [1-3], which is inversely proportional to the spectral bandwidth of the light emitting source, superluminescent diodes (SLDs) with a large spectral bandwidth are attractive for OCT because they are compact and relatively inexpensive. In previous chapters, I have reported the first hybrid quantum well/quantum dot active region to achieve broad spontaneous emission and gain spectra [4]. The positions and the values for modal gain are further confirmed by obtaining three-state lasing [5].

In this chapter, I report a hybrid quantum well/quantum dot superluminescent diode, In addition to the QD ground state (GS) transition, the QD first excited state (ES1) transition and the lowest energy transition of single QW (e1-hh1 transition), I show that emission from high order QW transitions (e1-hh2 and e1-hh3) at high current density, contributes to enhancing the spectral bandwidth by ~70nm. As a result, due to the combined contribution to the emission spectrum from the QD GS, QD ES1, and the QW, a 3-dB emission bandwidth of 289nm centered at 1198nm with a

corresponding output power of 2.4mW is achieved at room temperature. The hybrid QW/QD SLD is then assessed for application in an OCT system, the ultra-broad bandwidth enables a predicted axial resolution of $\sim 2.9\mu\text{m}$, a factor of 3-5 times better than standard OCT system using SLDs [2].

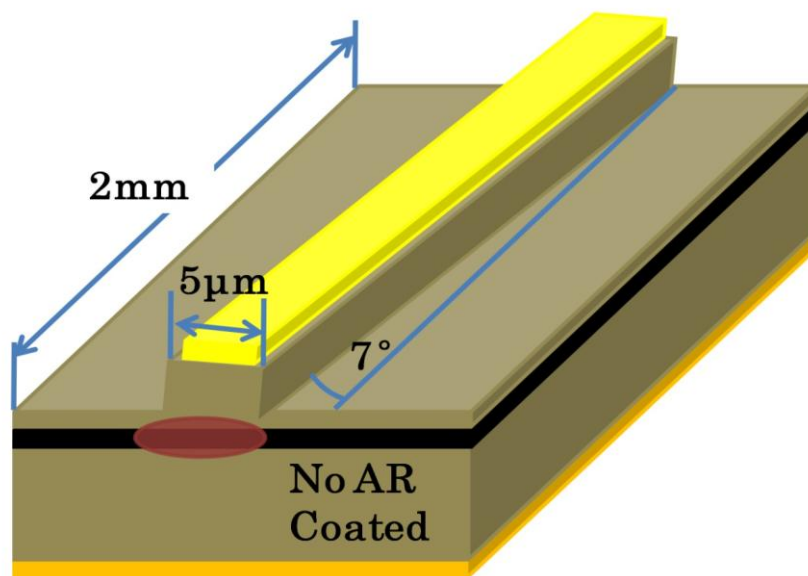


Fig. 5.1 Schematic diagram of the single contact SLD. The device is 2mm in length and $5\mu\text{m}$ in width. The device is 7° tilted to inhibit lasing.

5.2 Experiments

The device structure consisting of six-stacked InAs QD layers and a single InGaAs QW embedded in an AlGaAs waveguide was grown on a (100) Si-doped GaAs substrate by a V90 MBE reactor. A detailed description of this structure can be found in [4]. To obtain a high quality QW with a sharp interface between the QW and the GaAs barriers, a low growth rate and relatively high growth temperature have been used for the high indium concentration InGaAs QW and GaAs barriers. To achieve

high dot density with large-size inhomogeneity, here a relatively low growth temperature was used during the formation of the QDs. The hybrid QW/QD SLDs were fabricated in a tilted-waveguide structure following standard ridge laser processing. 5 μm and 15 μm wide ridges were defined by inductively coupled plasma etching to a depth of 1.5 μm . The SLDs described in this chapter were 5 μm in width and 2mm in length. The stripe widow was tilted at 7 degree to inhibit lasing. A schematic diagram of the geometrical design is shown in Fig .5.1. No facet coating was applied. To characterize the spontaneous emission and photocurrent (PC) spectra, standard optical access mesa diodes were also fabricated as described in chapter 3.

5.3 Results and discussion

Fig 5.2 shows the PL spectra of the hybrid QW/QD structure at 15K as a function of excitation power. In weak excitation conditions, PL originating from recombination of an electron and hole pair in the energy levels of the QDs (GS) and in the lowest energy level of the QW (e1-hh1) is observed at 1203nm and 1068nm, respectively. With an increase of the excitation power, an additional peak at 1134nm is clearly observed, which is attributed to the ES1 of the QDs, further increasing the excitation, the PL intensities of GS and ES1 saturate, while the PL intensity of the lowest energy transition of QW still increases with increasing excitation. In addition, an additional shoulder associated with high order QW transitions clearly appears at the high energy side of the QW peak.

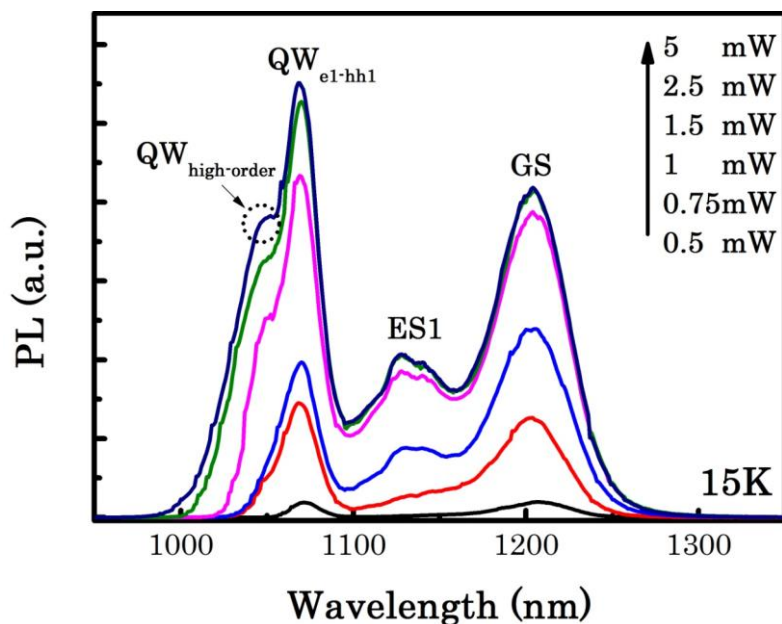


Fig. 5.2 PL spectra of the hybrid QW/QD structure at 15K as a function of excitation power.

The high order QW transitions are also observed in the EL spectra, (as shown in Fig 5.3) which are obtained from mesa diode (measured normal to the surface of the mesa diode) at room temperature at high injection currents. A feature at short wavelength of $\sim 1000\text{nm}$ has also been observed, and this is attributed to the emission from GaAs.

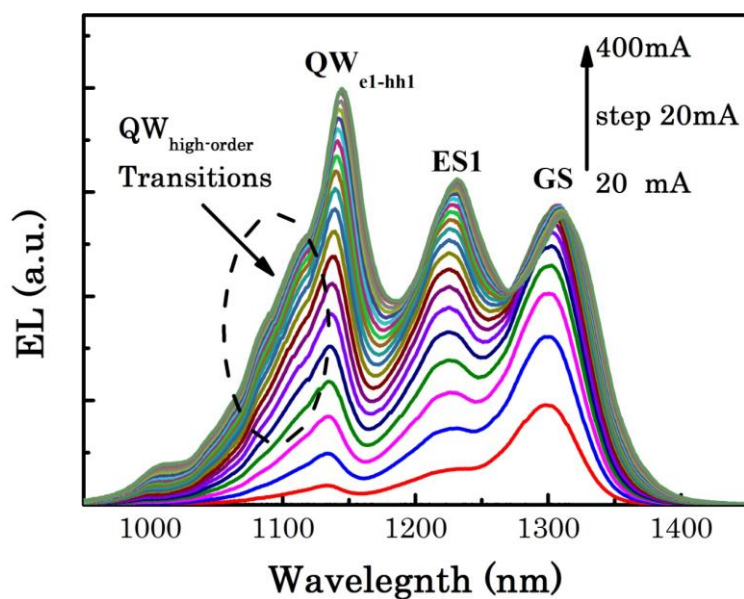


Fig. 5.3 Spontaneous emission spectral measured from hybrid QW/QD mesa diode as a function of current at room temperature.

To determine the origin of these high order transitions, PC experiments were also carried out on the same mesa diode, which was used for EL measurement. Fig 5.4 (a) shows the PC spectra as a function of applied reverse bias and an EL spectrum at a current density of 1.4KAcm^{-2} at room temperature. In the PC spectra, a linear shift of the QD interband transitions (GS and ES1) to lower energy is clearly observed with increasing reverse bias, suggesting that the dots have a permanent dipole moment at 0V [6]. A strong PC signal is observed at $\sim 1.09\text{eV}$. Comparison to data for a control sample (as shown in the Fig. 5.4 (b)), which contains only QDs suggests that this peak is due to the QW. As the applied reverse bias is increased, a quadratic shift of the energy transitions to lower energy and a concomitant broadening of the PC peak is observed due to the quantum confined Stark effect (QCSE) [7]. The agreement with the predicted transition (see inset) and QCSE allows us to attribute this feature to absorption by the e1-hh1 QW transition. To higher energy, at low reverse bias, weak transitions at $\sim 1.12\text{eV}$ and $\sim 1.15\text{eV}$ are resolved, which we attribute to the higher QW energy transitions of e1-hh2 and e1-hh3, due to the agreement with predicted transitions as shown in the inset of Fig 5.4 (a). At high reverse bias, more pronounced transitions for e1-hh2 and e1-hh3 are observed. Compared to the e1-hh1 transition, a relatively small energy shift is seen for e1-hh2 and e1-hh3 in agreement with the higher energy transitions being less sensitive to applied reverse bias than the lower energy transitions [8], and this have been theoretically explained in terms of the shifts of sub-band energies by the electric field [8, 9].

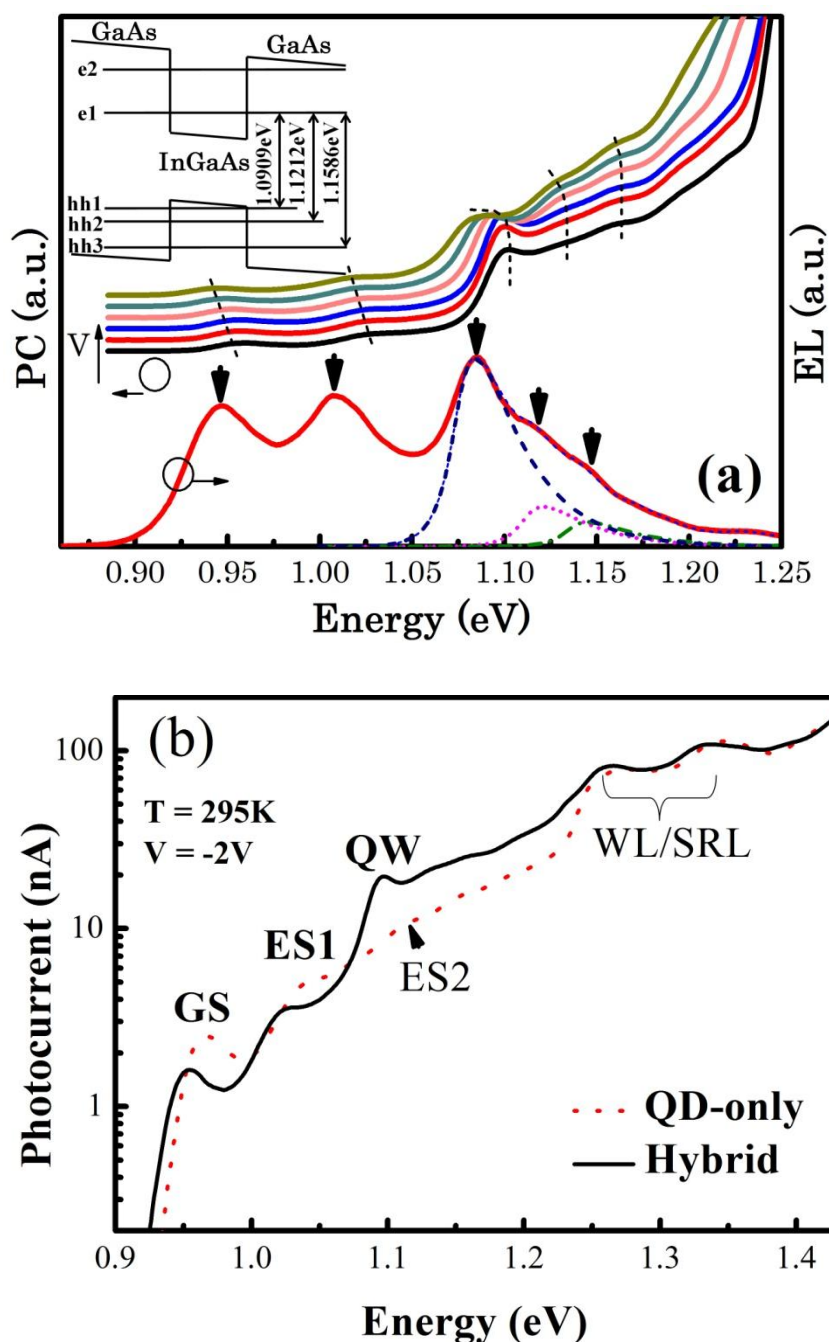


Fig. 5.4 (a) PC spectra as a function of applied reverse bias and an EL spectrum at a current density of 1.4KAcm^{-2} for hybrid QW/QD samples measured normal to the surface of an optical access mesa diode at room temperature. The inset shows the modeling results of the band structure for a single InGaAs quantum well. The QW energy levels were calculated using an effective mass approximation method. This model included temperature and strain dependent effects, and standard material parameters. A single 7 nm 34% InGaAs QW was simulated, clad with GaAs barriers on either side. An electric field of 10 kV/cm was also applied to the simulation structure. (b) PC spectra for hybrid sample and QD-only sample at room temperature at a reverse bias of -2V.

The EL spectrum (Fig 5.4 (a) Lower) shows clear luminescence peaks at 0.95eV and 1.02eV, due to the GS and ES1 transitions of the ensemble of InAs QD's. The peak which dominates the spectrum at ~1.09eV, has been shown to be due to the lowest energy transition of the single $\text{In}_{0.34}\text{Ga}_{0.66}\text{As}$ QW [4, 5, 10], and chapters [see chapter 3, 4]. Two more features are observed at ~1.12eV and ~1.15eV. Very good agreement between the QD and QW transition energies in PC and EL is observed. I therefore attribute the features observed at ~1.12 and ~1.15eV in EL to the transitions involving the lowest electron state and higher order hole states in the QW (e.g. e1-hh2, e1-hh3). In order to investigate the contribution of the high order QW transitions (e1-hh2, e1-hh3) to the spectral bandwidth of the device, lineshape fitting to the spontaneous emission spectrum was carried out by my colleague Jon Orchard, as shown in the Fig 5.4. The technique used for the fitting is described in [11]; the experimental spectrum was compared with a theoretical lineshape. Here we found that the higher order transitions are contributing ~33% to the spectrum at this current density. And a detailed description of the origin of such high intensity high order transitions (e1-hh2, e1-hh3) will be discussed in chapter 6.

Fig 5.5 shows the output power as a function of the injection current (L-I) of the hybrid QW/QD SLD. Device measurements were taken with the device mounted epi-side up with a sub-mount temperature of 20 °C under pulsed operation. Under pulse conditions of 1% duty-cycle and 5 μs pulse-width, superluminescent behavior is evidenced by the superlinear increase in optical power with increasing current. A peak

power of 4.6mW was measured at 1200mA, it should be noted that this is an underestimation of the power as a wavelength of 1300nm (0.95eV) was assumed. The inset of Fig 5.5 demonstrates the output power as a function of temperature at fixed duty-cycle and pulse-width (1%, 1 μ s). At 20 °C, a maximum output power of 11mW is achieved. By increasing the temperature from 20-50 °C, the output power decreases significantly. This strong effect of temperature on the L-I characteristics is attributed to increased nonradiative recombination and carrier escape from the heterostructures with increasing temperature [12]. It is well known that, The SLD is driven by both spontaneous emission and gain within the device. Increasing the temperature results in an increase in J_0 (point where transition from linear to superliner) from ~400mA at 20 °C to ~700mA at 50 °C (see inset of Fig. 5.5). This increase in J_0 is attributed to a reduction in carrier lifetime. Auger combination is very important in 1.3 μ m InAs QDs, and it has been widely reported that the existence of auger recombination in 1.3 μ m InAs QDs device explain the relatively low characteristic temperature at room temperature. Also as the temperature is increased, carriers can gain much more thermal energy and therefore they can easily “jump” out from the QDs. As seen in Fig 5.5, increasing the duty-cycle from 1% to 10% the maximum output power was reduced from 4.6mw to 2.4mW. Comparison to the inset indicates that self-heating of the device due to non-ideal heat sinking leads to a 10 – 15 °C temperature increase in the region of the junction at 1200mA when we move from 1% to 10% duty cycle. These thermal effects may be reduced by either p-doping the active region [13] or by using epi-down mounting process [14].

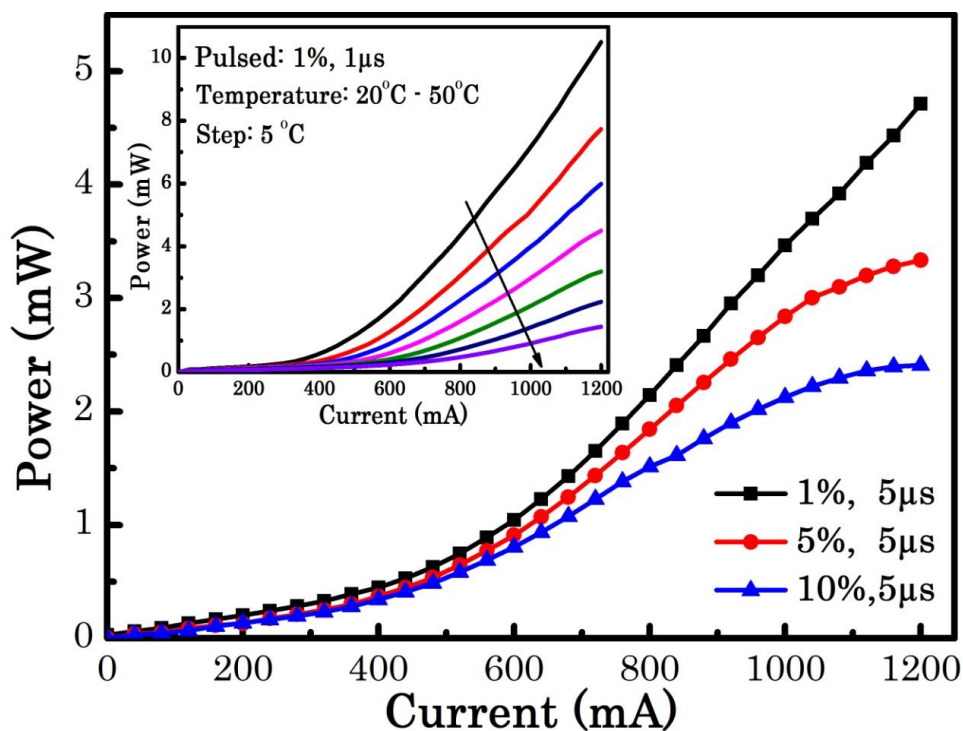


Fig. 5.5 L-I curve of the hybrid QW/QD SLD as a function of duty cycle. The inset shows the output power as a function of temperature at fixed duty-cycle and pulse-width (1%, 1 μs).

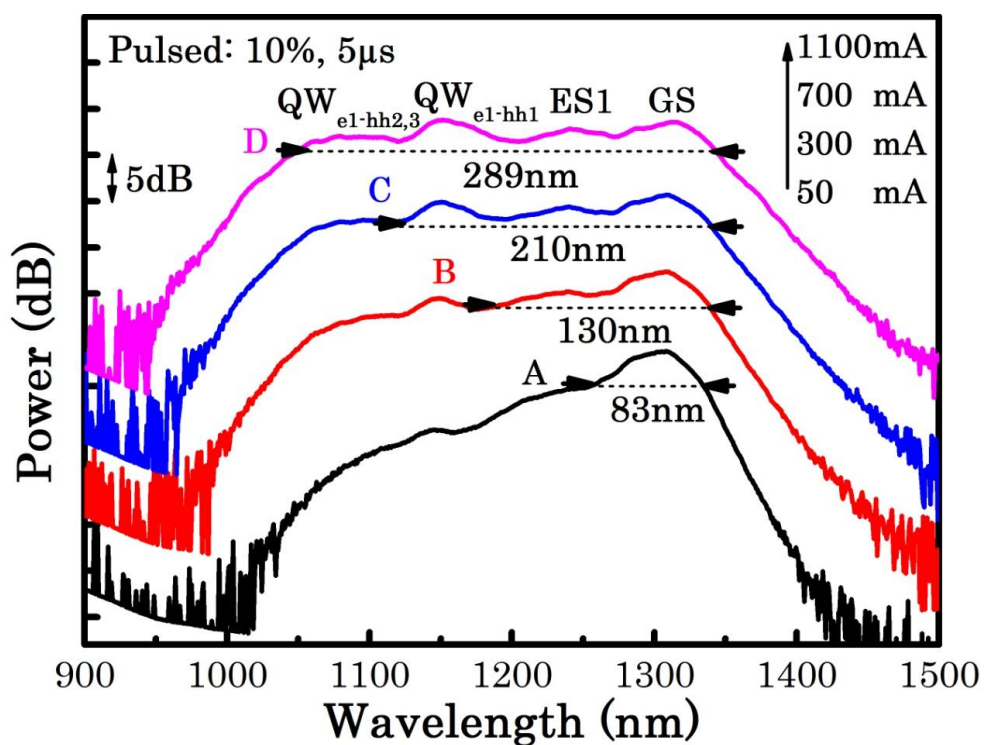


Fig. 5.6 Output power spectrum as a function of the injection current under pulsed operation (10% duty-cycle and 5 μs pulse-width) measured at room temperature.

Fig 5.6 plots the output power spectrum as a function of the injection current under pulsed operation (10% duty-cycle and 5 μ s pulse-width) measured at room temperature. The spectra are offset for clarity. At a drive current of 50mA, the emission is dominated by the ground state of the QDs at 1305nm. As the injection current is increased to 200mA, the ground state peak intensity saturates and the carriers begin to fill ES1 at 1230nm. With the further increase of drive current beyond 500mA, the QD emission begins to saturate, while an emission peak at 1150nm, due to the lowest energy transition of the QW increases, and gradually dominates the emission spectrum at the highest current. This is in line with previous work (see chapter 4) where I measured the gain spectrum of this material, and observed that the modal gain for GS and ES1 of the QDs is clamped at a certain current density, whilst the QW still increases in modal gain with further increasing current density [4]. In addition, at higher current, a shoulder in the emission spectrum between 1050 and 1100nm emerges, which further contributes to the full width at half maximum (FWHM) of the emission spectrum. These spectral features between 1050nm and 1100nm are attributed to higher order transitions of the QW as discussed in Fig 5.3.

Fig 5.7 illustrates the evolution of the FWHM as a function of the injection current obtained from the output power spectrum. Under low injection current, the GS makes the main contribution to the emission. As the current is increased, the emission spectra are broadened to the short wavelength side, which is attributed to the filling of the QD's ES1. Due to simultaneous contribution from the QD's GS and ES1, the

emission bandwidth is increased from $85 \pm 1 \text{ nm}$ (at 150mA) to $130 \pm 2 \text{ nm}$ (at 300mA) (see Fig 5.6). This is in line with previous work on a modulation p-doped QD-only SLDs [15], and is demonstrated in the inset of Fig 5.7, where the introduction of excited state emission increases the spectral bandwidth. However for this QD-only SLD, as the current is further increased, the spectrum becomes dominated by the ES leading to a reduction in FWHM to a value similar to that obtained for the GS. These effects have also been observed by other groups [16, 17, 18]. Here, for the hybrid QW/QD SLD, the QD's emission saturates and the emission due to the lowest energy transition of the QW gradually increases with increasing current. Due to the combined contribution from both the GS and the ES1 of the QD's and the lowest energy transition of the QW, the device exhibits an emission with a 3dB bandwidth of $\sim 210 \text{ nm}$ at 600mA. Further increasing the current induces higher energy transitions of the QW, and as a result, an emission spectrum with a 3dB bandwidth of 289nm, centered at 1198nm is achieved with a corresponding output power of 2.4mW. It should be noted that the power is integrated over the bandwidth.

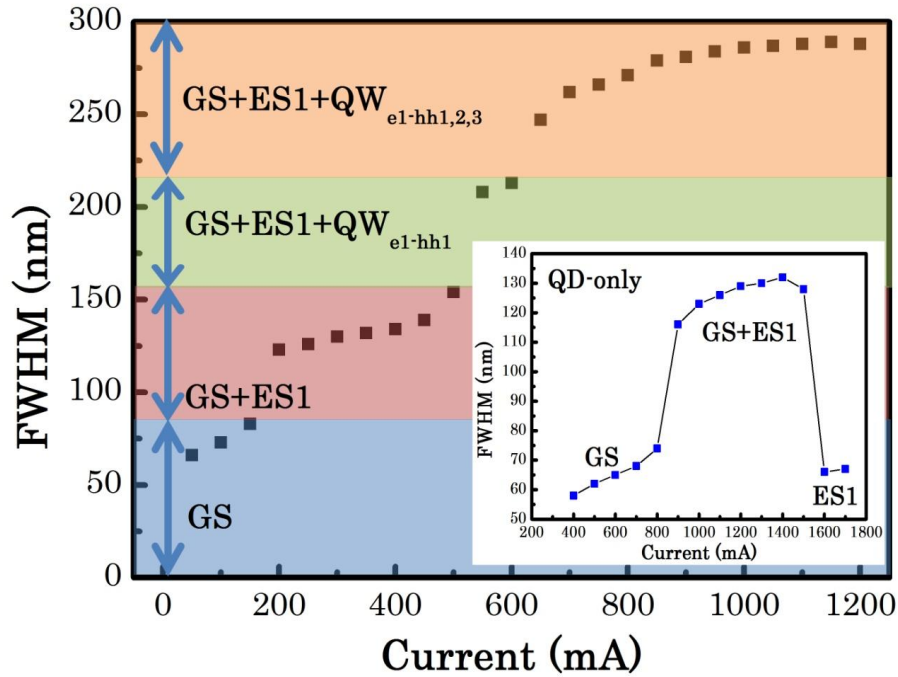


Fig. 5.7 Evolution of the FWHM versus the injection current obtained from the output power spectrum of hybrid QW/QD SLD. The inset shows the evolution of the FWHM as a function of current for a modulation p-doped QD-only SLD, which is processed by post-growth intermixing.

For application in an OCT system, the coherence length (and hence axial resolution) impacts upon the self-coherence function, which is given by the inverse Fourier transform of the power spectral density (PSD) and can be regarded as the point-spread function (PSF) of the imaging system [19]. A detailed description of derivation of the longitudinal resolution i.e. coherence length can be found in [19]. Referring to equation 1.1 and 1.2, the coherence length is inversely proportional to the spectrum bandwidth. And the axial resolution possible in an OCT imaging system can be approximated as being half the FWHM of the Fourier transform of the PSD. Whilst this is true for a Gaussian emission spectrum more complex emission spectra produce sidelobes (due to higher frequency components) in the self-coherence function. These will generally act to slightly reduce resolution. As demonstrated in Fig 5.8 (a)-(d), the

axial resolution is governed by the FWHM of the self-coherence function, which is gradually improved with increasing the FWHM of the emission spectrum. As seen in Fig 5.8 (a), for the emission spectrum with a bandwidth of 80nm, a resolution of 11 μm is obtained. Shown in Fig. 5.8 (b), as the spectrum bandwidth is increased to 130nm, the resolution is improved to 5.2 μm . In the end, as seen in Fig 5.8 (d), due to the combined contribution to emission from QD GS, QD ES1, and $\text{QW}_{\text{el-hh1,2,3}}$, an axial resolution of $\sim 2.5 \mu\text{m}$ is predicted for a Gaussian emission of 289nm 3dB bandwidth. In order to accommodate the undesirable side-lobe, generated by the more complex spectral structure, we need to introduce the Rayleigh criterion for resolution, which is explored in the inset of Fig 5.9. Here, a resolution of 2.9 μm is obtained, indicating that a $\sim 0.4 \mu\text{m}$ penalty is introduced to OCT system axial resolution due to the PSF side-lobes of the device [19, 20]. This ‘penalty’ may be reduced by reducing the spectral dips between QD GS and ES, QD ES and QW. This can be achieved by chirping the QDs to have different emission wavelength [21] or post growth intermixing [22].

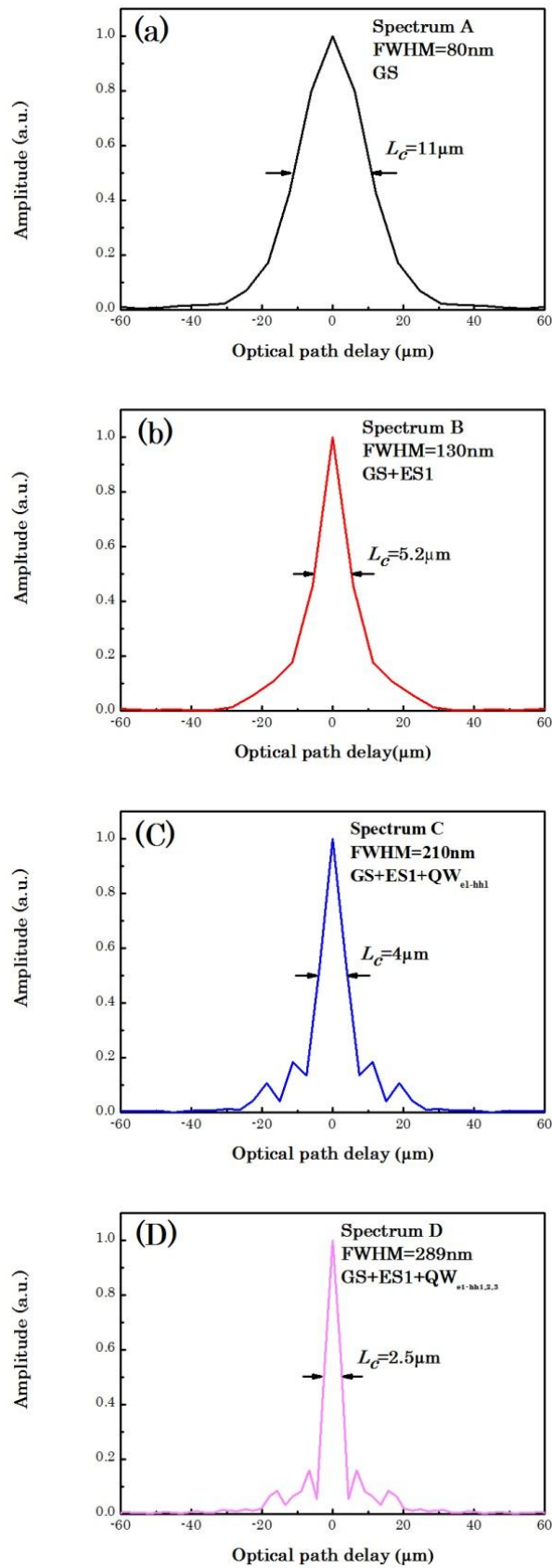


Fig. 5.8 Self-coherence function calculated from the different emission spectra as a labeled in Fig. 5.6. The self-coherence function is obtained by the inverse Fourier transform of the PSD.

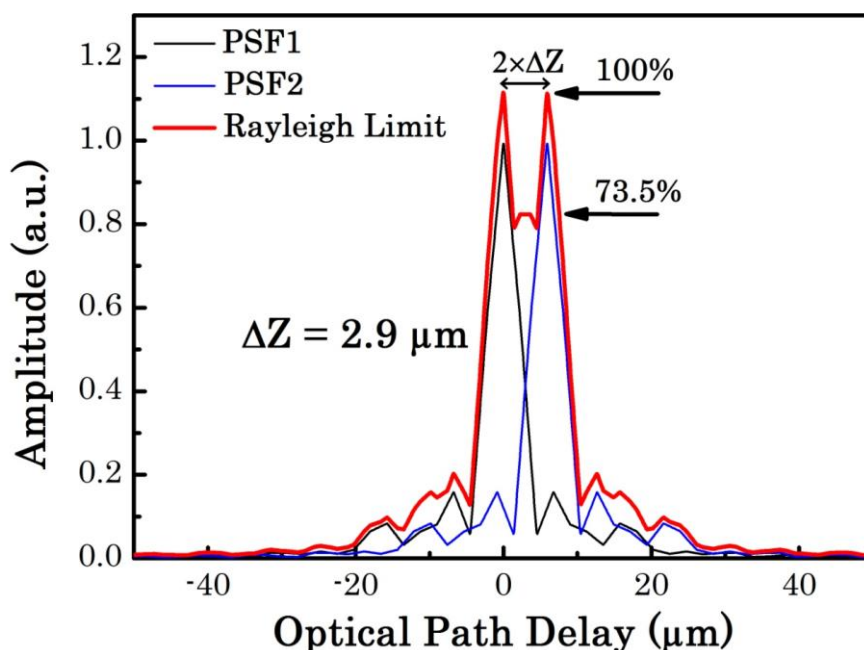


Fig. 5.9 Plot of envelope of the two point-spread function by introducing the Rayleigh criterion.

5.4 Conclusion

In this chapter, the first hybrid QW/QD SLD, which is capable of emitting an emission bandwidth of 289nm centered at 1198nm with a corresponding peak power of 2.4mW at room temperature, has been achieved. This is due to the combined effects of introducing a single QW into a multi-stack of QD layers, spectrally positioned to offset the loss due to the ES2 of the QDs, as well as introducing higher order QW transitions. The hybrid QW/QD SLD is then assessed for application in an OCT system. By introducing the Rayleigh criterion for resolution, a resolution of 2.9 μ m is obtained from the optimal result. Compared with current state-of-the-art with only-QDs structure, there is a significant improvement of over 50% in terms of spectrum bandwidth. And this device has the potential to insight into sub-cellular

imaging of skin tissue.

5.5 Future work

As discussed previously, thermal effects are a big issue for SLDs (see chapter 1), and as demonstrated in this chapter, a typical superluminescent phenomenon is only observed under pulsed operation. To reduce this thermal effect and therefore to achieve CW operation, it may be necessary to use epi-side down mounting process [13] and p-doping the active region [14]. Utilizing a larger number of QD layers with higher areal density [23] may also lead to SLDs working at high temperature.

The origin of higher order QW transitions will be discussed in the following chapter, which may be further exploited for even higher bandwidths.

Reference

- [1] D. Huang, E. A. Swanson, C. P. Lin, J. S. Schuman, W.G. Stinson, W. Chang, M. R. Hee, T. Flotte, K. Gregory, C. A. Puliafito, and J. G. Fujimoto, “optical coherence tomography,” *Science.*, vol. **254**, pp. 1178-1181, Nov. 1991.
- [2] W. Drexler, U. Morgner, R. K. Ghanta, F. X. Kartner, J. S. Schuman, and J. G. Fujimoto, “Ultrahigh-resolution ophthalmic optical coherence tomography,” *Nat Med.*, vol. **7**, no. 4, pp. 502-507. Apr. 2001.
- [3] R. C. Youngquist, S. Carr, and D. E. N. Davies, “Optical coherence-domain reflectometry: a new optical evaluation technique,” *Opt. Lett.*, vol. **12**, no.3, pp.158-160. Mar.1987.
- [4] S. M. Chen, K. J. Zhou, Z. Y. Zhang, D. T. D. Childs, M. Hugues, A. J. Ramsay, and R. A. Hogg, “Ultra-broad spontaneous emission and modal gain spectrum from a hybrid quantum well/quantum dot laser structure,” *Appl. Phys. Lett.*, vol. **100**, no. 4, pp. 041118-1 – 041118-3, Jan. 2012.
- [5] S. M. Chen, K. J. Zhou, Z. Y. Zhang, O. Wada, D. T. D. Childs, M. Hugues, X. Jin and R. A. Hogg, “Room temperature simultaneous three-state lasing in hybrid quantum well/quantum dot laser,” *Electron. Lett.*, vol. **48**, no. 11, pp. 644-646. May. 2012.
- [6] P. W. Fry, I. E. Itskevich, D. J. Mowbray, M. S. Skolnick, J. J. Finley, J. A. Barker, E. P. O’Reilly, L. R. Wilson, I. A. Larkin, P. A. Maksym, M. Hopkinson, M. Al-Khafaji, J. P. R. David, A. G. Gullis, G. Hill, and J. C. Clark, “Inverted electron-hole alignment in InAs-GaAs self-assembled QD,” *Phys. Rev. Lett.*, vol. **84**, no. 4, pp. 733-736, Jan. 2000.
- [7] D. A. B. Miller, D. S. Chemla, T. C. Damen, A. C. Gossard, W. Wiegmann, T. H. Wood, and C. A. Burrus, “Band-edge electroabsorption in QW structure: the quantum-confined stark effect,” *Phys. Rev. Lett.*, vol. **53**, no. 22, pp. 2173-2176, Nov. 1984.
- [8] K. Yamanaka, T. Fukunaga, N. Tsukada, K. L. I. Kobayashi, and M. Ishii, “Photocurrent spectroscopy in GaAs/AlGaAs multiple quantum wells under a high electric field perpendicular to the heterointerface,” *Appl. Phys. Lett.*, vol. **48**, no. 13, pp. 840-842, Mar. 1986.
- [9] J. A. Brum and G. Bastard, “Electric-field-induced dissociation of excitons in semiconductor quantum well,” *Phys. Rev. B* vol. 31, no. 6, pp. 3893-3898, Mar, 1985.
- [10] S. Chen, K. Zhou, Z. Zhang, J. R. Orchard, D. T. D. Childs, M. Hugues, O. Wada, and R. A. Hogg, “Hybrid Quantum Well/Quantum Dot Structure for Broad

- Spectral Bandwidth Emitters,” *IEEE J. Select. Topics Quantum Electron.*, vol. **19**, no. 4, pp.1900209-1900209-9, Jul/Aug. 2013.
- [11] M. S. Skolnick, P. R. Tapster, S. J. Bass, A. D. Pitt, N. Apsley, and S. P. Aldred, “Investigation of InGaAs-InP quantum wells by optical spectroscopy,” *Semicond. Sci. Technol.*, vol. **1**, pp.29-40, Mar.1986.
- [12] I. P. Marko, A. R. Adams, S. J. Sweeney, D. J. Mowbray, M. S. Skolnick, H. Y. Liu, and K. M. Groom, “Recombination and Loss Mechanisms in Low-Threshold InAs–GaAs 1.3- μm Quantum-Dot Lasers,” *IEEE J. Sel. Topics Quantum Electron.*, vol. **11**, pp.1041-1047, Sep/Oct, 2005.
- [13] O. B. Shchekin and D. G. Deppe, “1.3 μm InAs quantum dot laser with $T_0 = 161\text{K}$ from 0 to 80°C ,” *Appl. Phys. Lett.*, vol. **80**, pp.3277-3279. May.2002.
- [14] X. Li, P. Jin, Q. An, Z. Wang, X. Lv, H. Wei, J. Wu, J. Wu, and Z. Wang, “Improved Continuous-Wave Performance of Two-Section Quantum-Dot Superluminescent Diodes by Using Epi-Down Mounting Process,” *IEEE Photon. Technol. Lett.*, vol. **24**, pp.1188-1190, Jul. 2012.
- [15] Z. Y. Zhang, Q. Jiang, I. J. Luxmoore and R. A. Hogg, “A p-type-doped quantum dot superluminescent LED with broadband and flat-topped emission spectra obtained by post-growth intermixing under a GaAs proximity cap,” *Nanotechnology.*, vol. **20**, no.5, pp. 055204-1– 055204-4, Jan. 2009.
- [16] Y. Xin, A. Martinez, T. A. Nilsen, A. Moscho, Y. Li, A. L. Gray, and L. F. Lester, “1.3 μm quantum dot multi-section superluminescent diode with extremely broad bandwidth ($>150\text{ nm}$),” *IEEE Photon. Technol. Lett.*, vol. **19**, no. 7, pp. 501–503, Apr. 2007.
- [17] M. Rossetti, A. Markus, A. Fiore, L. Occhi, and C. Vele, “Quantum Dot Superluminescent Diodes Emitting at 1.3 μm ,” *IEEE Photon. Technol. Lett.*, vol. **17**, pp.540-542. 2005.
- [18] Z. C. Wang, P. Jin, X. Q. Lv, X. K. Li and Z. G. Wang, “High-power quantum dot superluminescent diode with integrated optical amplifier section,” *Electron. Lett.*, vol. **47**, pp.1191-1192. 2011.
- [19] C. Ackay, P. Parrein, and J. P. Rolland, “Estimation of longitudinal resolution in optical coherence imaging,” *Appl. Opt.*, vol. 41, no. 25, pp. 5256– 5262, Aug. 2002.
- [20] K. J. Zhou, Q. Jiang, Z. Y. Zhang, S. M. Chen, H. Y. Liu, Z. H. Lu, K. Kennedy, S. J. Matcher, and R. A. Hogg, “Quantum dot selective area intermixing for broadband light sources,” *Opt. Express.*, vol. **20**, no. 24, pp. 26950-26957, Nov. 2012.

- [21] S. K. Ray, K. M. Groom, M. D. Beattie, H. Y. Liu, M. Hopkinson, and R. A. Hogg, "Broad-Band Superluminescent Light-Emitting Diodes Incorporating Quantum Dots in Compositionally Modulated Quantum Wells," *IEEE Photon. Technol. Lett.*, vol. **18**, pp.58-61. 2006.
- [22] Z. Y. Zhang, Q. Jiang, M. Hopkinson, and R. A. Hogg, "Effects of intermixing on modulation p-doped quantum dot superluminescent light emitting diodes," *Opt. Express.*, vol.**18**, no. 7, pp.7055–7063 (2010).
- [23] Y. Tanaka, M. Ishida, Y. Maeda, T. Akiyama, T. Yamamoto, H. Z. Song, M. Yamaguchi, Y. Nakata, K. Nishi, M. Sugawara, and Y. Arakawa, "1.3 μ m InAs/GaAs high-density quantum dot lasers," Optical Fiber Communication Conference (OFC) 2009, OWJ1

Chapter 6: Study of QD-Induced Strain Modulation of a QW

6.1 Introduction

In previous chapters, I have shown that high order QW transitions (e1-hh2, e1-hh3) are observed from hybrid QW/QDs devices (including mesa diodes and SLDs) through EL, and PC measurements. These transitions contribute to enhancing the spectral bandwidth by $\sim 70\text{nm}$ in hybrid QW/QDs SLDs (chapter 5). As these higher order QW transitions observed in hybrid QW/QD structure are highly desirable for achieving broad bandwidth [1], a fuller understanding of their origin is of importance, since in a regular QW, due to the selection rules, these higher order QW transitions (e1-hh2, e1-hh3) should have a very low oscillator strength.

In this chapter, I focus my attention on spatial strain modulation of the QW due to the QD layers. I experimentally demonstrate that in the hybrid QW/QD structure, the QD-induced strain of the QW can result in both broader QW transitions, and more pronounced high order transitions, both of which can be expected to be beneficial for broad spectral bandwidth devices.

6.2 Experiments

To investigate the effect of QD-induced strain on QW modulation, three p-i-n LED test structures, named “QW-only”, “QW+QD” and “QD-only” were studied. These LED test structures (schematically shown in the Fig. 6.1) were grown by a V90 solid source molecular beam epitaxy (MBE) reactor on a (100) Si-doped substrate by Dr Edmund Clarke. The epitaxy for the three test structures is essentially identical except for the growth of the active region. The epitaxy for the three test structures all start with a 200 nm thick n-type GaAs buffer layer ($2 \times 10^{18} \text{ cm}^{-3}$) followed by a 400nm n-type ($5 \times 10^{17} \text{ cm}^{-3}$) $\text{Al}_{0.35}\text{Ga}_{0.65}\text{As}$ lower cladding layer, above this is an undoped active region, followed by a 400nm p-type ($5 \times 10^{17} \text{ cm}^{-3}$) $\text{Al}_{0.35}\text{Ga}_{0.65}\text{As}$ upper cladding layer, and finally a 100nm highly p-doped ($1 \times 10^{19} \text{ cm}^{-3}$) GaAs contact layer. For the growth of the active region, for the QW-only test sample, a 7nm un-doped $\text{In}_{0.3}\text{Ga}_{0.7}\text{As}$ QW is sandwiched between 96.5nm of un-doped GaAs. For the QW+QD test sample, firstly 56.5nm of un-doped GaAs and then a 7nm un-doped $\text{In}_{0.3}\text{Ga}_{0.7}\text{As}$ QW was grown, this was followed by the deposition of 35nm of un-doped GaAs and then one un-doped $\text{In}_{0.18}\text{Ga}_{0.82}\text{As}/\text{InAs}/\text{In}_{0.18}\text{Ga}_{0.82}\text{As}$ dot-in-well (DWELL) layer [2] followed by 94nm GaAs layer. Due to the comparatively thick barrier between the QW and QD, no electronic coupling between the QW and QD layers is expected [3]. The growth of the active region for the QD-only test sample is nominally identical to that of the QW-only test sample, but with the QW replaced

by a single DWELL layer identical to that used in the QW +QD test structure. For characterizing the material properties such as spontaneous emission and PC, three test structures were fabricated into p-i-n optical mesa diodes [4]. PC was carried out using a tungsten-halogen lamp, dispersed by a Bentham M300 single monochromator. The PC signal was recorded using standard lock-in techniques.

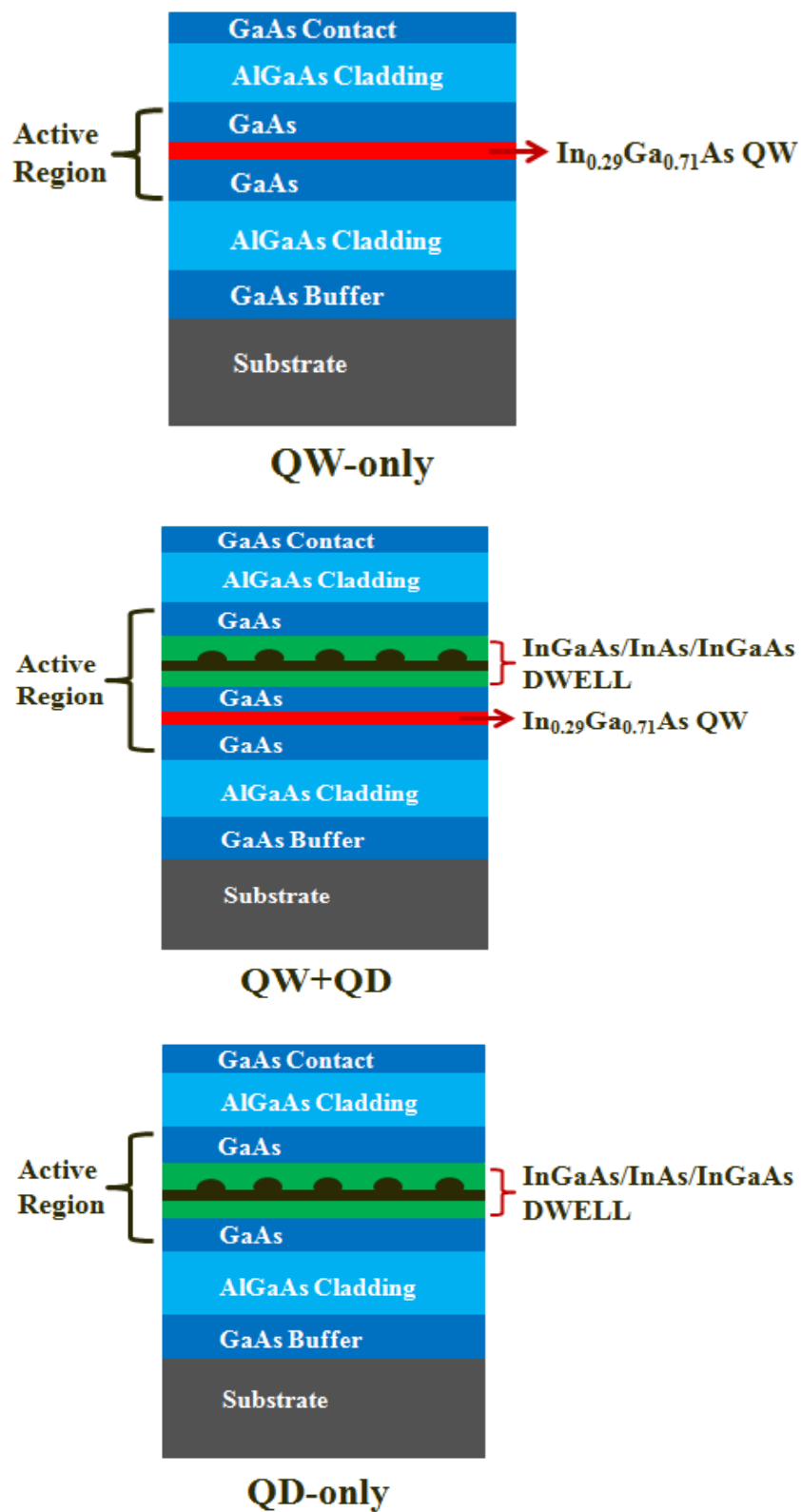


Fig.6.1 Schematics of the device structure for QW-only, QW+QD and QD-only test sample.

6.3 Results and Discussion

Photocurrent spectra for the QW-only, QW+QD and QD-only test samples measured normal to the surface of the an optical mesa diodes, as a function of reverse bias from 0 to 2V, are shown in Fig 6.2. For the QD-only test sample (the inset of Fig 6.2 lower), at 0V, a series of well-defined features, arising from the QD interband absorption (GS, ES1, ES2, etc.), are observed from 0.96eV to 1.13eV. With increasing reverse bias (it should be note that, it may be better converting to electric field rather than reverse bias for studying quantum confined Stark effect (QCSE). While the exact intrinsic region widths for QD and QW are unknown that can be calculated through capacitance-voltage measurements. I compared the effect of electric field on QD and QW in this set and previous samples based on their nominal width, the results are quite similar) all of the QD transitions shift linearly to low energy, the signature of the quantum confined Stark effect [5], but without any qualitative change in the form of the spectra. For the QW-only test sample, a strong PC signal due to the lowest QW interband absorption is observed at ~ 1.127 eV. For QW+QD test structure (the inset of Fig 6.2 upper), the PC spectra show clear absorption peaks at 0.96 and 1.016 eV, which indicate the GS and ES1 of InAs QD's interband transitions. In addition, a strong PC appears near 1.127eV, suggests that this peak is attributing to the lowest energy transition of the QW due to very good agreement with QW transition energy in QW-only PC spectra.

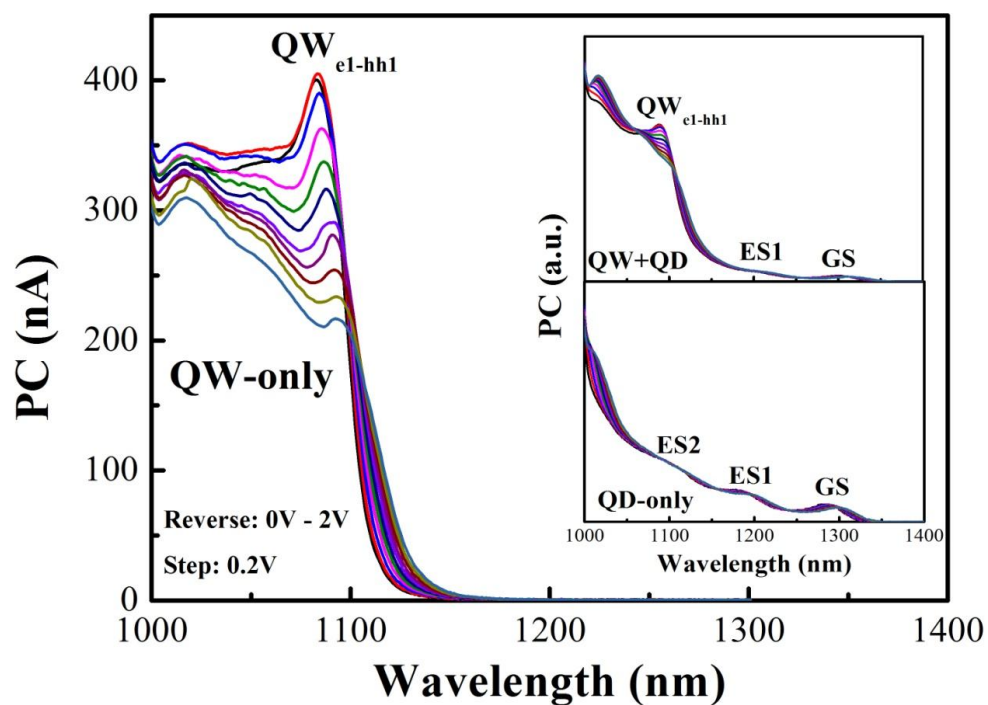


Fig. 6.2 Photocurrent spectra for QW-only, QW+QD, QD-only test samples as a function of reverse bias from 0 to 2V.

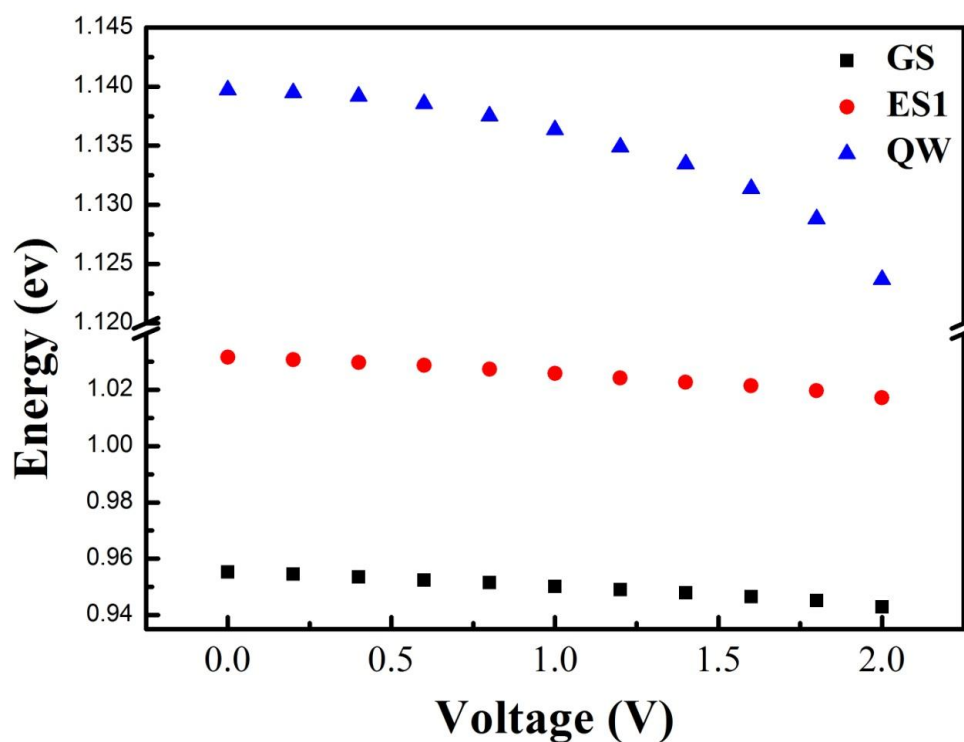


Fig.6.3 Transition energies for QD GS, QD ES1 and QW as a function of reverse bias from 0V to 2V at room temperature.

In order to further confirm the assignment of the 1.127eV PC signal in QW+QD test sample is due to the QW rather than due to the ES2 of the QD's, the transition energies for QD GS, QD ES1 and QW were plotted as a function of reverse bias from 0-2V in Fig 6.3. A linear shift of the QD interband transitions (GS and ES1) to lower energy is clearly observed, indicating again that the dots have a permanent dipole moment at 0V [6], for the strong PC signal observed at 1.127eV, as the applied reverse bias is increased, a quadratic shift of this transition to lower energy and a concomitant broadening of the PC peak is observed due to the quantum confined Stark effect (QCSE) [7]. The QCSE and the agreement with the predicted transition by modeling the InGaAs QW (discussed later) allow us to attribute this feature to absorption by the e1-hh1 QW transition.

Fig 6.4 shows the normalized QW PC spectra for the QW-only test sample and the QW+QD test sample at an electric field of 8kV/cm, (where the PC is maximized), at room temperature. To obtain the QW PC signal from the QW+QD sample, first of all, the normalization is made to the QD PC. The QW PC signal of the QW+QD test sample is then obtained by subtracting the normalized QD PC from the QW+QD PC. For the QW-only test sample, the PC spectrum shows a clear peak at 1083nm, which indicates the lowest energy transition of the QW. Very good agreement between the lowest energy transitions of the QW in the QW-only and QW+QD test samples is found. However, for the measured linewidth, (which is the full width at half maximum of the line, that corresponding to the best-fit assuming the sum of Gaussian

functions), the QW PC from the QW+QD test sample is found to have a broader linewidth than that for the QW-only test sample. The increased linewidths (from 30nm to 47nm), along with considerable band-tailing (1150-1200nm) is attributed to the modulation of the QW by a spatial strain modulation induced by the highly strained QDs [8-11]. The origin of this spatial strain modulation is presumably related to the effect of the elastic strain introduced by the lattice mismatched materials of the quantum dots and GaAs barrier [8], and also a change in the height of potential barrier near the QDs can possibly results in a local variation in the potential energy of carriers in the region of QW near QDs [8]. As the QW is grown first, the QDs cannot modulate the growth of the QW as was seen for the p-side QW in chapter 3.

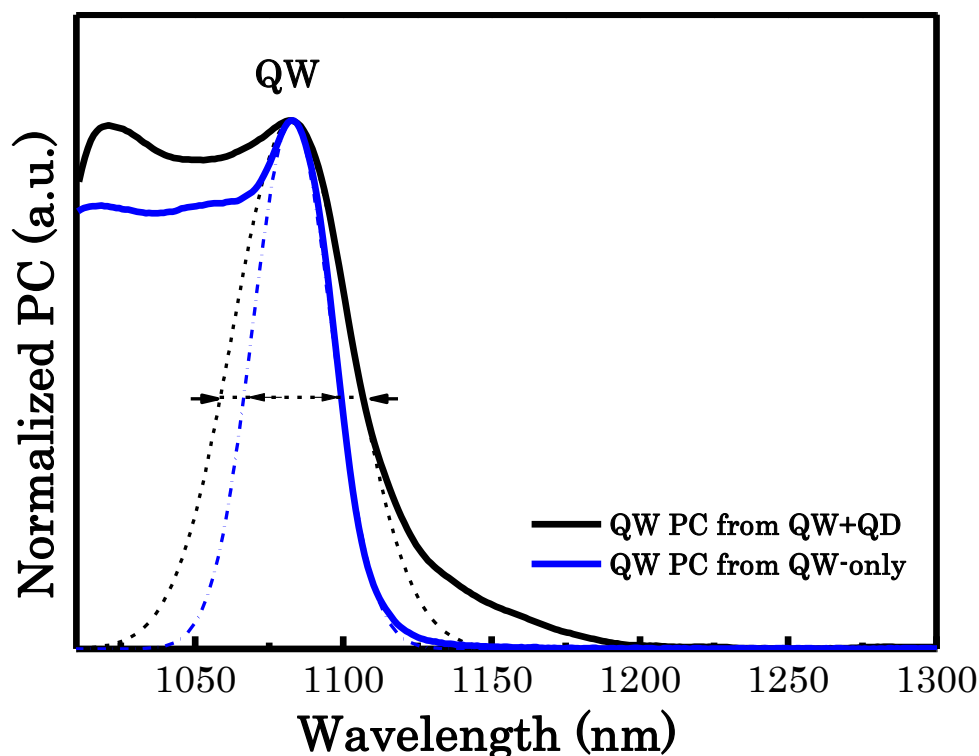


Fig.6.4 Normalized QW PC spectra for QW-only sample and QW+QD sample at an electric field of 8KV/cm (where the PC is maximized), at room temperature, the dash line corresponding the best-fit assuming the sum of Gaussian function. Here the normalization is made to the lowest energy state of QW.

Fig 6.5 shows the normalized EL spectra obtained from mesa diodes for the QW-only, QW+QD and QD-only test samples at room temperature. The QW-only and QW+QD test samples are driven with the same current density of 300Acm^{-2} . In order to investigate the contribution of the QDs to the emission in the QW+QD test sample, the QD-only test sample is injected at a specific current density (160Acm^{-2}) where the ratio of the emission from the QD ground-state and excited state are the same as that of the QW+QD test sample. It is assumed that at this current density/GS:ES ratio the QD carrier occupancy in the QW+QD test sample and QD-only test sample are the same. As indicated in the Fig 6.5, the EL spectrum for the QD-only test sample shows a series of well-defined features at 1293nm, 1200nm and 1116nm, which are attributed to the ground state, the first excited state and the second excited state of the QD transitions. For the QW-only test sample, only a single peak at 1084nm is observed attributed to the lowest energy transition of the QW (e1-hh1). By contrast, for the QW+QD test sample in addition to the e1-hh1 transition, two more features at 1058nm and 1018nm are observed. It is noted that a shoulder in QW+QD spectrum at $\sim 980\text{nm}$ is also observed, and this is attributed to the GaAs substrate emission. The energies of these features are in agreement with the predicted energies of higher order QW transitions (e1-hh2 and e1-hh3) from the modeling of single QW as shown in the Fig 6.6 [12]. Therefore, there is clear evidence of QW modulation due to QD-induced strain modulation. This effect is additional to the QD-induced strain modulation of epitaxy which was responsible for the modification of the p-side QW in chapter 3.

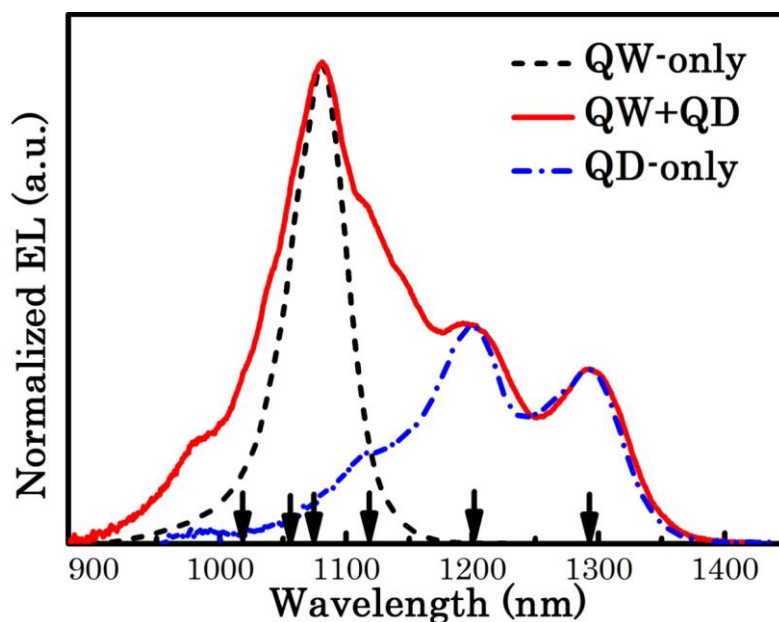


Fig. 6.5 Normalized EL spectra obtained from Mesa diodes (200 μ m) for QW-only, QW+QD, and QD-only test samples at room temperature under CW operation. The marks at the bottom (from the right to left) indicate the following transitions: QD GS, QD ES1, QD ES2, QW_{e1-hh1}, QW_{e1-hh2}, and QW_{e1-hh3}. While, the feature observed at 980nm is attributed to the emission from GaAs.

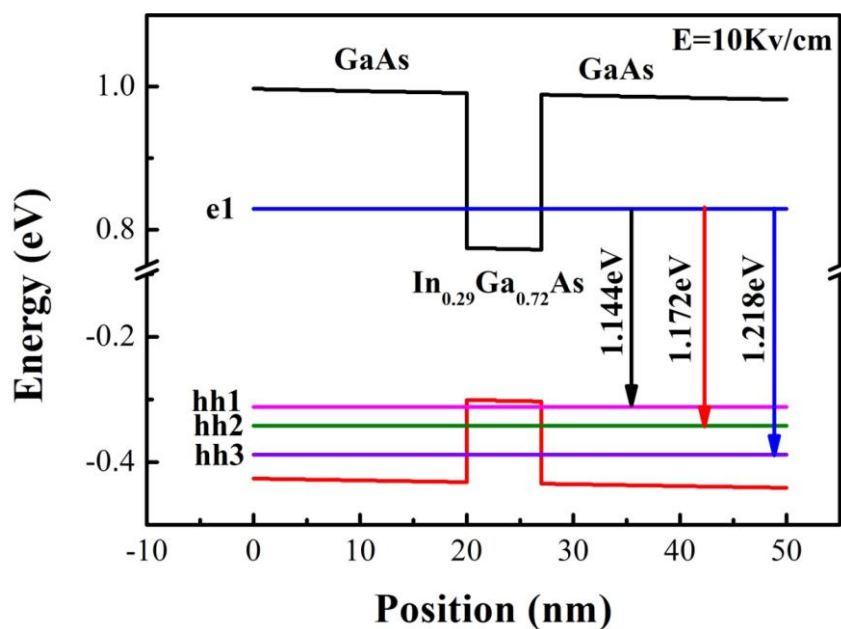


Fig. 6.6 Modeling results of the band structure for a single InGaAs quantum well. The QW energy levels were calculated using an effective mass approximation method. This model included the temperature- and strain-dependent effects, and standard material parameters. A single 7nm 29% InGaAs QW was simulated, clad with GaAs barriers on either side. An electric field of 10kV/cm was also applied to the simulation structure.

6.4 Summary

To summarize the results obtained from these test samples, QD strain modulation of the underlying QW, which is deposited *before* the QDs, results in a broadened linewidth of the e1-hh1 transition and leads to larger oscillator strengths for the higher order QW transitions (e1-hh2, e1-hh3). Based on this observation, we can also conclude that the QD-induced spatial strain modulation may be expected to play a significant role in introducing the high order QW transitions which further enhancing the spectral bandwidth by 70nm in our hybrid QW/QD SLD (discussed in chapter 5).

6.5 Future Work

This brief study shows a very large effect on the modulation of the QW due to the QD-induced strain (remembering that the QW is grown first). There is therefore an opportunity to insert QD layers in a QW active region design to enhance the spectral bandwidth of the QW. This may be best executed at 800nm for immediate application in ophthalmic imaging system [1].

Reference

- [1] T. Semenov, V. R. Shidlovski, S. A. Safin, “Wide spectrum single quantum well superluminescent diodes at 0.8 μm with bent optical waveguide,” *Electron. Lett.*, vol. **29**, pp. 854-856, May. 1993.
- [2] H. Y. Liu, I. R. Sellers, T. J. Badcock, D. J. Mowbray, M. S. Skolnick, K. M. Groom, M. Guti erez, M. Hopkinson, J. S. Ng, J. P. R. David, and R. Beanland, “Improved performance of 1.3 μm multilayer InAs quantum-dot lasers using a high-growth-temperature GaAs spacer layer,” *Appl. Phys. Lett.*, vol. **85**, no 5, pp. 704-706, Jun. 2004.
- [3] P. Bhattacharya and S. Ghosh, “Tunnel injection In_{0.4}Ga_{0.6}As/GaAs quantum dot lasers with 15 GHz modulation bandwidth at room temperature,” *Appl. Phys. Lett.*, vol. **80**, no. 19, pp. 3482-2484, Mar. 2002.
- [4] S. Chen, K. Zhou, Z. Zhang, J. R. Orchard, D. T. D. Childs, M. Hugues, O. Wada, and R. A. Hogg, “Hybrid Quantum Well/Quantum Dot Structure for Broad Spectral Bandwidth Emitters,” *IEEE J. Select. Topics Quantum Electron.*, vol. **19**, no. 4, Jul/Aug. 2013.
- [5] C. M. A. Kapteyn, M. Lion, R. Heitz, and D. Bimberg, P. N. Brunkov, B. V. Volovik, S. G. Konnikov, A. R. Kovsh, and V. M. Ustinov, “Hole and electron emission from InAs quantum dots,” *Appl. Phys. Lett.*, vol. **76**, no 12, pp. 1573-1575, Mar. 2000.
- [6] P. W. Fry, I. E. Itskevich, D. J. Mowbray, M. S. Skolnick, J. J. Finley, J. A. Barker, E. P. O’Reilly, L. R. Wilson, I. A. Larkin, P. A. Maksym, M. Hopkinson, M. Al-Khafaji, J. P. R. David, A. G. Gullis, G. Hill, and J. C. Clark, “Inverted electron-hole alignment in InAs-GaAs self-assembled QD,” *Phys. Rev. Lett.*, vol. **84**, no. 4, pp. 733-736, Jan. 2000.
- [7] D. A. B. Miller, D. S. Chemla, T. C. Damen, A. C. Gossard, W. Wiegmann, T. H. Wood, and C. A. Burrus, “Band-edge electroabsorption in QW structure: the quantum-confined stark effect,” *Phys. Rev. Lett.*, vol. **53**, no. 22, pp. 2173-2176, Nov. 1984.
- [8] A. F. Tsatsul’nikov, A. Yu. Egorov, A. E. Zhukov, A. R. Kovsh, V. M. Ustinov, N. N. Ledentsov, M. V. Maksimov, A. V. Sakharov, A. A. Suvorova, P. S. Kop’ev, Zh. I. Alferov, D. Bimberg, “Modulation of a quantum well potential by a quantum-dot array,” *Semiconductor.*, vol. **31**, pp.88-91, Jan. 1997.
- [9] U. Zeimer, F. Bugge, S. Gramlich, V. Smirnitcki, M. Weyers, G. Tra nkle, J. Grenzer, U. Pietsch, G. Cassabois, V. Emiliani, and Ch. Lienau, “Evidence for strain-induced lateral carrier confinement in InGaAs quantum wells by

low-temperature near-field spectroscopy,” *Appl. Phys. Lett.*, vol. **79**, no 11, pp. 1611-1613, Jul. 2001.

[10]K. Kash, Derek D. Mahoney, B. P. Van der Gaag, A. S. Gozdz, J. P. Harbison, and L. T. Florez, “Observation of quantum dot levels produced by strain modulation of GaAs–AlGaAs quantum wells,” *J. Vac. Sci. Technol. B.*, vol. **10**, pp.2030-2033. 1992.

[11]M. Sopanen, H. Lipsanen, and J. Ahopelto, “Strain-induced quantum dots by self-organized stressors,” *Appl. Phys. Lett.*, vol. **66**, no 18, pp. 2364-2366, Mar. 1995.

[12]<http://www.nextnano.de/nextnano3/index.htm>, 2012.

Chapter 7: Development of New Design of Hybrid QW/QD Structure for High Power and Broad Bandwidth Superluminescent Diodes

7.1 Introduction

Previous work has shown that a significant enhancement of the spectral bandwidth of a multi-layer quantum dot (QD) device can be achieved by the introduction of single quantum well (QW) spectrally positioned to be coincident with the QD second excited state (ES2) emission, and spatially positioned closet to the n-contact (see the TEM imaging result in Fig. 3.4 (a)). The higher saturated gain of the QW offsets loss associated with ES2 of the QDs, as a result, a spontaneous emission with a 3dB bandwidth of 250nm was achieved (see the inset of Fig. 3.10). Similarly, as illustrated in Fig. 4.4(a), gain measurements indicate a positive modal gain spanning ~300nm, covering the wavelength range of 1100-1400nm [1]. Bias-controlled simultaneous three-state lasing [2], via the ground state (GS) and first excited state (ES1) transitions of the QDs and the lowest energy transition of the single QW, spanning ~160nm can also be observed at room temperature for suitable lengths and current densities, which is demonstrated in the Fig. 4.8(b). In the end, based on this structure, the first hybrid QW/QD superluminescent diode (SLD), which is capable of

emitting an emission bandwidth of 289nm centered at 1200nm with a corresponding output power of 2.4mW at room temperature, has been achieved [see chapter 5].

However, in previous work, hybrid QW/QDs structures only contain 6 DWELL layers and the dot density per layer was $\sim 3 \times 10^{10} \text{ cm}^{-2}$, which results in a relative small saturation gain of 12 cm^{-1} for GS, and therefore low output power of 2.4mW. For skin imaging applications using OCT systems, high power is required for deep penetration and increased signal to noise ratio. Therefore it is necessary to increase the number of dot layers and the dot density. Based on my previous work, in this chapter, results on new device designs utilizing a larger number of QD layers with higher areal density [3, 4] grown by collaborators at QD Laser Incorporated (Japan) are reported. In addition to the ability to incorporate more than twice as many QDs, the state separation of the devices is higher than previous structures grown in Sheffield by moving the 1130nm QW further to 1080nm, leading to broader theoretical bandwidths and high temperature operation [5, 6]. Four structures are studied including three hybrid QW/QD structures and one QD-only structure. All the hybrid QW/QD structures have a 1080nm InGaAs QW, positioned closest to the n-contact, and nine QD layers. Room temperature characterization is in line with previous Sheffield grown samples and structures (will be discussed in detail later in this chapter). I go on to describe designs for chirped and un-chirped QD structures [7]. Spectrally positioning the dots to overlap, provides smaller spectral modulation to the spontaneous emission spectra, yet still allows the identification of the QD GS and ES, and QW. I also describe designs for an asymmetric triangular QW and a rectangular

symmetrical QW. Both structures were realized using a digital alloy approximation. I show that a triangular indium composition QW profile makes high order QW transitions more pronounced via PC spectroscopy. Finally, I report on the spontaneous emission spectra from an optimized structure (that consisted of chirped QDs and digital alloy triangular QW under CW operation, without active cooling. The combined effect of our design and self-heating effects results in a spontaneous emission spectrum spanning 350nm.

7.2 Second Generation Hybrid QW/QD Structure

7.2.1 Device Structure and Fabrication

I focus firstly on the second generation hybrid QW/QD p-i-n structure termed “QLF1375-AE”, which was grown by a commercial supplier (QD Laser Inc.). The structures under studied was grown by molecular beam reactor on a (100) Si-doped GaAs substrate.

The epitaxy for this structure starts with a 300nm thick n-type GaAs buffer layer (Si: $1 \times 10^{18} \text{ cm}^{-3}$) followed by a combination of $\text{Al}_{0.2}\text{Ga}_{0.8}\text{As}/\text{Al}_{0.4}\text{Ga}_{0.8}\text{As}/\text{Al}_{0.2}\text{Ga}_{0.8}\text{As}$ in thickness of 200nm – 1400nm – 200nm n-type (Si: $6 \times 10^{17} \text{ cm}^{-3}$) which acts as the lower cladding layer. The usage of this combination as a cladding layer can effectively smooth band discontinuities, enhancing carrier transport, and helping to confine carriers into the active region. Above the lower cladding layer is the active region, followed by another combination of $\text{Al}_{0.2}\text{Ga}_{0.8}\text{As}/\text{Al}_{0.4}\text{Ga}_{0.8}\text{As}/\text{Al}_{0.2}\text{Ga}_{0.8}\text{As}$

p-type upper cladding layer in thickness of 200nm – 1400nm – 200nm respectively, and finally a highly p-doped ($1.4 \times 10^{19} \text{ cm}^{-3}$) GaAs contact layer. The basic device structure for this structure is schematically shown in Fig. 7.1.

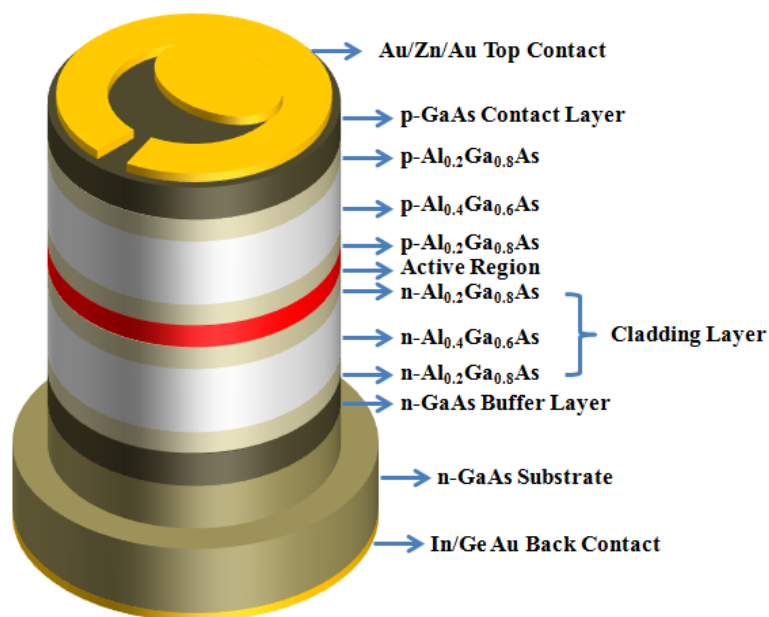
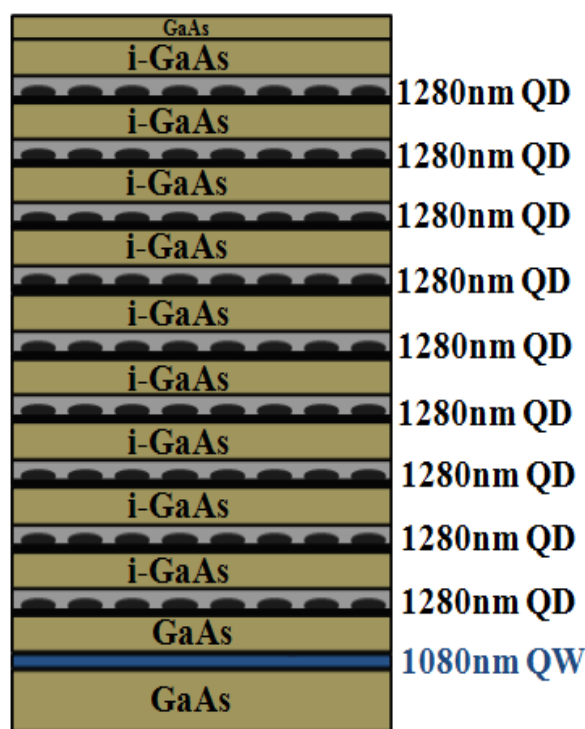


Fig. 7.1 Schematic of the basic device structure studied in this chapter.

Fig.7.2 (a) shows schematics of the active region for the second-generation hybrid QW/QD sample QLF1375-AE. For the growth of the active region, first of all, 56.5nm of un-doped GaAs and a 7nm In_{0.29}Ga_{0.71}As single QW were grown, followed by 36.5nm thick un-doped GaAs barriers. Above this were nine InAs QDs layers. Each InAs QD layer was form by depositing 0.8nm InAs, capped with 3.7nm InGaAs strain reduce layer (SRL). By means of the SRL, the effect of strain on the InAs QDs between the lattice mismatch of InAs and GaAs can be partly relaxed as the lattice constant of the SRL is larger than that of GaAs, therefore, resulting in a smaller

bandgap red shift induced by strain [8]. The nine layers of the InAs QDs were each separated by a 35.5nm thick un-doped GaAs barrier layer. The GaAs barrier between the single QW and the first QD layer is 36.5nm thick, and as mentioned above no tunneling/electronic coupling between the QW and QDs is expected due to such a thick barrier.



QLF1375-AE

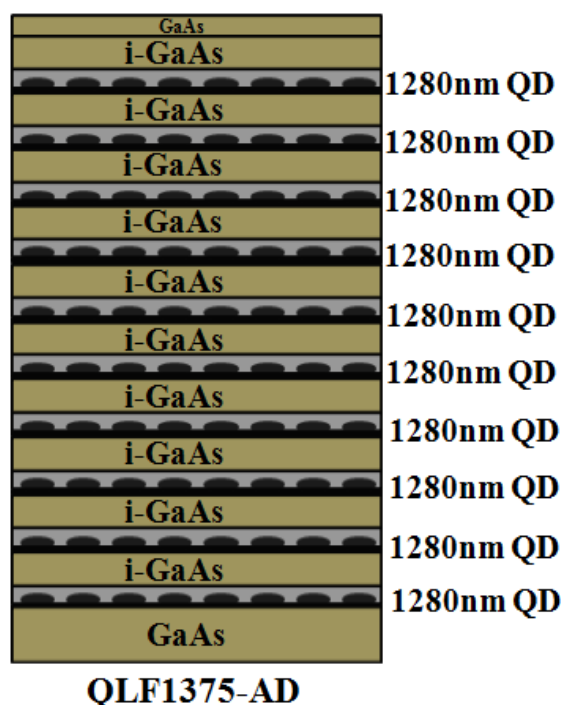


Fig. 7.2 Schematic diagram of the active region for sample AD, AE.

In comparison to my previous work [1], this newly developed design utilizes a large number of the QD layers with higher areal density [9], therefore, enhanced modal gain is expected from this structure. Also the state separation of this structure is higher than previous samples (the QW emission being moved from 1130nm to 1080nm), leading to broader theoretical bandwidths as the spectral bandwidth is determined by the separation between the QD GS and ES2.

In order to verify the effect of the single QW, a structure, termed “QLF1375-AD”, containing only QDs was grown under identical conditions to those described above, but with QW replaced by a QD layer, i.e., it contained ten QD layers in its active region, also shown in the Fig.7.2 (b). To characterize the spontaneous emission and

photocurrent, standard optical access p-i-n mesa diodes were fabricated [10]. And the final device is schematically shown in Fig. 7.1.

7.2.2 Results and Discussion

Fig. 7.3 shows the normalized photocurrent (PC) spectrum at 0V (short-circuit) for sample QLF1375-AD and QLF1375-AE at room temperature. For sample AD (containing just ten layer of QDs emitting at ~1280nm), three well-defined features, arising from the InAs QDs interband absorption (GS, ES1 and ES2) are observed at ~1275nm, ~1170nm and ~1095nm respectively. A similar spectrum is observed for the hybrid QW/QD sample AE (consisting of nine InAs QDs emitting at ~1280nm and one single InGaAs QW emitting at ~1080nm), very good agreement between the ground state and first excited state transition energies in sample AD and AE is found. A small shoulder due to ES2 of the QDs is also partially resolved around 1095nm for sample AD. While a strong PC signal appearing at ~1075nm is observed in sample AE, which is attributed to the lowest energy transition of the QWs. In order to further confirm that the feature at 1075nm is due to the QW rather than the ES2 of the QDs, the transition energies for these features are tracked as a function of reverse bias from 0 to 10V at room temperature. As seen, a linear shift of QD interband transitions (GS and ES1) to long wavelength (lower energy) is clearly observed, in line with a dipole being present within the QDs at zero bias. However, for the feature at 1075nm (at 0V), as the applied reverse bias is increased, a quadratic shift of the transition to low energy and a concomitant broadening of the PC peak is observed due

to the quantum confined Stark effect (QCSE) [11]. This is also in contrast to what has been observed for ES2 of sample AD as shown in the inset of Fig. 7.3 (lower). The agreement with the predicated transition at 1080nm and QCSE allows us to confirm this feature to the absorption by the e1-hh1 QW transitions.

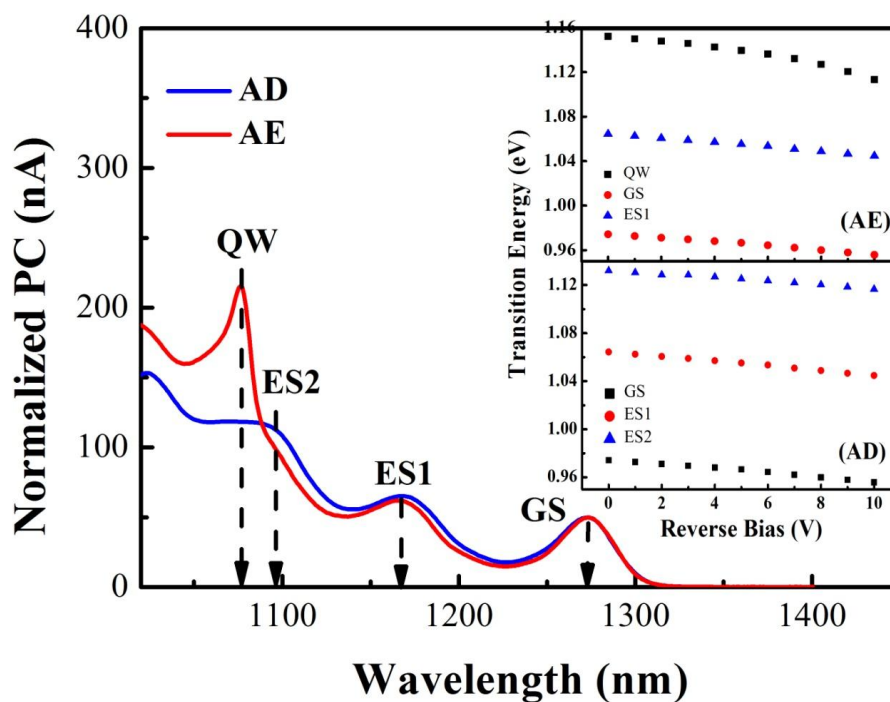


Fig. 7.3 Normalized photocurrent (PC) spectrum at 0V (short-circuit) for sample QLF1375-AD and QLF1375-AE at room temperature. The inset shows the transition energy as a function of reverse bias sample AE (GS, ES1 and QW) and sample AD (GS, ES1 and ES2).

Fig. 7.4 shows the normalized spontaneous emission (SE) spectrum at the same current of 1A under pulsed operation of 10% duty cycle and 5 μ s pulse width at room temperature for sample AD and AE. For sample AD, the emission spectrum clearly shows three features at 1285nm, 1190nm and 1105nm, corresponding to the GS, ES1 and the ES2 of the QDs interband transitions. As seen, at this current, there is no significant ES2 emission observed from this sample, as these states are not fully

occupied. Very good agreement between the QDs interband transitions (GS, ES1 and ES2) in sample AD and AE is found. For sample AE, as seen in previous work, a strong contribution to the emission spectrum from the QW is observed at 1080nm. For the SE emission, the separation between the QW and ES2 is about 20nm, which is also in good agreement with the separation between the QW and ES2 observed in PC spectra. A 10nm red-shift in the SE spectrum as compared to the PC is noted due to the different bias conditions and free carrier effects [12].

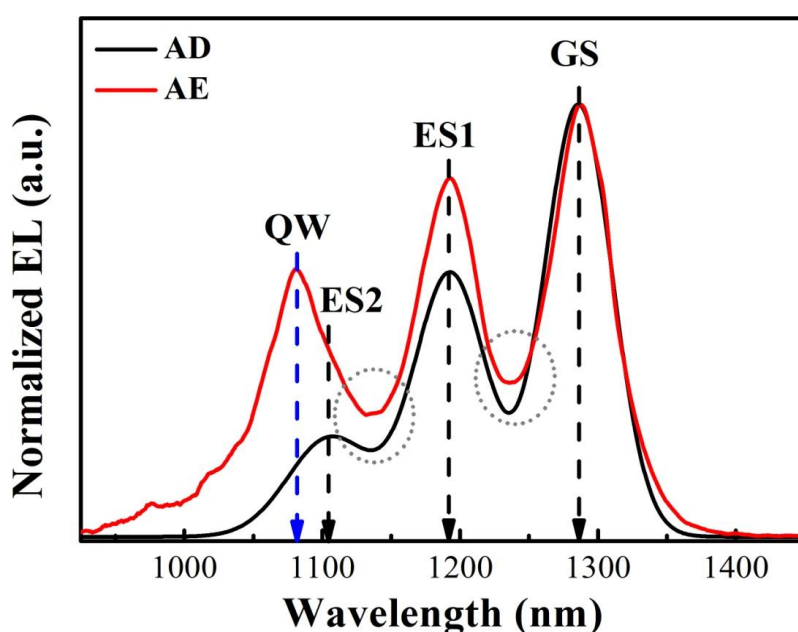


Fig. 7.4 normalized spontaneous emission (SE) spectrum at the same current of 1A under pulsed operation of 10% duty cycle and 5 μ s pulse width at room temperature for sample AD and AE.

Compared with our previous design (six-layer of QDs with single QW at 1130nm), the new developed hybrid QW/QD structure utilizing larger numbers of QD layers (nine-layer QDs) with higher areal density (50 percent higher areal number of dots), should lead to more modal gain. The state separation between the QD states is also higher than previous design with the QW moved from the 1130nm to 1080nm.

Therefore, this new design (sample AE) is expected to achieve broader theoretical bandwidth and high output power. However, as noted from the SE spectrum, large spectrum modulation is observed due to the reduced spectral overlap between the GS and ES1 emission as well as between the ES1 and the QW emission, which is attributed to the reduced inhomogeneous broadening. This reduced QD inhomogeneity with high dot density are the key factors for QD based devices to achieve high gain and operate at high temperatures [6], however, the large spectrum modulation also degrades the resolution of the OCT system by introducing sidelobes due to the non-Gaussian spectrum [13].

A preliminary summary reached here is that, compared with our previous hybrid QW/QD structure, for this second-generation hybrid QW/QD structure, the effects in terms of PC and SE are repeatable. These materials are expected to provide higher gain and broader spectral bandwidth due to high dot densities and larger state separation, respectively. However, the large spectral modulation between the QW and QD GS and QD ES1 emission is also observed due to the large state separation between QW and QD and reduced QD inhomogeneity.

Therefore, in order to reduce the spectral modulation and to further broaden the emission bandwidth, a new series of structures, i.e., the third generation of hybrid QW/QD structure was developed for future SLDs and amplifiers.

7.3 Third Generation Hybrid QW/QD Structure

7.3.1 Device Structure and Fabrication

Fig. 7.5 shows a schematic diagram of the active region of the final hybrid QW/QD structure developed during my PhD. This sample (QLF1375-AJ) is termed the 3rd generation hybrid QW/QD structure. The epitaxy for the third generation hybrid QW/QD structure is essentially identical with the second generation hybrid QW/QD structure except for the growth of the active region.

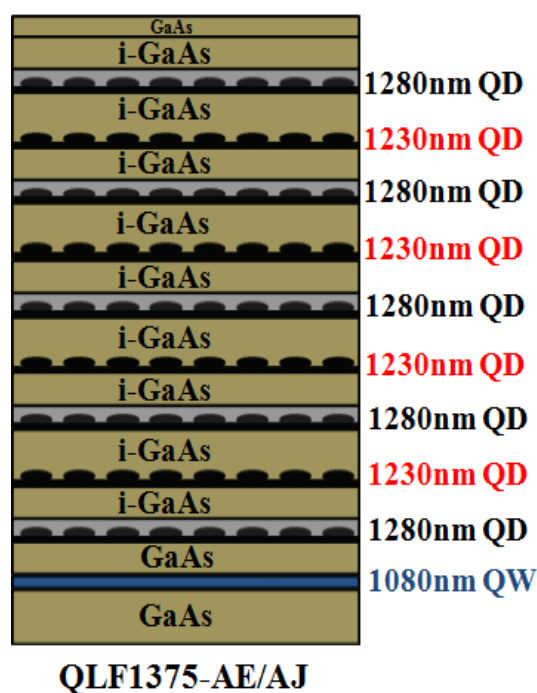


Fig. 7.5 Schematic diagram of the active region for sample AI/AJ.

The growth of the active region for QLF1375-AJ, consisted firstly of 56.5nm of undoped GaAs and a ~7nm 1080nm digital alloy InGaAs QW was grown, followed by five-layers of InAs QDs with emission wavelength at 1280nm (type A QDs) and

four layers of InAs QDs with emission wavelength at 1230nm (type B QDs). This nine-layer stack of QDs was grown in the sequence A/B/A/B/A/B/A/B/A in order to attempt to evenly distribute carriers between the different QD layers. For the growth of the 1280nm InAs QDs, a 3.7nm InGaAs SRL was used as discussed above. For the growth of the 1230nm InAs QDs, the self-assembled QDs were directly covered by a GaAs capping layer. The chirped QDs are intended to spectrally position the dots to overlap, providing smaller modulation to the emission spectra [7].

Traditional rectangular QWs have been well studied [14, 15]. It is well known that, without electric field is applied, the overlap integral of wave functions between the conduction band ($n=1$) and valence band ($n=1$) is very close to unit, leading to strong emission and absorption process. Unfortunately, in most of photo-electronic devices the QW is subjected to internal and external electric fields from the device [16]. These fields will push the electron and hole wave functions in opposite directions reducing the wave functions overlap integral and therefore reduce the emission and absorption process in QW devices. Recently, asymmetrical triangular quantum wells have attracted significant attention due to the potential to increase the overlap integral. The growth of asymmetrical triangular quantum well is based on compositional gradients [16], which are normally achieved by two major techniques. The first technique is the analog alloy method, and a detail description for this method growing asymmetrical triangular quantum well can be found in [17]. Another method is named digital alloy method. And, in our case, this digital alloy method is based on the approximation of

the alloy composition profile by using alternating layers of InAs and GaAs where the ratio of layer thicknesses determines the average alloy composition [16]. For the growth of the QW in this chapter, an asymmetric triangular quantum well was grown by a digital alloy approximation in an attempt to further broaden the emission bandwidth from the single InGaAs QW by further promoting the emission of normally forbidden higher order transitions. A reference sample, named QLF1375-AI, containing a rectangular symmetrical quantum well was grown under identical conditions to sample QLF1375-AJ.

The as-designed In composition profile for the digital alloy approximation and the ideal average composition profile for sample QLF1375-AI/AJ are shown in Fig.7.6. As seen, for QLF1375-AI (Fig. 7.6 (a)), eighteen layers of InAs/GaAs in a thickness of 0.11nm and 0.269nm were grown respectively to produce a 6.822nm $\text{In}_{0.29}\text{Ga}_{0.71}\text{As}$ digital alloy QW with a constant In composition of 0.29. This kind of digital alloy InAs/GaAs QW can be regard as a normal $\text{In}_{0.29}\text{Ga}_{0.71}\text{As}$ QW [16], and this was confirmed by modeling.

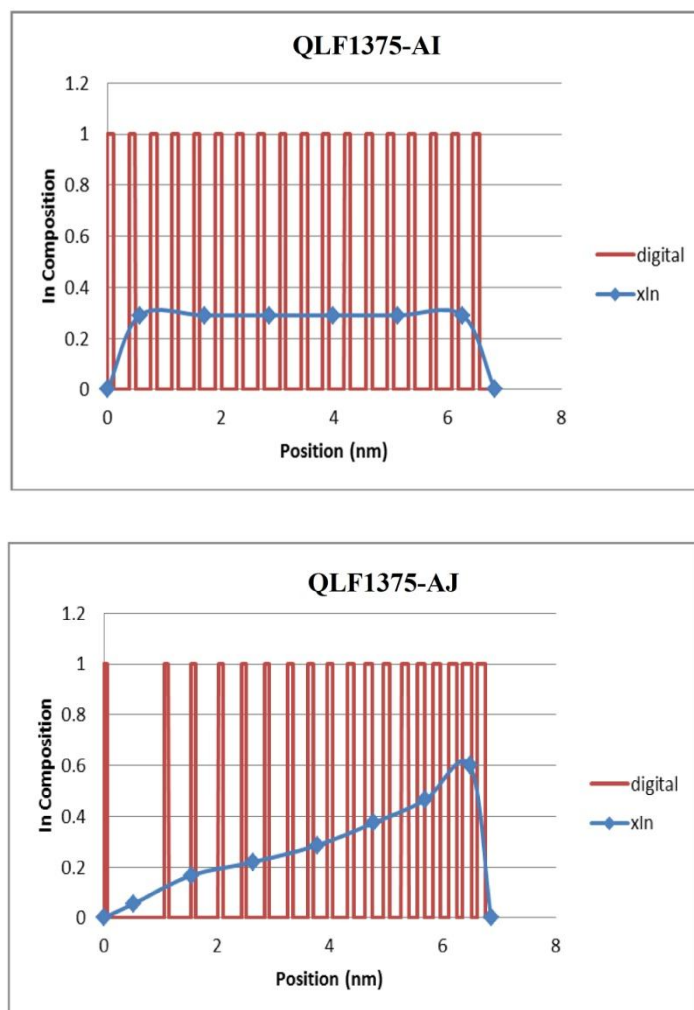


Fig. 7.6 The In composition profile for sample AI and AJ grown by a digital alloy approximation. (Figures courtesy by QD laser Lnc.)

For the sample QLF1375-AJ (Fig. 7.6 (b)), in comparison to sample AI, eighteen layer of InAs/GaAs layers with grading In composition from 0.0566 to 0.6 were deposited to form an asymmetric triangular InGaAs QW with a average In composition of 0.29. A detailed description of the growth of the digital alloy InGaAs QW is summarized in table 1.

| xIn | InAs(nm) | GaAs(nm) | loop | In (sec) | Ga (sec) | thickness (nm) | comm thick | position | xIn | In*thick | |
|----------|----------|------------|------|----------|----------|----------------|------------|----------|---------|-------------|----------|
| | | | | | | | | 0 | 0 | | |
| 0.290237 | 0.11 | 0.269 | 3 | 1.98 | 2.421 | 1.137 | 1.137 | 0.5685 | 0.29024 | 0.33 | |
| 0.290237 | 0.11 | 0.269 | 3 | 1.98 | 2.421 | 1.137 | 2.274 | 1.7055 | 0.29024 | 0.33 | |
| 0.290237 | 0.11 | 0.269 | 3 | 1.98 | 2.421 | 1.137 | 3.411 | 2.8425 | 0.29024 | 0.33 | |
| 0.290237 | 0.11 | 0.269 | 3 | 1.98 | 2.421 | 1.137 | 4.548 | 3.9795 | 0.29024 | 0.33 | |
| 0.290237 | 0.11 | 0.269 | 3 | 1.98 | 2.421 | 1.137 | 5.685 | 5.1165 | 0.29024 | 0.33 | |
| 0.290237 | 0.11 | 0.269 | 3 | 1.98 | 2.421 | 1.137 | 6.822 | 6.2535 | 0.29024 | 0.33 | |
| | | total loop | 18 | | | | | 6.822 | 0 | | |
| | | | | | | | | | | 1.98 | |
| | | | | | | Well thickness | 6.822 | | | average xIn | 0.290237 |

| xIn | InAs(nm) | GaAs(nm) | loop | In (sec) | Ga (sec) | thickness (nm) | comm thick | position | xIn | In*thick | |
|----------|----------|----------|------|----------|----------|----------------|------------|----------|---------|-------------|----------|
| | | | | | | | | 0 | 0 | | |
| 0.056604 | 0.06 | 1 | 1 | 1.08 | 18 | 1.06 | 1.06 | 0.53 | 0.0566 | 0.06 | |
| 0.166667 | 0.08 | 0.4 | 2 | 1.44 | 7.2 | 0.96 | 2.02 | 1.54 | 0.16667 | 0.16 | |
| 0.219512 | 0.09 | 0.32 | 3 | 1.62 | 5.76 | 1.23 | 3.25 | 2.635 | 0.21951 | 0.27 | |
| 0.285714 | 0.1 | 0.25 | 3 | 1.8 | 4.5 | 1.05 | 4.3 | 3.775 | 0.28571 | 0.3 | |
| 0.375 | 0.12 | 0.2 | 3 | 2.16 | 3.6 | 0.96 | 5.26 | 4.78 | 0.375 | 0.36 | |
| 0.464286 | 0.13 | 0.15 | 3 | 2.34 | 2.7 | 0.84 | 6.1 | 5.68 | 0.46429 | 0.39 | |
| 0.6 | 0.15 | 0.1 | 3 | 2.7 | 1.8 | 0.75 | 6.85 | 6.475 | 0.6 | 0.45 | |
| | | | | | | | | 6.85 | 0 | | |
| | | | | | | | | | | 1.99 | |
| | | | | | | Well thickness | 6.85 | | | average xIn | 0.290511 |

Table. 7.1 Summary of growth of InGaAs digital QW for sample AI (upper) and AJ (lower). (Tables courtesy by QD laser Lnc.)

These structures were also fabricated into optical access mesa diodes [10] for material characterization. The final device is shown schematically in Fig. 7.1.

7.3.2 Results and Discussion

7.3.2.1 The Effect of Chirped QDs

Firstly, I discuss the effect of the chirped QDs on the emission spectrum. Fig. 7.7 shows the normalized PC (short-circuit) and normalized SE spectrum for sample AE (consist of nine QDs at 1280nm and single QW at 1080nm) and sample AI (consist of chirped QDs at 1280nm and 1230nm respectively and digital alloy QW at 1080nm) at room temperature. Here, the normalization is made to the QD GS. In the PC spectra,

in addition to absorption peaks at 1275nm and 1170nm, attributed to the interband absorption of GS and ES1 of the 1280nm InAs QDs, two more features at 1220nm and 1130nm are also clearly observed, which are related to the absorption of GS and ES1 of the 1230nm InAs QDs.

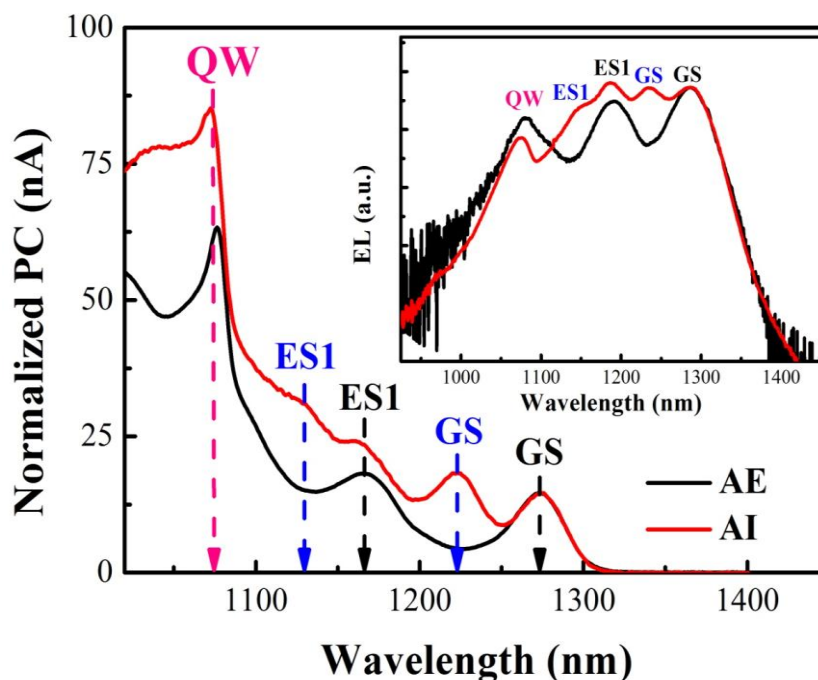


Fig. 7.7 Normalized PC (short-circuit) and normalized SE spectrum for sample AE (consist of nine QDs at 1280nm and single QW at 1080nm) and sample AI (consist of chirped QDs at 1280nm and 1230nm respectively and digital alloy QW at 1080nm) at room temperature. The inset shows the normalized emission spectra for sample AE and AI at the same current density of $450\text{A}/\text{cm}^2$.

The inset to Fig. 7.7 plots the normalized spontaneous emission spectra at $\sim J = 450\text{A}/\text{cm}^2$. The “chirping” of the QD layers reduces the modulation of the spontaneous emission spectra, yet still allows the identification of the QD ground state and excited states, and QW emission.

7.3.2.2 Asymmetric triangular quantum well

To further broaden the emission from the single 1080nm InGaAs QW, an InAs/GaAs asymmetric triangle QW was grown by molecular-beam epitaxy using a digital alloy composition grading method, since this asymmetric triangular QW is expected to provide more pronounced high order quantum well transitions (e1-hh2, and e1-hh3) [16, 17, 18].

Fig. 7.8 shows the normalized (to the peak PC of the GS) PC for sample AI and AJ at room temperature at 0V. It is noteworthy that very good agreement between the QDs transitions energies in sample AI and AJ is found. For sample AI, at 0V, a single sharp QW PC peak (due to the lowest energy QW transition) is observed due to the good uniformity of In composition in the InAs/GaAs layers making up the QW. Compared to sample AI, the lowest QW PC peak for sample AJ is much broader, and this is attributed to the modulation of the QW due to the triangular profile of In composition in the QW.

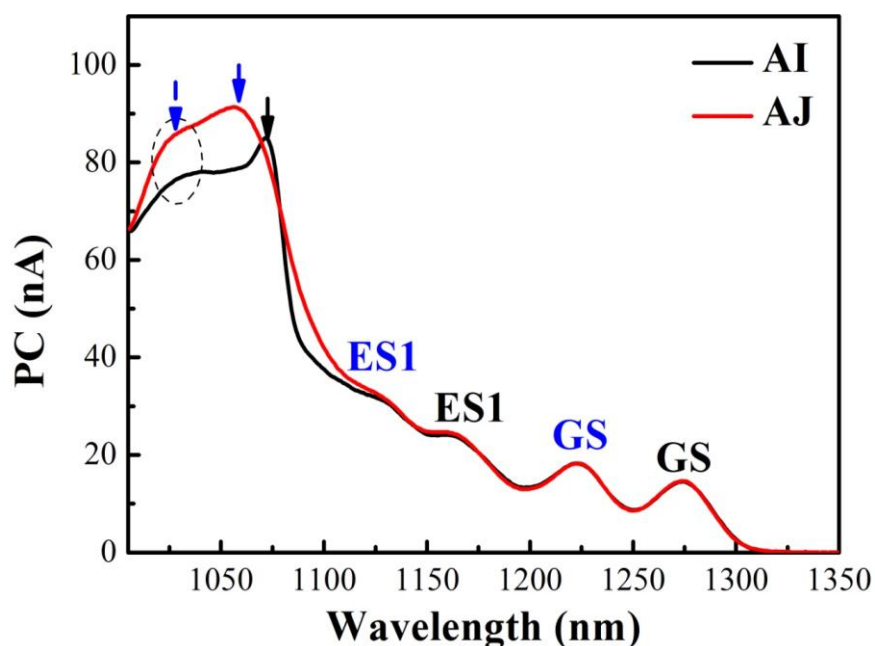


Fig. 7.8 Normalized PC for sample AI and AJ at room temperature at 0V.

For sample AJ, in addition to the PC peak, which is related to the lowest QW absorption, strong PC signal (compared to sample AI) related to the higher order QW transitions are also observed, this is in line with the modelling results of the wave functions for a digital alloy InGaAs QW, which show that the overlap integral between the conduction ($n=1$) and heavy hole ($n=2$) wave functions has been significantly improved from 0.04% (normal rectangular QW) to over 10% through the use of this design.

However, the lowest QW PC peak intensity for sample AJ is also higher than that of sample AI, this is an unexpected result, as in comparison with rectangular symmetric QW, in the asymmetric triangular QW, the overlap integral between the conduction ($n=1$) and heavy hole ($n=1$) wave functions decreases, and the reduction in the

overlap integral should result in a reduction in absorption. The modelling results also show that, the wave function overlap integral (for e1-hh1 transition) for sample AI and AJ is about 94% and 81% respectively. The possible reasons for the unexpected enhancement in the QW related PC in sample AJ may be due to increased tunnelling effects in the triangular QW, which enhance carrier extraction.

7.3.2.3 Ultra-broad Spontaneous Emission

Fig. 7.9 shows the spontaneous emission from sample QLF1375-AJ (3rd generation hybrid QW/QD structure which consists of chirped QDs and digital alloy triangular QW) fabricated into a surface emission mesa diodes driven under CW conditions, with no active cooling at room temperature. As seen, as the current density is increased, a significant red-shift and a concomitant decrease of the peak intensity is observed due to self-heating. The shift of the QD ground-state is $\sim 100\text{nm}$, and by assuming a band-edge shift for InAs/GaAs quantum dot is $\sim 0.5\text{nm/K}$, a junction temperature of 493K is estimated. While this self-heating effect may suppress the QD gain to some extent, it benefits the spectral bandwidth significantly. It is noteworthy that similar materials are able to be used as laser at very high temperature [6].

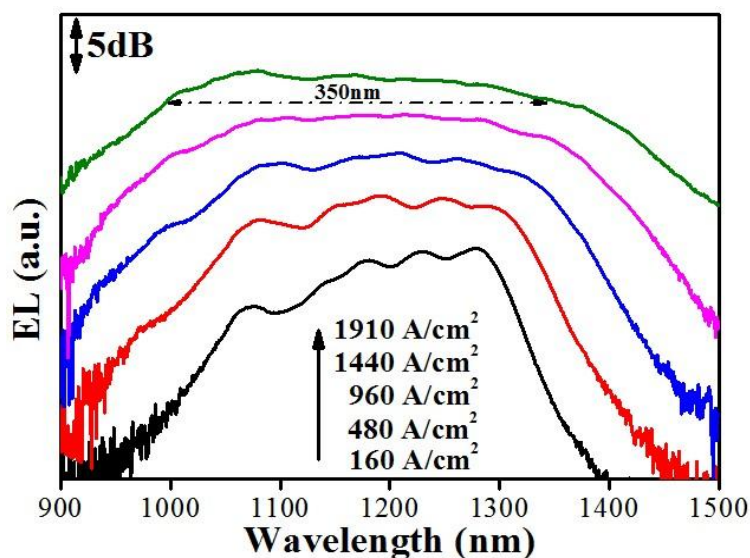


Fig. 7.9 Spontaneous emission spectra at various current densities from sample QLF1375-AJ (3th generation hybrid QW/QD structure which consists of chirped QDs and digital alloy triangular QW) fabricated into surface emission mesa diodes driven under CW conditions, with no active cooling at room temperature.

There is therefore a trade off between the reduction of peak gain and the enhancement of the spectral bandwidth and this trade off can be reduced by increasing the gain and increasing the quantized-energy separation [6].

Due to the combined effect of this design and self-heating (Joule heating), an ultra broad spontaneous emission with 3dB bandwidth of 350nm (spanning from 990nm to 1340nm) centred at 1200nm is achieved under continuous wave (CW) operation at room temperature. This result for spontaneous emission improved on our previous best result by ~100nm [1,10], suggesting that these 3rd generation designs have a great potential for achieving high resolution imaging in OCT systems.

7.4 Conclusion

In previous chapters, I have shown that a single QW introduced into a multi-layer QD structure can result in spontaneous emission FWHM of 250nm and positive modal gain of ~300nm. Based on this structure, the first hybrid QW/QD SLD, with an emission spectral width of 289nm centered at 1200nm with a corresponding power of 2.4mW under pulsed operation at room temperature has been achieved. In this chapter, new designs, incorporating chirped QD layers with higher areal density and higher number of QD layer as well as utilizing an asymmetric triangular QW, demonstrate CW spontaneous emission FWHM of ~350nm. This is due to the beneficial effect of self-heating, higher state-splitting between QW and QDs, and emission from high order QW transitions.

7.5 Future Work

An analysis of the evolution of the gain and spontaneous emission spectrum with current and temperature needs to be carried out on all the structures (sample AD, AE, AI, and AJ). This can provide us with more information about the carrier capture and transport effects in the QD laser structure and hybrid QW/QD laser structure.

Superluminescent diodes need to be fabricated. The fabrication can follow previous methods described in chapter 5 for comparisons in terms of power and spectrum bandwidth. Once we get CW working SLDs. The next step is to use these SLDs as the light source for skin imaging in OCT system.

Rectangular QWs have been extensively studied and used as active elements for broadband sources by using chirped QW, QW intermixing as so on [19, 20]. Asymmetric triangular QW grown by a digital alloy approximation also have a great potential for broadband sources, since this structure is expected to offer more pronounced high order QW transitions. My results suggest that more attentions should be paid to this, in conjunction with optimisation of QD to QW separation, as discussed in chapter 6.

Reference

- [1] S. M. Chen, K. J. Zhou, Z. Y. Zhang, D. T. D. Childs, M. Hugues, A. J. Ramsay, and R. A. Hogg, “Ultra-broad spontaneous emission and modal gain spectrum from a hybrid quantum well/quantum dot laser structure,” *Appl. Phys. Lett.*, vol. 100, no. 4, pp. 041118-1 – 041118-3, Jan. 2012.
- [2] S. M. Chen, K. J. Zhou, Z. Y. Zhang, O. Wada, D. T. D. Childs, M. Hugues, X. Jin and R. A. Hogg, “Room temperature simultaneous three-state lasing in hybrid quantum well/quantum dot laser,” *Electron. Lett.*, vol. 48, no. 11, pp. 644-646. May. 2012.
- [3] Y. Tanaka, M. Ishida, Y. Maeda, T. Akiyama, T. Yamamoto, H. Z. Song, M. Yamaguchi, Y. Nakata, K. Nishi, M. Sugawara, and Y. Arakawa, “1.3 μ m InAs/GaAs high-density quantum dot lasers,” Optical Fiber Communication Conference (OFC) 2009, OWJ1
- [4] K. Nishi, T. Kageyama, M. Yamaguchi, Y. Maeda, K. Takemasa, T. Yamamoto, M. Sugawara, and Y. Arakawa, The 17th Intl. Conf. on MBE (MBE 2012), TuA-3-5 (2012).
- [5] T. Kageyama, K. Takada, K. Nishi, M. Yamaguchi, R. Mochida, Y. Maeda, H. Kondo, K. Takemasa, Y. Tanaka, T. Yamamoto, M. Sugawara, and Y. Arakawa, SPIE Photonics West 2012, 8277-11, (2012).
- [6] T. Kageyama, K. Nishi, M. Yamaguchi, R. Mochida, Y. Maeda, K. Takemasa, Y. Tanaka, T. Yamamoto, M. Sugawara, and Y. Arakawa, “Extremely high temperature (220 ° C) continuous-wave operation of 1300-nm-range quantum-dot lasers, CLEO/Europe-EQEC 2011, PDA.1.
- [7] S. K. Ray, K. M. Groom, M. D. Beattie, H. Y. Liu, M. Hopkinson, and R. A. Hogg, “Broad-Band Superluminescent Light-Emitting Diodes Incorporating Quantum Dots in Compositionally Modulated Quantum Wells,” *IEEE Photon. Technol. Lett.*, vol. **18**, pp.58-61. 2006.
- [8] V. M. Ustinov, A. E. Zhukov, A. Y. Egorov, and N. A. Maleev, Quantum dot lasers, Oxford, New York, 2003.
- [9] Y. Tanaka, M. Ishida, K. Takada, T. Yamamoto, H. Z. Song, Y. Nakata, M. Yamaguchi, K. Nishi, M. Sugawara and Y. Arakawa, “25 Gbps direct modulation in 1.3- μ m InAs/GaAs high-density quantum dot lasers,” CLEO’10 CTuZ1 (2010).
- [10] S. Chen, K. Zhou, Z. Zhang, J. R. Orchard, D. T. D. Childs, M. Hugues, O. Wada, and R. A. Hogg, “Hybrid Quantum Well/Quantum Dot Structure for Broad Spectral Bandwidth Emitters,” *IEEE J. Select. Topics Quantum Electron.*, vol.**19**,

- no. 4, pp. 1900209-1900209-9, Jul/Aug. 2013.
- [11]D. A. B. Miller, D. S. Chemla, T. C. Damen, A. C. Gossard, W. Wiegmann, T. H. Wood, and C. A. Burrus, “Band-edge electroabsorption in QW structure: the quantum-confined stark effect,” *Phys. Rev. Lett.*, vol. **53**, no. 22, pp. 2173-2176, Nov. 1984.
- [12]H. Shahid, D. T. D. Childs, B. J. Stevens, and R. A. Hogg, “Negative differential gain due to many body effects in self-assembled quantum dot lasers,” *Appl. Phys. Lett.*, vol. 99, no. 6, pp. 061104-1 – 061104-3, Aug. 2011.
- [13]C. Ackay, P. Parrein, and J. P. Rolland, “Estimation of longitudinal resolution in optical coherence imaging,” *Appl. Opt.*, vol. 41, no. 25, pp. 5256– 5262, Aug. 2002.
- [14]D. Gerber , R. Droopad, and G. N. Maracas, “Comparison of electroabsorption in asymmetric triangular and rectangular GaAs/Al_xGa_{1-x}As multiple quantum wells,” *Appl. Phys. Lett.* vol. 62, no. 5, pp.525-527, Feb, 1993.
- [15]K. -K. Law, R. H. Yan, A. C. Gossard, and J. L. Merz, “Electric field induced absorption changes in triangular quantum wells grown by pulsed beam molecular beam epitaxy technique,” *J. Appl. Phys.* Vol. 67, no. 10, pp. 6461-6465, 1990.
- [16]D. L. Mathine, G. N. Maracas, D. S. Gerber, R. Droopad, R. J. Graham, and M. R. McCartney, "Characterization of an AlGaAs/GaAs asymmetric triangular quantum well grown by a digital alloy approximation," *J. Appl. Phys.*, vol. 75, pp.4551-4556.
- [17]S. Vlaev, F. Garc á-Moliner, and V. R. Velasco, “Electronic states of digital versus analog graded quantum wells,” *Phys. Rev. B.*, vol. 52, pp.13784-13787. 1995.
- [18]D. J. Feng, C. L. Chiu, S. H. Lin, T. S. Lay, and T. Y. Chang, “InGaAlAs/InGaAs strain-balanced multi-quantum-well laser/semiconductor optical amplifiers operating at excited transitions,” *J. Vac. Sci. Technol. B.*, vol.26, pp.1163-1166. 2008.
- [19]C. F. Lin, and B. L. Lee, “Extremely Broadband AlGaAs/GaAs superluminescent diodes,” *Appl. Phys. Lett.*, vol. 32, pp.1598-1600, 1997.
- [20]T. K. Ong, M. Yin, Z. Yu, Y. C. Chan, and Y. L. Lam, “High performance QW intermixing superluminescent diodes,” *Meas. Sci. Technol.*, vol. 15, pp. 1591-1595, 2004.

Chapter 8: Conclusion

In this thesis, I have presented and discussed results concerned with a hybrid QW/QD structure for application in broadband sources.

In chapter 3, the concept of the hybrid QW/QD structure has been introduced. The hybrid structures incorporate a single InGaAs QW and six InAs DWELL layers. The QW is spectrally positioned to be coincident with emission from the second ES of the QDs. I have compared the two hybrid samples where the QW position is changed, and have investigated the optoelectronic properties (such as I - V , C - V , and PC), and temperature-dependent spontaneous emission for both the hybrid QW/QD samples. From experimental results and calculations, I conclude that the significant difference in room temperature spontaneous emission is due to the different carrier transport/distribution effects between the n-side and p-side samples. I have also shown an ultra-broad spontaneous emission for n-side sample due to the combined effect of QD GS, ES1 and the lowest energy state of QW.

In chapter 4, I presented modal gain result for n-side hybrid QW/QD structure. I have revealed that the modal gain for the QD ES1 can be clamped at low current density while the QW still increases in modal gain with further increasing current density. Most importantly, due to the combined contribution to gain spectrum from the GS and ES1 of the QD and the lowest energy transition of the QW, positive modal gain spans

~300 nm at room temperature, covering the wavelength of 1100–1400 nm. In this chapter, I also showed bias-controlled room temperature operation of simultaneous multi-state lasing over 160nm, and the threshold current density for achieving three-state lasing is shown to be reduced from 23000 to 1025A/cm² for the 2-mm-long device. In addition, I showed that, by changing the cavity length/optical loss, different lasing sequences for achieving three-state lasing are observed. Furthermore, unexpected lasing sequence for certain cavity lengths has been introduced, suggesting the optical pumping of the QW to the QDs.

In chapter 5, I presented the first hybrid QW/QD SLD, which is capable of emitting an emission bandwidth of 289nm centered at 1198nm with a corresponding peak power of 2.4mW at room temperature. I observed high order QW transitions at high current densities. I then assessed the hybrid QW/QD SLD for application in an OCT system. By introducing the Rayleigh criterion for resolution, a resolution of 2.9μm is obtained from the optimal result.

In chapter 6, I discussed the origin of the high order QW transitions observed in chapter 5. I showed that, QD strain modulation of the underlying QW, which is deposited *before* the QDs, results in a broadened linewidth of the e1-hh1 transition and leads to larger oscillator strengths for the higher order QW transitions (e1-hh2, e1-hh3).

In chapter 7, I presented new designs, incorporating chirped QD layers with higher areal density and higher number of QD layer as well as utilizing an asymmetric triangular QW. This design demonstrates CW spontaneous emission FWHM of ~350nm, and represents the first step in translation of my work to a commercial device.